Geoscientific
Model Development
Discussions

# Description and evaluation of the Diat-HadOCC model v1.0: the ocean biogeochemical component of HadGEM2-ES

Ian Totterdell[1]

[1]Met Office, Fitzroy Road, Exeter, EX1 3PB, UK

*Correspondence to:* Dr Ian Totterdell (ian.totterdell@metoffice.gov.uk)

**Abstract.** The Diat-HadOCC model (version 1.0) is presented. A simple marine ecosystem model with coupled equations representing the marine carbon cycle, it formed the ocean biogeochemistry sub-model in the Met Office's HadGEM2-ES Earth System Model. The equations are presented and described in full, along with the underlying assumptions, and particular attention is given to how they were implemented for the CMIP5 simulations. Results from the CMIP5 Historical simulation
5 (particularly those for the simulated 1990s) are shown and compared to data: dissolved nutrients and dissolved inorganic carbon, as well as biological components, productivity and fluxes. Where possible, the amplitude and phase of the predicted seasonal cycle is evaluated. Since the model was developed to explore and predict the effects of climate change on the marine ecosystem and marine carbon cycle, the response of the model to the RCP8.5 future scenario is also shown. The model generally matches well the available nutrient and DIC datasets, but the model chlorophyll is higher than observed while the total primary
10 production is just below the bottom of the range of global estimates. However, these quantities show realistic seasonal cycles.

*Copyright statement.* Crown Copyright, Met Office

## 1 Introduction

The recent publication of the 5th Assessment Report of Working Group 1 of the Inter-Governmental Panel on Climate Change (IPCC, 2013) includes analysis of four possible future scenarios of how the global climate might change over the next few
15 decades in response to anthropogenic emissions of carbon dioxide ($CO_2$) and other anthropogenic influences (e.g. changes to land use). These future scenarios are informed by the results of the 5th Climate Model Intercomparison Project, CMIP5 (Taylor et al., 2012), for which 47 different climate models ran one or more of the scenarios. Models are of course an absolute necessity for predicting future climate, since no observations can exist.

The number of general circulation models (GCMs) available to study climate has increased rapidly in recent years, and the
20 range of processes and feedbacks that they can represent has also become more comprehensive. Initially there were just physical models, describing the circulation of the atmosphere and the ocean and how those circulations redistributed and stored heat, as well as the response of the system to rising atmospheric $CO_2$. The first coupled climate model to include representations of the land and marine carbon cycles, including terrestrial vegetation and soils and marine ecosystems and capable of representing

their basic feedbacks on the climate, was HadCM3LC (Cox et al., 2000). In that model, the terrestrial vegetation was described by the TRIFFID model (Cox, 2001), while the chemistry of carbon dioxide in sea-water and the marine ecosystem were described by the Hadley Centre Ocean Carbon Cycle (HadOCC) model (Palmer and Totterdell, 2001). The latter is a simple Nutrient-Phytoplankton-Zooplankton-Detritus (NPZD) model, using nitrogen as the limiting element.

5    A brief overview of Met Office model nomenclature is useful here. The Met Office modelling system used (over a time period of several decades) for climate studies and for numerical weather prediction is known as the Unified Model, and the coupled climate models exist as various versions of it. The HadCM3LC model mentioned above featured a lower-resolution ("L") ocean sub-model than the HadCM3C model, which itself was the member of the HadCM3 family of coupled climate models (Gordon et al., 2000; version 4.5 of the Unified Model) that featured an interactive carbon cycle ("C") in the atmosphere, on

10   land and in the ocean. The HadGEM2 family of climate models (The HadGEM2 Development Team, 2011), a development of HadCM3 with enhanced resolution and improved parameterisations that was used for CMIP5 simulations, was version 6.6 of the Unified Model. In particular HadGEM2-ES (Collins et al., 2011), featuring active Earth System components including version 1.0 of the Diat-HadOCC sub-model, was version 6.6.3 and it is the code from that version which is described in this paper, although Diat-HadOCC v1.0 can be run with any version of HadGEM2 that features an ocean.

## 15 2   Description of the Diat-HadOCC model, version 1.0

As shown in Table 1 and Figure 1 the Diat-HadOCC model has thirteen biogeochemical state variables, representing three dissolved nutrients (nitrate, silicate and iron), two phytoplankton (diatoms and misc-Phyto; plus diatom silicate), one zooplankton, three detritus compartments (detrital nitrogen, carbon and silicon), dissolved oxygen, dissolved inorganic carbon and alkalinity. "misc-Phyto(plankton)" refers to the "Miscellaneous Phytoplankton" term used in the CMIP5 database, i.e. any phytoplankton

20   that is not specified to be a particular functional type. All the state variables are advected by the ocean currents and mixed by physical processes such as the isopycnal diffusion, diapycnal diffusion and convective mixing. The biogeochemical processes that affect the biogeochemical state variables are shown below in basic form, with greater detail on the processes given in subsequent paragraphs. In the following equations all flows are body (point) processes except those in [ square brackets ] which are biogeochemical flows across layer interfaces.

25
$$\frac{dDIN}{dt} = ph_{resp} + dm_{resp} + ph_{mort} \cdot f_{nmp} + dm_{mort} \cdot f_{nmp} + grz_{DIN} + zp_{lin} + zp_{mort} \cdot f_{zmrt}$$
$$+ dtn_{remin} + dtn_{bedrmn} - ph_{PP} - dm_{PP} \tag{1}$$

$$\frac{dSi}{dt} = dtsi_{remin} + dtsi_{bedrmn} - dm_{PP} \cdot R_{si2n}^{Dm} \tag{2}$$

$$\frac{dFeT}{dt} = ( ph_{resp} \cdot R_{c2n}^{Ph} + dm_{resp} \cdot R_{c2n}^{Dm} + ph_{mort} \cdot R_{c2n}^{Ph} + dm_{mort} \cdot R_{c2n}^{Dm} + grz_{DIC} + grz_{DtC} - dtc_{grz}$$
$$+ zp_{lin} \cdot R_{c2n}^{Zp} + zp_{mort} \cdot R_{c2n}^{Zp} - ph_{PP} \cdot R_{c2n}^{Ph} - dm_{PP} \cdot R_{c2n}^{Dm} ) \cdot R_{fe2c}^{eco} + [ fe_{dust} ] - fe_{adsorp} \tag{3}$$

30
$$\frac{dPh}{dt} = ph_{PP} - ph_{resp} - ph_{mort} - ph_{grz} \tag{4}$$

$$\frac{dDm}{dt} = dm_{PP} - dm_{resp} - dm_{mort} - dm_{grz} - [dm_{sink}] \tag{5}$$

$$\frac{dDmSi}{dt} = dm_{PP} \cdot R_{si2n}^{Dm} - dmsi_{mort} - dmsi_{grz} - [dmsi_{sink}] \tag{6}$$

$$\frac{dZp}{dt} = grz_{Zp} - zp_{lin} - zp_{mort} \tag{7}$$

$$\frac{dDtN}{dt} = ph_{mort} \cdot (1 - f_{nmp}) + dm_{mort} \cdot (1 - f_{nmp}) + grz_{DtN} + zp_{mort} \cdot (1 - f_{zmrt}) + dm_{bedmrt}$$
$$- dtn_{grz} - dtn_{remin} - [dtn_{sink}] \tag{8}$$

$$\frac{dDtSi}{dt} = dmsi_{mort} + grz_{dtsi} + dmsi_{bedmrt} - dtsi_{remin} - [dtsi_{sink}] \tag{9}$$

$$\frac{dDtC}{dt} = ph_{mort} \cdot (1 - f_{nmp}) \cdot R_{c2n}^{Ph} + dm_{mort} \cdot (1 - f_{nmp}) \cdot R_{c2n}^{Dm} + grz_{DtC} + zp_{mort} \cdot (1 - f_{zmrt}) \cdot R_{c2n}^{Zp}$$
$$+ dm_{bedmrt} \cdot R_{c2n}^{Dm} - dtc_{grz} - dtc_{remin} - [dtc_{sink}] \tag{10}$$

$$\frac{dDIC}{dt} = ph_{resp} \cdot R_{c2n}^{Ph} + dm_{resp} \cdot R_{c2n}^{Dm} + ph_{mort} \cdot f_{nmp} \cdot R_{c2n}^{Ph} + dm_{mort} \cdot f_{nmp} \cdot R_{c2n}^{Dm} + grz_{DIC}$$
$$+ zp_{lin} \cdot R_{c2n}^{Zp} + zp_{mort} \cdot f_{zmrt} \cdot R_{c2n}^{Zp} + dtc_{remin} + dtc_{bedrmn} + crbnt$$
$$- ph_{PP} \cdot R_{c2n}^{Ph} - dm_{PP} \cdot R_{c2n}^{Dm} + [CO2_{asf}] \tag{11}$$

$$\frac{dTAlk}{dt} = 2 \cdot crbnt - \frac{dDIN}{dt} \tag{12}$$

$$\frac{dOxy}{dt} = [Oxy_{asf}] - \left( \frac{dDIC}{dt} - crbnt - [CO2_{asf}] \right) \cdot R_{o2c}^{eco} \tag{13}$$

## 2.1 Growth of diatoms and misc-Phytoplankton

The growth of diatoms and misc-Phytoplankton (respectively $dm_{PP}$ and $ph_{PP}$) is a function of the availability of macro- and micro-nutrients, the temperature and the availability of light. The growth limitation by dissolved nitrate (and, in the case of Diatoms, also by dissolved silicate) in the model has a hyperbolic form, while that by dissolved iron is represented in a different way. The effect of dissolved iron ($FeT$) in the Diat-HadOCC model is to vary certain parameter values: the assimilation numbers (maximum growth rates) for diatoms and misc-Phytoplankton $P_m^{Dm}$ and $P_m^{Ph}$, the silicon:nitrogen ration for diatoms $R_{si2n}^{Dm}$, the zooplankton base preference for feeding on diatoms $bprf_{Dm}$ and the zooplankton mortality $\Pi_{mort}^{Zp}$. (Note that, because the base feeding preferences are normalised so that their sum is 1, changing the preference for diatoms will mean the preferences for misc-Phytoplankton and for detritus also change.) Each of those parameters has an iron-replete value (the standard) and an iron-deplete value, and the realised value at a given time and location will be:

$$\Pi = \Pi_{replete} + (\Pi_{deplete} - \Pi_{replete}) / \left( 1 + \frac{FeT}{k_{FeT}} \right) \tag{14}$$

where $k_{FeT}$ is similar to a half-saturation constant for iron uptake. In the CMIP5 simulations run using HadGEM2-ES (with the Diat-HadOCC model as the ocean biogeochemical component) only the value of $P_m^{Dm}$ varied (i.e. the iron-replete and -deplete values of the other parameters were set equal).

The growth-rate varies exponentially with temperature according to Equation 1 of Eppley (1972), normalised so that default rates occur at 20°C. However the Eppley study was informed by laboratory cultures, whereas in the real ocean phytoplankton show significant adaption in their growth rates to their average temperatures, so it is not clear that this relationship is valid for global populations; therefore for the CMIP5 simulations run using HadGEM2-ES the temperature variation of phytoplnkton growth-rate was switched off and the default values were used (i.e. in the equation below $f_{Temp}$ was always equal to 1.

$$P^{Ph} = \left( P_{m,r}^{Ph} + \frac{(P_{m,d}^{Ph} - P_{m,r}^{Ph})}{(1 + \frac{FeT}{k_{FeT}})} \right) \cdot MIN\left( 1.0, f_{Temp} \cdot \frac{DIN}{k_{DIN}^{Ph} + DIN} \right) \tag{15}$$

$$P^{Dm} = \left( P_{m,r}^{Dm} + \frac{(P_{m,d}^{Dm} - P_{m,r}^{Dm})}{(1 + \frac{FeT}{k_{FeT}})} \right) \cdot MIN\left( 1.0, f_{Temp} \cdot \frac{DIN}{k_{DIN}^{Dm} + DIN} \cdot \frac{Si}{k_{Si}^{Dm} + Si} \right) \tag{16}$$

In the above equations the combined effects of the temperature and the macro-nutrient concentrations is limited to a maximum factor of 1.0 to guard against excessively-fast growth if the water temperature should become very high (and the temperature factor is actively used).

### 2.1.1 The photosynthesis sub-model

The variation with light availability of the primary production of each phytoplankton type is calculated using the production scheme of Anderson (1993; hereafter TRA93). This models the preferential absorption of longer-wavelength light by seawater, so that the spectrum of light available for growth is shifted towards blue deep in the euphotic zone. Note that consequently the light calculated and used for photosynthesis in these functions at a given depth will not be the same as that available to the physics (for heating): the physics could easily be made to use the biological light field but does not do so as standard (and did not in the CMIP5 simulations). The functions also integrate production over a day, based on the noon surface irradiance and the number of daylight hours (from Equation 5 of Platt et al., 1990). This is consistent with the once-daily frequency of atmosphere-ocean coupling used in HadGEM2-ES (and previously in HadCM3C), because daily-average light is passed through the coupler and noon irradiance can easily be calculated given the daily-average and the number of daylight hours (and assuming, as Platt et al. did, that the light varies sinusoidally within the daylight hours only). Note that although the light will stay the same for each time-step between couplings the other factors determining production (e.g. phytoplankton abundance and nutrient concentration) will not, so the production is re-calculated every time-step and the appropriate proportion of daily production added to the phytoplankton state variable (e.g. 1/24 for a 1-hour time-step). When the HadOCC model (which uses the same productivity model) has been forced by 6-hourly re-analysis fluxes, for example, a daily-average irradiance field has been calculated and passed in for use in this scheme. When used in coupled models with shorter coupling periods, either a running 24-hour average of irradiance could be calculated and the scheme used as designed (and as described in the following paragraphs), or the daily integral part of the scheme could be removed and instantaneous production calculted using the remainder of the scheme.

TRA93 built on earlier work by Morel (1988,1991) which measured the absorption of light due to water and chlorophyll in 61 wavelength-bands, each 5 $nm$ wide, across the visible spectrum between 400 and 700 $nm$. Considering six typical

chlorophyll depth-profiles TRA93 showed that the changing spectrum of light with depth (due to red light being more readily absorbed than blue) could be taken into account by splitting the water-column into three depth-ranges, allowing the absorption in each depth range to be modelled by a different function of the chlorophyll concentration. It was found that the best-fitting solution put the boundaries between the ranges at $5m$ and $23m$ depth, and the parameters for the three functions published in

5 TRA93 related to those splits. However, since the physical ocean model in HadGEM2-ES (and also in previous Met Office GCMs, including HadCM3) has layer interfaces at $10m$ and $20m$ the scheme was re-parameterised for depth-range boundaries at those depths, and the model described here uses those new values.

Using the notation of TRA93, the spectrally-averaged vertical attenuation coefficient for layer $n$ within depth-range $L$, $k_n$ (units: $m^{-1}$), is given by that paper's Equation 16:

10
$$k_n = b_{0,L} + b_{1,L} \cdot c_n + b_{2,L} \cdot c_n^2 + b_{3,L} \cdot c_n^3 + b_{4,L} \cdot c_n^4 + b_{5,L} \cdot c_n^5 \tag{17}$$

where $c_n$ is the square-root of $G_n$, the total pigment concentration in layer $n$ (units: $mg\ m^{-3}$), and the re-parameterised coefficient values $b_{i,L}$ are given in Table 2. TRA93 assumed the chlorophyll biomass is always 80% of the total pigment biomass $G$ (the remainder being pheophytin) and the HadOCC and Diat-HadOCC models make the same assumption.

A derived parameter $a^{\#}$, required to calculate light absorption by phytoplankton, is then calculated by finding its surface

15 value $a_{s,G}^{\#}$ (TRA93 Equation 20) and integrating down the water-column, $\frac{da^{\#}}{dz}$ being parameterised in terms of $c$ and the depth $z$ (TRA93 Equations 21-23). The paper's equations allow for the pigment concentration to have a depth-profile that varies continuously with depth, but as implemented in Met Office GCMs the concentration is taken as being constant within a model layer and changing suddenly at the depth-interfaces. TRA93 showed that this requires an offset to $a^{\#}$ when crossing between model layers: this offset is equal to the difference between $a_{s,G}^{\#}$ calculated using the $G$ for each layer.

20 The calculation (in layer $n$) of the model variable $astar_n$, which corresponds to $a^{\#}$ in TRA93, is performed layer-by-layer, stepping down from the surface; the value is calculated at the mid-point of each layer:

$$astar_1 \quad = \quad astar0_0 + 0.5 \cdot dastar_1 \qquad\qquad (n=1) \tag{18}$$

$$astar_n \quad = \quad astar_{n-1} + (dastar_{n-1} + dastar_n)/2 + astar0_n - astar0_{n-1} \qquad (n>1) \tag{19}$$

where $astar_1$ is the model variable corresponding to TRA93's $a_{L=1}^{\#}$, $astar0_0 = astar0_1$ and corresponds to $a_{s,G_1}^{\#}$, $dastar_1$

25 corresponds to $\frac{da^{\#}}{dz}(c,\nu)$ integrated over depth from the top to the bottom of layer 1 and where

$$astar0_n \quad = \quad 0.36796 + 0.17537c_n - 0.065276c_n^2 + 0.013528c_n^3 - 0.0011108c_n^4 \tag{20}$$

$$dastar_n \quad = \quad (gcof_1 + gcof_2 \cdot c_n + gcof_3 \cdot c_n^2 + gcof_4 \cdot c_n^3) \cdot DLCO0_n + (gcof_5 + gcof_6 \cdot c_n$$
$$\qquad\qquad + gcof_7 \cdot c_n^2) \cdot DLCO1_n + (gcof_8 + gcof_9 \cdot c_n) \cdot DLCO2_n + gcof_{10} \cdot DLCO3_n \tag{21}$$

$$c_n \quad = \quad G_n^{0.5}$$

30
$$\qquad = \quad 1.25 \left( \frac{w_C \cdot R_{c2n}^{Ph}}{R_{c2chl}^{Ph}} \cdot Ph + \frac{w_C \cdot R_{c2n}^{Dm}}{R_{c2chl}^{Dm}} \cdot Dm \right) \tag{22}$$

Geoscientific
Model Development
Discussions

$$DLCO0_n = \nu_n - \nu_{n-1} \tag{23}$$

$$DLCO1_n = (\nu_n \cdot \log(\nu_n) - \nu_n) - (\nu_{n-1} \cdot \log(\nu_{n-1}) - \nu_{n-1}) \tag{24}$$

$$DLCO2_n = (\nu_n \cdot (\log(\nu_n))^2 - 2\nu_n \cdot \log(\nu_n) + 2\nu_n) - (\nu_{n-1} \cdot (\log(\nu_{n-1}))^2 - 2\nu_{n-1} \cdot \log(\nu_{n-1}) + 2\nu_{n-1}) \tag{25}$$

$$DLCO3_n = (\nu_n \cdot (\log(\nu_n))^3 - 3\nu_n \cdot (\log(\nu_n))^2 + 6\nu_n \cdot \log(\nu_n) - 6\nu_n) - (\nu_{n-1} \cdot (\log(\nu_{n-1}))^3$$
$$-3\nu_{n-1} \cdot (\log(\nu_{n-1}))^2 + 6\nu_{n-1} \cdot \log(\nu_{n-1}) - 6\nu_{n-1}) \tag{26}$$

$$\nu_n = 1 + Z_n$$

In the above equations $R_{c2chl}^{Ph}$ is the carbon to chlorophyll ratio (units: mgC mgChl$^{-1}$), which is either calculated according to Equation 33 or fixed, $w_C$ is the molecular weight of carbon, 12.01 mg Mol$^{-1}$, and $Z_n$ is the depth (in metres) of the base of layer n, with $Z_0 = 0.0$m. Note that the $gcof$ coefficients relate to the 'g' coefficients in TRA93's Equations 18 and 21, but are numbered in a different order, as shown in Table 3; in TRA93 they were ordered by the total exponent of $c$ and $\nu$ combined, but the Diat-HadOCC model (like the HadOCC model) orders them by the exponent of $\nu$.

Based on TRA93's Equation 29 (itself derived from work described in Platt et al., 1990) the primary production for each phytoplankton type ($Dm$ or $Ph$) in layer n during a whole day can then be calculated using a fitted 5th-order polynomial. In that equation, a quantity shown as ($\alpha_{max}^B \cdot a_n^{\#} \cdot I_{n,\Phi,1}/P_m^B$) is calculated; Platt et al.'s polynomial is fitted for values of that quantity between 0.0 and 15.8 and the fitted function oscillates wildly outside that range, but in the model the value of the corresponding quantity can be larger than 15.8. Therefore a rational function with non-oscilliatory behaviour was calculated (Geoff Evans, pers. comm) which matches the 5th-order polynomial at an input of 15.8 in both value and first derivative, and this is used for higher input values. For phytoplankton type $X$ and layer n (of thickness $\Delta_n$):

$$solbio_n = solbio_{n-1} \cdot exp(-k_n \cdot \Delta_n) \tag{27}$$

$$psmaxs_n^X = P_n^X \cdot R_{c2chl}^X / 24 \tag{28}$$

$$V_a = \alpha_{mx}^X \cdot astar_n / psmaxs_n^X \tag{29}$$

$$V_b = V_a \cdot solbio_{n-1}$$

$$V_c = V_a \cdot solbio_n$$

$$V_d = MIN(15.8, V_b)$$

$$V_e = MIN(15.8, V_c)$$

$$V_f = MAX(15.8, V_b)$$

$$V_g = MAX(15.8, V_c)$$

$$psynth_n^X = \sum_{i=1}^{5} \Omega_i [V_d^i - V_e^i] + \left( \frac{V_f \cdot (\gamma_1 + \gamma_2 \cdot V_f)}{(1.0 + \gamma_3 \cdot V_f)} - \frac{V_g \cdot (\gamma_1 + \gamma_2 \cdot V_g)}{(1.0 + \gamma_3 \cdot V_g)} \right) \tag{30}$$

The values of the coefficients $\Omega$ and $\gamma$ are given in Table 4. In the above equations, $\alpha_{mx}^X$ is the maximum photosynthetic efficiency ($\alpha_{max}^B$ in TRA93) and has the value 2.602 times $\alpha^X$, the initial slope of the photosynthesis-light curve (Equation 26

in TRA93). $P_n^X$ is the maximum growth rate for the phytoplankton type and layer, taking into account the temperature and the nutrient limitations, as calculated in Equations 15 and 16. $solbio_0$ is the solar radiance just below the ocean surface. The total daily production in that layer is then:

$$ph_{PP} = Ph \cdot \frac{dlh \cdot P^{Ph}}{\pi \cdot k \cdot \Delta} \cdot psynth^{Ph} \tag{31}$$

$$dm_{PP} = Dm \cdot \frac{dlh \cdot P^{Dm}}{\pi \cdot k \cdot \Delta} \cdot psynth^{Dm} \tag{32}$$

where $dlh$ is the number of daylight hours at that location and time of year and $k$ is the attenuation coefficient calculated in Equation 17. All terms in these equations (except $dlh$ and the constant $\pi$) vary between layers. Where a number of layers are part of a surface mixed layer at a given time-step the production in those layers is averaged over those layers.

### 2.1.2 Carbon-to-chlorophyll ratio

The carbon to chlorophyll ratio for each phytoplankton type, $R_{c2chl}^X$, can either be prescribed or updated using a scheme based on Geider et al. (1996,1997,1998). In the CMIP5 simulations run using HadGEM2-ES the constant values $R_{c2chl,0}^X$ shown in Table 5 were used. However, for completeness the time-varying scheme as implemented in the Diat-HadOCC model is described briefly.

Re-arranging Equations A1-A5 in Geider et al. (1997; hereafter G97) produces (using that paper's notation, including $\theta = (chl/C)$, so corresponding to the reciprocal of the ratio used in this model):

$$\frac{d\theta}{dt} = \frac{k_{chl}}{\theta} \cdot \frac{(P_m^C)^2}{\alpha^{chl}I} \cdot \left(1 - exp\left(\frac{-\alpha^{chl}I\theta}{P_m^C}\right)\right) - \theta \cdot \left(P_m^C \cdot \left(1 - exp\left(\frac{-\alpha^{chl}I\theta}{P_m^C}\right)\right) - (R^{chl} - R^C)\right) \tag{33}$$

where G97's $P_m^C$ corresponds to this model's $P^X$, $\alpha^{chl}$ corresponds to $\alpha_{mx}^X \cdot astar$, $I$ is the irradiance (in the middle of the layer) and $R^{chl}$ and $R^C$ are respectively the specific removal rates of chlorophyll and carbon from the phytoplankton. Finally, $K_{chl}$ is the 'maximum proportion of photosynthesis that can be directed to chl a synthesis', but in a number of conditions is equal to the maximum $(chl/C)$ ratio, and in this model it is represented by $1/R_{c2chl,min}^X$.

The equation above has no analytical solution for $\theta$, and it is intended that the model should be able to operate with long time-steps if required (up to 1 day), so a semi-implicit finite-difference solution was found. $\frac{d\theta}{dt}$ is represented as $(\theta_{t+1} - \theta_t)/\delta t$, and the $\theta$s inside the exponents take the value $\theta_t$ (i.e. the reciprocal of the value of $R_{c2chl}^X$ from the previous time-step) while those outside take the value $\theta_{t+1}$. $R^C$ is set equal to $\Pi_{resp}^X + \Pi_{mort}^X \cdot X$ (where $X$ is $Ph$ or $Dm$ as appropriate), and $R^{chl}$ is set equal to $R^C$ (so the difference is zero). Then a simple re-arrangement results in a quadratic equation in $\theta_{t+1}$ which can be easily solved. The updated value of $R_{c2chl}^X$ is then the reciprocal of the resulting $\theta$ (though it can be necessary on occasions to apply upper and lower bounds to the ratio, respectively $R_{c2chl,max}^X$ and $R_{c2chl,min}^X$). Ratios calculated in layers that are part of the surface mixed layer are averaged. As implemented, the ratio is stored from one time-step to the next and not advected or mixed as a tracer; the change in the ratio due to biological processes is much larger than that due to mixing with the ratio in adjacent grid boxes. It would be possible to use the ratio and the concentration of the appropriate phytoplankton type to create a phytoplankton-chlorophyll state variable which could be advected and mixed as a tracer, but that is not how the scheme is currently used in the Diat-HadOCC model.

Geoscientific
Model Development
Discussions

## 2.2 Zooplankton grazing

The grazing function used in the Diat-HadOCC model differs from that used in the HadOCC model in that it uses a 'switching' grazer similar to that used in Fasham et al. (1990; hereafter FDM90). The single zooplankton consumes diatoms, misc-Phytoplankton and (organic) detrital particles. As in FDM90 the realised preference $dprf_X$ for each food type depends on that
5   type's abundance and on the base preferences $bprf_X$:

$$dprf_{denom} = bprf_{Dm} \cdot R_{b2n}^{Dm} \cdot Dm + bprf_{Ph} \cdot R_{b2n}^{Ph} \cdot Ph + bprf_{Dt} \cdot (R_{b2n}^{DtN} \cdot DtN + R_{b2c}^{DtC} \cdot DtC) \tag{34}$$

$$dprf_{Dm} = \frac{bprf_{Dm} \cdot R_{b2n}^{Dm} \cdot Dm}{dprf_{denom}} \tag{35}$$

$$dprf_{Ph} = \frac{bprf_{Ph} \cdot R_{b2n}^{Ph} \cdot Ph}{dprf_{denom}} \tag{36}$$

$$dprf_{Dt} = \frac{bprf_{Dt} \cdot (R_{b2n}^{DtN} \cdot DtN + R_{b2c}^{DtC} \cdot DtC)}{dprf_{denom}} \tag{37}$$

10   where, if $M_N$ and $M_C$ are the respective atomic weights of nitrogen and carbon (14.01 and 12.01 g Mol$^{-1}$) and $R_{c2n}^{Rdfld}$ is the Redfield C:N ratio (106 Mol C : 16 Mol N), then the $R_{b2Y}^{X}$ terms convert from nitrogen or carbon units to biomass units that allow the various potential food items to be compared:

$$E = (M_N + M_C \cdot R_{c2n}^{Rdfld})^{-1}$$

$$R_{b2n}^{Ph} = E \cdot (M_N + M_C \cdot R_{c2n}^{Ph}) \tag{38}$$

15   $$R_{b2n}^{Dm} = E \cdot (M_N + M_C \cdot R_{c2n}^{Dm}) \tag{39}$$

$$R_{b2n}^{Zp} = E \cdot (M_N + M_C \cdot R_{c2n}^{Zp}) \tag{40}$$

$$R_{b2n}^{DtN} = E \cdot M_N \tag{41}$$

$$R_{b2c}^{DtC} = E \cdot M_C \tag{42}$$

Note that the base preference values supplied (or calculated as a function of iron-limitation) $bprf_X$ are normalised so that they
20   sum up to 1. The available food is:

$$food = dprf_{Dm} \cdot R_{b2n}^{Dm} \cdot Dm + dprf_{Ph} \cdot R_{b2n}^{Ph} \cdot Ph + dprf_{Dt} \cdot (R_{b2n}^{DtN} \cdot DtN + R_{b2c}^{DtC} \cdot DtC) \tag{43}$$

and the grazing rates on the various model state variables are:

$$dm_{grz} = \frac{dprf_{Dm} \cdot Dm \cdot g_{max} \cdot R_{b2n}^{Zp} \cdot Zp}{g_{sat} + food} \tag{44}$$

$$dmsi_{grz} = \frac{dprf_{Dm} \cdot DmSi \cdot g_{max} \cdot R_{b2n}^{Zp} \cdot Zp}{g_{sat} + food} \tag{45}$$

25   $$ph_{grz} = \frac{dprf_{Ph} \cdot Ph \cdot g_{max} \cdot R_{b2n}^{Zp} \cdot Zp}{g_{sat} + food} \tag{46}$$

$$dtn_{grz} = \frac{dprf_{Dt} \cdot DtN \cdot g_{max} \cdot R_{b2n}^{Zp} \cdot Zp}{g_{sat} + food} \tag{47}$$

$$dtc_{grz} = fracdprf_{Dt} \cdot DtC \cdot g_{max} \cdot R_{b2n}^{Zp} \cdot Zpg_{sat} + food \tag{48}$$

A fraction $(1 - f_{ingst})$ of the grazed material is not ingested: of this, a fraction $f_{messy}$ returns immediately to solution as $DIN$ and $DIC$ while the rest becomes detritus. All of the grazed diatom silicate $DmSi$ immediately becomes detrital silicate $DtSi$. Of the organic material that is ingested, a source-dependent fraction $(\beta^X)$ of the nitrogen and of the carbon is assimilatable while the remainder is egested from the zooplankton gut as detrital nitrogen $DtN$ or carbon $DtC$. The amount of assimilatable material that is actually assimilated by the zooplankton $grz_{Zp}$ is governed by its C:N ratio compared to that of the zooplankton: as much as possible is assimilated, with the remainder passed out immediately as $DIN$ or $DIC$.

$$assim_N \quad = \quad f_{ingst} \cdot (\beta^{Dm} \cdot dm_{grz} + \beta^{Ph} \cdot ph_{grz} + \beta^{Dt} \cdot dtn_{grz}) \tag{49}$$

$$assim_C \quad = \quad f_{ingst} \cdot (\beta^{Dm} \cdot R_{c2n}^{Dm} \cdot dm_{grz} + \beta^{Ph} \cdot R_{c2n}^{Ph} \cdot ph_{grz} + \beta^{Dt} \cdot dtn_{grz}) \tag{50}$$

$$grz_{Zp} \quad = \quad MIN\left(assim_N, \frac{assim_C}{R_{c2n}^{Zp}}\right) \tag{51}$$

$$grz_{DtN} \quad = \quad (1 - f_{ingst}) \cdot (1 - f_{messy}) \cdot (dm_{grz} + ph_{grz} + dtn_{grz})$$
$$+ f_{ingst} \cdot ((1 - \beta^{Dm}) \cdot dm_{grz} + (1 - \beta^{Ph}) \cdot ph_{grz} + (1 - \beta^{Dt}) \cdot dtn_{grz}) \tag{52}$$

$$grz_{DtC} \quad = \quad (1 - f_{ingst}) \cdot (1 - f_{messy}) \cdot (R_{c2n}^{Dm} \cdot dm_{grz} + R_{c2n}^{Ph} \cdot ph_{grz} + dtc_{grz})$$
$$+ f_{ingst} \cdot ((1 - \beta^{Dm}) \cdot R_{c2n}^{Dm} \cdot dm_{grz} + (1 - \beta^{Ph}) \cdot R_{c2n}^{Ph} \cdot ph_{grz} + (1 - \beta^{Dt}) \cdot dtc_{grz}) \tag{53}$$

$$grz_{dtsi} \quad = \quad dmsi_{grz} \tag{54}$$

$$grz_{DIN} \quad = \quad (1 - f_{ingst}) \cdot f_{messy} \cdot (dm_{grz} + ph_{grz} + dtn_{grz}) + MAX\left(0, assim_N - \frac{assim_C}{R_{c2n}^{Zp}}\right) \tag{55}$$

$$grz_{DIC} \quad = \quad (1 - f_{ingst}) \cdot f_{messy} \cdot (R_{c2n}^{Dm} \cdot dm_{grz} + R_{c2n}^{Ph} \cdot ph_{grz} + dtc_{grz})$$
$$+ MAX(0, assim_C - assim_N \cdot R_{c2n}^{Zp}) \tag{56}$$

## 2.3 Other processes

The other loss terms for diatoms, misc-Phytoplankton and zooplankton are:

$$dm_{resp} \quad = \quad \Pi_{resp}^{Dm} \cdot Dm \tag{57}$$

$$ph_{resp} \quad = \quad \Pi_{resp}^{Ph} \cdot Ph \tag{58}$$

$$dm_{mort} \quad = \quad \Pi_{mort}^{Dm} \cdot Dm^2 \tag{59}$$

$$dmsi_{mort} \quad = \quad \Pi_{mort}^{Dm} \cdot Dm \cdot DmSi \tag{60}$$

$$ph_{mort} \quad = \quad \Pi_{mort}^{Ph} \cdot Ph^2 \qquad\qquad (Ph > ph_{min})$$
$$= \quad 0 \qquad\qquad\qquad\qquad (Ph < ph_{min}) \tag{61}$$

$$zp_{lin} \quad = \quad \Pi_{lin}^{Zp} \cdot Zp \tag{62}$$

$$zp_{mort} \quad = \quad \Pi_{mort}^{Zp} \cdot Zp^2 \tag{63}$$

### 2.3.1 Detrital sinking and remineralisation

All detrital material sinks at a constant speed $V_{Dt}$ at all depths. Diatoms (and its associated silicate) sinks at a constant speed $V_{Dm}$ at all depths. Detrital remineralisation (of $DtN$ and $DtC$)is depth-dependent, the specific rate varying as the reciprocal of depth but with a maximum value. This functional form gives a depth variation of detritus consistent with the Martin et al. (1987) power-law curve. Dissolution of opal does not vary with depth.

$$dtn_{remin} = DtN \cdot MIN\left(\Pi_{rmnmx}^{DtN}, \frac{\Pi_{rmndd}^{DtN}}{z}\right) \tag{64}$$

$$dtc_{remin} = DtC \cdot MIN\left(\Pi_{rmnmx}^{DtC}, \frac{\Pi_{rmndd}^{DtC}}{z}\right) \tag{65}$$

$$dtsi_{remin} = DtSi \cdot \Pi_{rmn}^{DtSi} \tag{66}$$

$$dt(n,c,si)_{sink} = V_{Dt} \cdot \frac{d\,Dt(N,C,Si)}{d\,z} \tag{67}$$

$$d(m,msi)_{sink} = V_{Dm} \cdot \frac{d\,D(m,mSi)}{d\,z} \tag{68}$$

Since there are no sediments in the Diat-HadOCC model, all detritus that sinks to the sea-floor is instantly remineralised to N, C or Si and spread through the lowest three layers (above the sea-floor). Diatoms (and associated silicate) that sink to the sea-floor instantly die and become $DtN$, $DtC$ and $DtSi$, as appropriate, in the lowest layer. Therefore, if $btmflx_Y$ is the value of $[Y_{sink}]$ at the sea-floor:

$$
\begin{aligned}
dt(n,c,si)_{bedrmn} &= \frac{btmflx_{Dt(N,C,Si)}}{\Delta_{b3l}} & (btm\,3\,lyrs) \\
&= 0 & (above\,btm\,3\,lyrs)
\end{aligned}
\tag{69}
$$

$$
\begin{aligned}
(dm,dmsi)_{bedmrt} &= \frac{btmflx_{(dm,dmsi)}}{\Delta_{b1l}} & (bottom\,lyr) \\
&= 0 & (other\,lyrs)
\end{aligned}
\tag{70}
$$

where $btmflx_X$ is the sinking flux of $X$ to the sea-floor and $\Delta_{bMl}$ is the combined thickness of the bottom $M$ layers (of course, which layers those are will vary according to the location).

### 2.3.2 The iron cycle

Iron is added to the ocean by dust deposition from the atmosphere (prescribed or passed from the atmospheric sub-model in coupled mode), with a constant proportion (by weight) of the dust being iron which immediately becomes part of the total dissolved iron pool $FeT$. Iron is taken up by diatoms and misc-Phytoplankton during growth in a fixed ratio to the carbon taken up, and moves through the ecosystem in the same ratio, except that any flow of carbon to $DtC$ is associated with a flow of iron back to solution, as there is no iron in organic detritus in the model. All iron that flows through the ecosystem is returned to solution, but there is a final loss term for dissolved iron, namely (implicit) adsorption onto pelagic sinking mineral particles (*not* the model's detrital particles) and thence to the (implicit) sediments. Only the fraction of $FeT$ that is not complexed to organic ligands can be adsorbed. The un-complexed (free) iron concentration $FeF$ and the complexed concentration $FeL$ are

found by assuming a constant uniform total ligand concentration $LgT$ and a partition function $K_{FeL}$, and the adsorption flux $fe_{adsorp}$ derived from that:

$$FeT = FeL + FeF \tag{71}$$

$$LgT = FeL + LgF \tag{72}$$

$$K_{FeL} = \frac{FeL}{FeF \cdot LgF} \tag{73}$$

$$B = K_{FeL} \cdot (LgT - FeT) - 1 \tag{74}$$

$$FeF = FeT - LgT + \frac{1}{2 \cdot K_{FeL}} \cdot \left( B + \sqrt{B^2 - 4 \cdot K_{FeL} \cdot LgT} \right) \tag{75}$$

$$fe_{adsorp} = \Pi_{ads}^{FeF} \cdot FeF \tag{76}$$

### 2.3.3 The calcium carbonate sub-model

Solid calcium carbonate is implicitly produced in a constant ratio to organic production by misc-Phytoplankton. The total production is summed over the surface layers (those where production is non-zero) and instantly re-dissolved equally through the water column below the (prescribed) lysocline. If the sea-floor is shallower than the lysocline, then the dissolution takes place in the bottom layer (there being no sediments). The depth of the lysocline is always co-incident with a layer interface, and is constant both geographically and in time.

$$ccfrmtn = R_{cc2pp}^{Ph} \cdot ph_{PP} \tag{77}$$

$$xprt_{cc} = \sum_n (ccfrmtn_n \cdot \Delta_n) \tag{78}$$

$$ccdsltn = \frac{xprt_{cc}}{\Delta_{dsl}} \qquad (valid\,lyrs\,)$$

$$= 0 \qquad (other\,lyrs\,) \tag{79}$$

$$crbnt = ccdsltn - ccfrmtn \tag{80}$$

where $\Delta_n$ is the thickness of layer $n$ and $\Delta_{dsl}$ is the total thickness of the valid layers (where dissolution can occur) in that water column, which is equal to the distance between the lysocline and the sea-floor if the lysocline is shallower than the sea-floor and the thickness of the deepest layer otherwise.

### 2.3.4 Air-Sea fluxes

Finally, the calculation of the air-to-sea fluxes of $O_2$ and $CO_2$ (respectively $[Oxy_{asf}]$ and $[CO2_{asf}]$) follow the methodology of OCMIP. The flux is the product of the gas-specific gas transfer (piston) velocity $Vp$ and the difference between the gas concentrations in the atmosphere (just above the sea-surface), $X_{sat}$, and in the (surface) ocean, $X_{surf}$: $X_{asf} = Vp_X \cdot (X_{sat} - X_{surf})$. The piston velocity (in m/s) is a function of the 10m wind-speed, $U$ (using the Wanninkhof 1992 formulation, normalised for a Schmidt number of 660), the gas-specific Schmidt number $Sch$ and the fraction of the

grid-box area that is open water $A_{ow}$:

$$Vp_X = A_{ow} \cdot (f_U \cdot U^2 \times 0.01/3600.0) \cdot (Sch_X/660)^{-1/2} \qquad (81)$$

where $f_U$ is a coefficient taking the value 0.31 if wind-speed averaged over a day or less is used (e.g. in a coupled model) or
0.39 if monthly-mean wind-speed is used (Wanninkhof, 1992).

5    In the case of oxygen $O_{2,surf}$ is the model oxygen concentration, while the surface ocean is assumed to be fully saturated in equilibrium so $O_{2,sat}$ is equal to the solubility $C_O$ (calculated in units of ml/l, and converted to model units before use). That is calculated using Equation 8 of (Garcia and Gordon, 1992), but removing the spurious "$A_3 \cdot T_s^2$" term found at the end of the first line (as in the o2sato.f subroutine in the OCMIP-2 Biotic-HOWTO documentation, available at http://ocmip5.ipsl.jussieu.fr/OCMIP/phase2/simulations/Biotic/boundcond/o2sato.f). The solubility coefficients used in the

10   OCMIP-2 subroutine, originally from Benson and Krause (1984) and recommended by Garcia and Gordon (1992), are used here. Note that in HadGEM2-ES the sea-level pressure is assumed to be always 1 atmosphere, everywhere. Therefore the equation is:

$$
\begin{aligned}
C_O \quad = \quad & exp(2.00907 + 3.22014T_s + 4.05010T_s^2 + 4.94457T_s^3 - 0.256847T_s^4 + 3.88767T_s^5 \\
& - S \cdot (6.24523 + 7.37614T_s + 10.3410T_s^2 + 8.17083T_s^3) \times 10^{-3} - 4.88682 \times 10^{-3} \cdot S^2)
\end{aligned}
\qquad (82)
$$

15   where sea-surface temperature $T$ has units of $°C$, salinity $S$ has units of permil and where $T_s = ln[(298.15 - T)(273.15 + T)^{-1}]$.
$C_O$ can be converted to units of mol/m$^3$ by dividing by the molar volume, 22.3916 l/mol. The Schmidt number is calculated according to Keeling et al. (1998):

$$Sch_{O2} = 1638.0 - 81.83T_l + 1.483T_l^2 - 0.008004T_l^3 \qquad (83)$$

where $T_l = max(-2.0, min(40.0, T))$, protecting the calculation from crashing if the physical ocean model should produce

20   unreasonably low or high sea-surface temperatures.

In the case of carbon dioxide $CO_{2,sat} = C_{CO2} \cdot pCO_{2,atm}$ where $C_{CO2}$ is the $CO_2$ solubility and $pCO_{2,atm}$ is the partial pressure of $CO_2$ in dry air at 1 atmosphere pressure in the atmospheric level immediately above the ocean surface (note again that the sea-level pressure is always assumed to be 1 atmosphere). The solubility is that due to Weiss (1974):

$$C_{CO2} = exp(93.4517/T_h - 60.2409 + 23.3585 \cdot ln(T_h) + S \cdot (0.023517 - 0.023656T_h + 0.0047036T_h^2)) \qquad (84)$$

25   where $T_h = max(2.71, (273.15 + T)/100.0)$ (protecting the calculation from any spuriously-low sea-surface temperatures the physical model might produce). The Schmidt number for $CO_2$ is calculated according to Wanninkhof (1992):

$$Sch_{CO2} = 2073.1 - 125.62T_l + 3.6276T_l^2 - 0.043219T_l^3 \qquad (85)$$

where $T_l$ is defined as in the calculation for $Sch_{O2}$.

The calculation of $CO_{2,surf}$ has to take into account the partitioning of $DIC$ into three forms, namely carbonic acid (taken

30   here to include the dissolved gas phase), bicarbonate ion and carbonate ion, only the first of which contributes to the air-to-sea

flux:

$$DIC = [H_2CO_3] + [HCO_3^-] + [CO_3^{2-}] \tag{86}$$

The calculation of the partitioning, which follows the method described by Bacastow (1981), requires as inputs the total Alkalinity $A_T$ and the DIC concentration $DIC$, the temperature, the salinity and the total boron concentration. The method involves using an earlier estimate of the hydrogen ion concentration $[H^+]_I$ to calculate the carbonate alkalinity $A_C = A_T - f([H^+]_I)$, which is then used with $DIC$ to set up a quadratic equation in $[H^+]$. Bacastow (1981) then used the secant method of similar triangles (Acton, 1970) is used to minimise the difference between successive estimates.

Four equilibrium constants describing the dissociation of carbonic acid ($K_1$, from Roy et al. 1993), bicarbonate ion ($K_2$, also from Roy et al. 1993), boric acid ($K_B$, from Dickson 1990) and water ($K_W$, from Millero 1995) are calculated (in moles/kg):

$$
\begin{aligned}
K_1 &= \frac{[H^+][HCO_3^-]}{[H_2CO_3]} \tag{87}\\
&= (1 - 0.001005S) \cdot exp(-2307.1266/T_k + 2.83655 - 1.5529413ln(T_k) \\
&\quad -(4.0484/T_k + 0.20760841) \cdot S^{1/2} + 0.08468345S - 0.00654208S^{3/2}) \tag{88}\\
K_2 &= \frac{[H^+][CO_3^{2-}]}{[HCO_3^-]} \tag{89}\\
&= (1 - 0.001005S) \cdot exp(-3351.6106/T_k - 9.226508 - 0.2005743ln(T_k) \\
&\quad -(23.9722/T_k + 0.106901773) \cdot S^{1/2} + 0.1130822S - 0.00846934S^{3/2}) \tag{90}\\
K_B &= \frac{[H^+][B(OH)_4^-]}{[B(OH)_3]} \tag{91}\\
&= exp(-(8966.90 + 2890.53S^{1/2} + 77.942S - 1.728S^{3/2} + 0.0996S^2)/T_k \\
&\quad +(148.0248 + 137.1942S^{1/2} + 1.62142S) - (24.4344 + 25.085S^{1/2} + 0.2474S) \cdot ln(T_k) \\
&\quad +0.053105S^{1/2} \cdot T_k) \tag{92}\\
K_W &= [H^+][OH^-] \tag{93}\\
&= exp(-13847.26/T_k + 148.96502 - 23.6521ln(T_k) \\
&\quad +(118.67/T_k - 5.977 + 1.0495ln(T_k)) \cdot S^{1/2} - 0.01615S) \tag{94}
\end{aligned}
$$

where $T_k = T + 273.15°C$ is the temperature in Kelvin and S the salinity in per mil. Note that, because these constants are in units of Moles/kg-seawater (strictly, (Moles/kg-seawater)$^2$ in the case of $K_W$), the alkalinity and DIC state variables must be converted to those units from the model units of mMoles/m$^3$ before the partitioning is calculated; all state variables in the converted units have the subscript $u$ (e.g. $A_{T,u}$).

The total borate concentration $B_T$ (in Moles/kg) is set to be proportional to the salinity: $B_T = [B(OH)_3] + [B(OH)_4^-] = 4.16e^{-4}S/35.0$. Then, since the Diat-HadOCC model uses the 5-term expression for total alkalinity (Bacastow, 1981), the carbonate alkalinity is calculated as:

$$A_{C,u} = [HCO_3^-] + 2[CO_3^{2-}] \tag{95}$$

$$= A_{T,u} - Z_W \cdot \chi_{x,i} + Z_p/\chi_{x,i} - B_T/\left(1 + \frac{Z_b}{\chi_{x,i}}\right) \tag{96}$$

where

$$Z_p = \sqrt{K_1 \cdot K_2} \tag{97}$$

$$Z_r = \sqrt{\frac{K_1}{K_2}} \tag{98}$$

$$Z_B = \frac{Z_p}{K_B} \tag{99}$$

$$Z_W = \frac{K_W}{Z_p} \tag{100}$$

$$\chi = \frac{Z_p}{[H^+]} \tag{101}$$

Equations 86 and 95 can be re-arranged and combined with equations 87, 89, 97, 98 and 101 to give:

$$(2DIC_u - A_{C,u}) \cdot \chi_{y,i}^2 - Z_r \cdot (A_{c,u} - DIC_u) \cdot \chi_{y,i} - A_{C,u} = 0 \tag{102}$$

which has the solution

$$\chi_{y,i} = 0.5(Z_r \cdot (A_{c,u} - DIC_u) + \sqrt{(Z_r^2 \cdot (A_{c,u} - DIC_u)^2 + 4A_{C,u} \cdot (2DIC_u - A_{C,u}))})/(2DIC_u - A_{C,u}) \tag{103}$$

When $\chi_{y,i}$ and $\chi_{x,i}$ are equal the value of $\chi$ that is consistent with both the $A_{C,u}$ and the $DIC_u$ values (for the current temperature and salinity) has been found, so $[H_2CO_3]$ can be found from equations 86, 87 and 89. While the two estimates of $\chi$ are not equal however, the secant method of similar triangles (Acton, 1970) is used to find an updated estimate $\chi_{x,i+1}$ for input into the next iteration of equation 96 by minimising $\chi_y - \chi_x$. The two similar triangles are right-angled and have sides of length $(\chi_{x,i+1} - \chi_{x,i}, \chi_{y,i} - \chi_{x,i})$ and $(\chi_{x,i+1} - \chi_{x,i-1}, \chi_{y,i-1} - \chi_{x,i-1})$ respectively; equating the ratios of these two triangles' sides and re-arranging gives

$$\chi_{x,i+1} = \frac{\chi_{x,i-1} \cdot \chi_{y,i} - \chi_{x,i} \cdot \chi_{y,i-1}}{(\chi_{y,i} - \chi_{y,i-1}) - (\chi_{x,i} - \chi_{x,i-1})} \tag{104}$$

This calculation can be iterated until the fractional change in successive estimates is less than a certain amount (e.g. $10^{-5}$). However, in the implementation used for HadGEM2-ES the calculation was iterated eight times; it had been found that the convergence criterion was always satisfied in 6 iterations, and given the computer architecture it was more computationally efficient to run that way than to repeatedly test for convergence.

Once the carbonic acid concentration has been determined (and converted back to model units) it can be used as $CO_{2,surf}$ in the air-sea flux calculation. Other diagnostic quantities can also be calculated: $pCO_2$ and $pH$ (the latter from the H$^+$ concentration).

## 3  Description of experiments

The Diat-HadOCC model formed the ocean biogeochemical component of the HadGEM2-ES Earth System model (Collins et al., 2011), which is part of the HadGEM2 family of coupled climate models (The HadGEM2 Development Team, 2011). Full details of the model set-up for the experiments described here can be found in those references, but a brief descrip-
5  tion is given here.

The atmospheric physical model has a horizontal resolution of 1.25° latitude by 1.875° longitude, and a vertical resoltion of 38 layers (to a height of 39 km). A timestep of 30 minutes is used. Eight species of aerosol are included in the atmosphere, as well as a representation of mineral dust (described in more detail below). The UK Chemistry and Aerosols (UKCA) model (O'Connor et al., 2014) describes the atmospheric chemistry. MOSES II (Essery et al., 2003) is used for the land surface
10  scheme, with additional processes and components as described in papers about the derived JULES scheme by Best et al. (2011) and Clark et al. (2011). The hydrology includes a river-routing sub-model based on the TRIP scheme (Oki and Sud, 1998), which supplies freshwater (but not nutrients, carbon or alkalinity) to the ocean. The TRIFFID dynamic vegetation model (Cox, 2001; Clark et al. 2011) and a four-pool implementation of the RothC soil carbon model (Coleman and Jenkinson 1996,1999) are used to represent the terrestrial carbon cycle. TRIFFID calculates the growth and phenology of five plant
15  functional types (broad-leaf trees, needle-leaf trees, C3 grasses, C4 grasses and shrubs) so that the (terrestrial) Gross Primary Production (GPP), and the Net Primary Production (NPP) can be determined, and thereby also the terrestrial sources and sinks of atmospheric carbon.

The ocean physical model is based on that described in Johns et al. (2006), with developments as detailed in the paper by The HadGEM2 Development Team (2011). It has a longitudinal resolution of 1°, while the latitudinal resolution is also
20  1° poleward of 30° (N or S) but increasing from than latitude to $\frac{1}{3}°$ at the equator. In the vertical there are 40 levels with thicknesses increasing monotonically from 10 m in the top 100 m to 345 m at the bottom, and with a full depth of 5500 m. A timestep of 1 hour is used. The computer code is based on that of Bryan (1969) and Cox (1984). The active ocean tracers (temperature and salinity) use a pseudo fourth-order advection scheme (Pacanowski and Griffies, 1998), while the passive tracers (including all the ocean biogeochemical tracers) use the UTOPIA scheme (Leonard et al., 1993) with a flux-
25  limiter. The Gent and McWilliams (1990) adiabatic mixing scheme is used in the skew flux form due to Griffies (1998), and with coefficient that varies spatially and temporally following Visbeck et al. (1997). An implicit linear free-surface scheme (Dukowicz and Smith, 1994) is included for freshwater fluxes. A simple upper mixed-layer scheme (Kraus and Turner, 1967) is used for vertical mixing due to surface fluxes of heat and freshwater for both active and passive tracers. The sea-ice model is based on the Los Alamos National Laboratory sea-ice model, CICE (Hunke and Lipscomb, 2004), including five thickness
30  categories, elastic-viscous-plastic ice dynamics (Hunke and Dukowicz, 1997) and ice ridging. The presence of sea-ice of any thickness reduces to zero the light entering the water-column (so preventing photosynthesis by marine phytoplankton) and blocks completely the transfer of gases between the atmosphere and ocean.

Coupling between the atmosphere and ocean models happens every 24 model hours. After 48 atmospheric timesteps (of 30 minutes each) have been run the fluxes of heat, freshwater, wind-stress and wind mixing energy, along with any necessary

biogeochemical quantities, are determined (usually as a time-mean over the 24 hours) and passed via the coupler to the ocean. Because the atmosphere and ocean models use different grids this involves re-gridding, with special care needing to be taken at the coasts where an atmospheric grid-box may correspond to both an ocean and a land grid-box. The ocean is then run for 24 timesteps (of 1 hour each) and the relevant fluxes calculated and passed to the atmosphere.

5    The biogeochemical quantities passed from the atmosphere to the ocean are the deposition flux of mineral dust and the concentration of $CO_2$ in the lowest atmospheric level, while the flux of $CO_2$ and the flux of Dimethyl Sulphide (DMS) are passed from ocean to atmosphere. Note however that in the concentration-driven simulations for which the results are presented here the atmospheric $CO_2$ concentration "seen" by the ocean is not passed from the atmosphere but prescribed in the ocean model (in such a way that it agrees with the atmospheric concentration prescribed in the atmosphere, once the different units are taken into account), and while the flux of $CO_2$ between the ocean and the atmosphere is calculated in the ocean model it is

10   purely diagnostic and is not passed to the atmosphere.

The dust deposition flux is calculated in the atmosphere as part of the dust sub-model, which is based on that described in Woodward (2001) but with developments as detailed in Woodward (2011). Six size-classes of mineral dust particles are used (up to 30 $\mu$m radius), and deposition can be by four mechanisms: wet deposition from convective precipitation and from

15   large-scale precipitation and dry deposition (i.e. settling under the force of gravity) from the lowest level and from levels above. For each size-class, the flux of dust being deposited is summed over the four mechanisms and separately passed to the ocean. Although not used in the simulations presented here, this separate passing allows for different size dust particles to have different soluble iron contents (supply of iron is the sole reason the dust deposition flux is passed to the ocean).

### 3.1 Simulations

20   The HadGEM2-ES model was used to run a wide range of simulations for CMIP5, the 5th Climate Model Intercomparison Project (Taylor et al., 2012); Jones et al. (2011) gives a detailed overview of the HadGEM2-ES simulations. The results presented here relate to a sub-set of three simulations, all with prescribed atmospheric $CO_2$ concentration. The first is the pre-industrial control ("piControl" in the CMIP5 terminology), the historical simulation ("historical"; from December 1859 to December 2005) and the RCP8.5 future simulation ("rcp85"). The historical simulation branched from the piControl, and

25   rcp85 was a continuation of the historical to simulated year 2100.

The model was spun-up before the piControl commenced. The ocean has particular issues with spin-up, because ideally several cycles of the ocean overturning circulation are needed to bring the tracers into equilibrium with the circulation and the driving climatological fluxes from the atmosphere, and each cycle lasts 500-1,000 model years. It was therefore deemed impractical to spin the full coupled model for the required time, and in any case the atmosphere and land-surface models would

30   reach equilibrium much faster.

The World Ocean Atlas (hereafter WOA) provides comprehensive gridded fields for the active tracers, temperature and salinity, and the processes affecting these quantities at the surface are relatively well understood and parameterised, so it was possible to initialise the ocean with fields close to equilibrium. The biogeochemical tracer fields however were not so easy to initialise. WOA gridded fields are available for the nutrients nitrate and silicate and for oxygen, but they are based on

many fewer data than those for temperature and salinity. Gridded fields are available for dissolved inorganic carbon (DIC) and total alkalinity (TAlk) from GLODAP (Sabine et al., 2005; Key et al., 2004) but these are based on even fewer data and relate to the present day with a substantial storage of anthropogenic carbon rather than the pre-industrial distribution (a correction for anthropogenic storage is available, but the method used for its production introduces many more uncertainties).

5   At the time that the model spin-ups were started the 2009 edition of the WOA database was the most recent, so those fields were used. In addition, while the Diat-HadOCC model was developed to represent the main ocean biogeochemical processes which (along with the physical circulation) determine the horizontal and vertical distributions of these tracers the incomplete knowledge of these processes, particularly quantitatively, and the model's necessary simplicity mean that the simulated fields may be significantly different from those measured in the real ocean (even with an accurate circulation). Therefore the ocean

10  biogeochemical tracers, even if initialised from the best-available gridded fields, required a significant period of spin-up before the drifts became acceptably small. The main criterion for "acceptably small" was a net pre-industrial air-sea flux of $CO_2$ that was below 0.2 Pg C / year (averaged over a decade, so inter-annual variability was smoothed out).

The tracers were therefore initialised as follows:

– Temperature and salinity: WOA 2009: Locarnini et al. (2010), Antonov et al. (2010)

15  – Nitrate, silicate (i.e. silicic acid), oxygen: WOA 2009: Garcia et al. (2010b), Garcia et al. (2010a)

– Iron: an initial field was produced from measurements reported in Parekh et al. (2004), on which the iron model used in Diat-HadOCC was based.

– misc-Phytoplankton, diatoms, zooplankton, and also C-, N-, and Si-detritus: a nominal small value ($10^{-6}$ mMol / m$^3$) was used, because these quantities (being mainly confined to the surface levels) would very quickly come into a pseudo-

20  equilibrium with the climatological fluxes and the initial nutrient distributions, and then be able to track the decadal and centennial changes to those distributions.

– DIC and TAlk: these were initialised from (re-gridded) fields from an earlier pre-industrial simulation by the HadCM3C model, where the net air-sea $CO_2$ flux had been within the criterion; it was expected that the large-scale ocean circulation would not differ greatly between the models.

25  The early stages of the spin-up were done incrementally: while parameterisations of the land-surface and the dust sub-models were being tested forty-year simulations were run for each trial sequentially, and around 200 years of spin-up were obtained this way. It was reasoned that the different versions of the land and dust models would not produce significantly different equilibria for the ocean tracers, and the ocean biogeochemical model, which was unchanged, would be a more-dominant influence. After this period, another 100 years of simulation was completed with the finalised model, and during this average fields (one for

30  each month of the year) were calculated for the climatological fluxes between the atmosphere and ocean. These average annual cycle fields were then used to force a coarse-resolution ocean-only model (a low-resolution version of the ocean component of HadCM3 - see Gordon et al., 2000 - with Diat-HadOCC embedded) which could be run extremely efficiently. This ran for

2,000 simulated years, after which the biogeochemical fields (but NOT temperature or salinity) were re-gridded back to the HadGEM2-ES ocean resolution and put back in that model (at the point immediately following the 100-year coupled spin-up. HadGEM2-ES was subsequently run in coupled mode for a further 50 years, during which it was found that the main criterion of the net air-sea $CO_2$ flux being below 0.2 Pg C / year was comfortably satisfied, and the drifts in the other biogeochemical

5  fields were reduced compared to before the ocean-only phase. However, there were still significant drifts in the silicate and dissolved iron fields.

The pre-industrial control (piControl) simulation was started from the end of the coupled spin-up, with its date set to 1st December 1859. (Note that HadGEM2-ES, like previous Met Office climate models, uses a 360-day year of 12 months each of 30 days, and begins its simulations on the 1st December, the start of meteorological winter, rather than 1st January.) It ran

10  to the year 2100 and beyond. The atmospheric $CO_2$ concentration was prescribed at a constant value, and the concentration (strictly, the partial pressure) seen by the ocean was also held at the same constant value. The historical simulation began from the same date, using the same initial fields. It ran to the end (31st December) of 2005. The atmospheric $CO_2$ concentrations were prescribed according to the CMIP5 dataset (http://cmip-pcmdi.llnl.gov/cmip5/forcing.html). The future simulation, rcp85, began at 1st December 2005 and was initialised using the fields from the historical simulation that were valid for that time.

15  Again, the atmospheric $CO_2$ was prescribed, but this time according to a future scenario (also to be found in the CMIP5 dataset). This was one of 4 RCPs (Representative Concentration Pathways; see Moss et al., 2010) calculated using an Integrated Assessment Model using projections of future anthropogenic emissions and other changes. RCP8.5 is the scenario with the highest atmospheric $CO_2$ concentrations, and the radiative forcing at year 2100 due to additional $CO_2$ is 8.5 W / m$^2$. Changes in the Earth System due to climate change will in general show most clearly in this scenario, and so, although HadGEM2-ES

20  ran all four RCP simulations (Jones et al. 2011; which also gives more details of other climatically-active gases, etc. in these experiments) it is the results from RCP8.5 that are considered in the following section.

## 4   Results from the Diat-HadOCC model

The primary purpose of the Diat-HadOCC model is to represent the marine carbon cycle, along with the factors and feedbacks influencing and controlling it, in the past, in the present and in the future; and therefore initially the results described here relate

25  to those quantities most directly connected with that cycle. However, it is also important to know that where the model results closely agree with observations they do so for the right reasons, rather than by coincidence, so certain other quantities are also presented.

### 4.1   Results for the present day (2010s)

#### 4.1.1   Total Chlorophyll

30  Figure 2 shows the annual mean surface total chlorophyll predicted by the model for the (simulated) decade 2010-2019 in the upper panel and that derived from satellite retrievals in the lower panel. The satellite-derived data are from the GlobColour

surface chlorophyll product (Fanton d'Andon et al., 2010; Maritorena et al., 2010) for the years 1998-2007, with further processing as described in Ford et al. (2012) to produce a monthly climatology, which has then been averaged to give the annual mean. Two things are immediately apparent: the geographical distributions are very similar but the actual values in the model are noticeably more extreme: higher where the data are high (Southern Ocean, sub-polar gyres in the North Pacific

5   and North Atlantic, eastern Equatorial Pacific) and lower where the data are low (mainly the sub-tropical gyres). In fact in the centres of the sub-tropical gyres the model chlorophyll is very slightly negative. Comparing the area-means of the respective annual mean fields, the model has an average of 0.812 mg Chl m$^{-3}$ while the average of the data is 0.213 mg Chl m$^{-3}$. However the seasonal cycle is also important, and Figure 3 shows (top panel) the seasonal cycle of the zonally-meaned model chlorophyll; (middle panel) the same but scaled by the factor 0.213/0.812 (so that the global annual mean is the same as that

10   of the data); and (bottom panel) the seasonal cycle of the zonally-meaned data. It can be seen by comparing the middle and bottom panels that the excess Chlorophyll is accentuated by a greater-than-average factor when the observed chlorophyll is high. It is possible to find the best-fitting sine-curve through the monthly mean values at any points (assuming they form a repeating cycle): Figure 4 shows the amplitude (left panels) and phase (right panels) of the seasonal cycle so derived of the model chlorophyll (upper panels, amplitude adjusted by factor 0.213/0.812 so that patterns can be better compared) and the

15   satellite-derived data (lower panels). In the model, the seasonal cycle is larger (even when adjusted) in much of the Southern Ocean and in the Equatorial Pacific, and slightly lower in the sub-polar North Atlantic.

### 4.1.2   Diatoms and Misc-Phytoplankton

Figure 5 shows the surface biomass of the two phytoplankton types, diatoms and misc-Phyto: the mean for the model years 2010-2019. The geographical patterns are naturally very similar to that of the model's total surface chlorophyll, since the

20   CMIP5 simulations used a fixed carbon:chlorophyll ratio for each of the phytoplankton (and the same value, 40.0 mg C / mg Chl, for each type). The geographical patterns for each type are also very similar to each other, with the diatoms having a slightly greater value than the misc-Phyto (global averages 1.486 and 1.223 mMol C m$^{-3}$ respectively, so diatoms make up 55% of the total surface biomass). The diatoms are slightly more dominant than the global average in the North Atlantic Ocean and in the Southern Ocean, both areas where surface silicic acid (needed by diatoms for shell formation) is plentiful.

25   Figure 6 compares the amplitude and the phase of the seasonal cycles for the two surface biomass types; as in the case of the total chlorophyll, these have been obtained by fitting a sine-curve to the monthly mean values at each point. The amplitude of the cycle is in each case very similar to the mean biomass, except in the equatorial latitudes (and especially in the Equatorial Pacific) where the amplitude is significantly less; this implies that in those latitudes there is significant biomass all year round, whereas in the high latitudes where the cycle amplitude and the mean are similar the biomass drops to near-zero for at least

30   some of the year. The right-hand panels show the phases of the seasonal cycle of surface biomass, in terms of the time of year when the biomass is at a maximum. The phases have comparable patterns, though it is noticeable that the peak of the diatom cycle leads that of the misc-Phyto by between 1 and 2 months at high latitudes, and especially in the North Atlantic and the Southern Ocean. This is consistent with observed seasonal succession of phytoplankton types. Figure 7 shows Hov-Muller diagrams of the seasonal abundances of the two phytoplankton types: the left-hand panels show global zonal means and the

right-hand panels zonal means in the Atlantic basin only. The earlier growth of the high-latitude diatoms is clearly apparent globally and especially in the Atlantic, where the magnitude of the diatom spring bloom is also seen to be higher than that of the misc-Phyto.

### 4.1.3    Primary Production

The global mean, vertically-integrated, total primary production during the years 2010-2019 in the model is 35.175 Pg C / yr; of this 19.791 Pg C / yr (56.3%) is due to the diatoms and 15.384 PgC / yr is due to the misc-Phyto. The total is slightly below the generally-quoted range of global primary production, 40-60 Pg C / yr (e.g. Carr et al. 2006). However that total includes the high-production areas along the coasts and in shelf-seas, which the coarse physical resolution and the structure of the model do not allow to be realistically represented: there are no sediments, no tidal mixing, no riverine supply of nutrients or run-off from land and the circulation over the shelf (where that exists) is not accurate. Figure 8 shows the geographical pattern of the total primary production and that of each phytoplankton type. Since the biomass and chlorophyll distributions of the two types are so similar it is no surprise that the primary production patterns are similar also; to each other and to the chlorophyll and biomass patterns. The diatoms dominate production slightly in most areas, and particularly in the North Atlantic Ocean and the Southern Ocean; in addition the un-productive gyres are larger in extent for misc-Phyto than for diatoms. Figure 9 shows Hov-Muller plots of the seasonal cycle of the total primary production (top row) and the separate diatom (middle row) and misc-Phyto (bottom row) fractions; global zonal means (left column) and zonal means for the Atlantic basin only (right column) are presented. The two phytoplankton types follow a generally similar pattern through the year, with the highest production occurring for each at temperate latitudes during the spring and summer in each hemisphere. However it is noticeable that the diatom production increases before that of the misc-Phyto: this is due to the diatoms having a higher specific growth rate (when all nutrients are non-limiting) and being more resistant to grazing because of their opaline shells (this is expressed in the model in terms of the zooplankton's base feeding preferences). This advanced blooming by the diatoms is evident in both the boreal and austral spring, and is especially pronounced in the North Atlantic ocean.

### 4.1.4    pCO$_2$

Figure 10 compares the model surface ocean pCO$_2$ field, meaned over the period 1990 to 2009 (upper panel), with the Takahashi gridded annual mean surface pCO2 field referenced to the year 2000 (lower panel). Overall the fields look very similar, having global means that show a consistent rise from preindustrial mean (to 364.2 ppmv in the model, compared to 357.9 ppmv in the gridded data product; in the year 2000 the atmospheric partial pressure was specified to be 368.8 ppmv). However, closer examination reveals a number of differences. The data show a narrow ridge of high pCO$_2$ in the Eastern Equatorial Pacific, but the corresponding high-pCO$_2$ water in the model is more widespread, does not reach the same extremes as the data, and actually shows a local minimum where the data-product values are highest. This is due to the much higher chlorophyll (and therefore also higher primary production) in that area dragging down the surface DIC. In the Atlantic basin there is a significantly greater area with very high pCO$_2$ than in the gridded field, especially in the northern and southern sub-tropical gyres. Finally there is

a zonal band of high $pCO_2$ water in the model just south of 45° S which is not present in the data; this is also an area where the model over-estimates the primary production.

Figure 11 compares the amplitude (left-hand panels) and the phase (right-hand panels) of the seasonal cycle in the model (mean of years 1990 to 2009; upper panels) and the data-product (referenced to year 2000; lower panels). It can be seen that

5  the model produces a substantially greater seasonal cycle than is observed in the data, though some of the patterns are similar: the data-product shows a relatively large amplitude of the cycle in the northern sub-tropical and sub-polar Pacific, where the model does as well, and in the areas closest to the Antarctic continent. However the strong seasonal cycle seen in the model in the North Atlantic is largely absent from the data, as is the band covering the southern sub-tropical gyres in all three ocean basins. In contrast to the large differences in the amplitude of the seasonal cycle, the phase compares quite well (though the

10  model has less variability in the Southern Ocean).

### 4.1.5  Air-Sea $CO_2$ flux

Figure 12 shows the air-to-sea flux of $CO_2$ (i.e. positive for net flux into the ocean) meaned over the decade 2010 to 2019. The upper panel shows the total flux (i.e. the natural cycle of $CO_2$ and the anthropogenic perturbation combined), while the lower panel shows just the anthropogenic perturbation. This perturbation has been calculated by subtracting the mean of the

15  air-to-sea flux in the piControl run from the total flux at each point. The annual mean $CO_2$ flux in the piControl simulation averaged just $0.0237$ Pg C yr$^{-1}$ over the period 1860 to 2099, with a standard deviation of $0.1036$ Pg C yr$^{-1}$ and no significant trend; this average is clearly well within the $0.2$ Pg C yr$^{-1}$ criterion for a successful spin-up. The annual mean $CO_2$ flux in the RCP8.5 simulation was $2.529$ Pg C yr$^{-1}$ averaged over the years 2010 to 2019, and was $2.117$ and $1.960$ Pg C yr$^{-1}$ in the 2000s and 1990s respectively. These figures are in good agreement with the figures quoted by the IPCC 5th Assessment Report

20  (IPCC, 2013) of $2.3 \pm 0.7$ and $2.2 \pm 0.7$ Pg C yr$^{-1}$ for the 2000s and 1990s respectively. Given the method for calculating the anthropogenic perturbation to the flux there is no way to distinguish between the two separate components to it: namely the (i) ingassing of anthropogenically-emitted $CO_2$ (mainly fossil fuel combustion) and (ii) changes to the natural cycle caused by climate change (itself mainly due to increasing atmospheric $CO_2$). Whereas the first component would be expected to give a net flux into the ocean the second can be either into or out of the ocean, and careful examination of the lower panel reveals a few

25  areas in the sub-tropical Pacific where the perturbation flux is negative (out of the ocean). But predominantly the perturbation flux is into the ocean, and co-incident with some of the largest fluxes in the total flux (and also the natural cycle flux): the sub-polar North Atlantic and the adjacent sector of the Arctic, the area where the Kuroshio current becomes zonal and the seas surrounding the Antarctic continent. It is notable that although (on a per unit area basis) the northern sub-polar Atlantic dominates the total flux it is only comparable with the Southern Ocean in terms of the anthropogenic perturbation. Figure 13

30  shows Hov-Muller plots of the seasonal cycle of the total flux of $CO_2$, zonally meaned globally and separately for each of the three ocean basins: Atlantic, Indian and Pacific. The Atlantic has the largest per unit area fluxes, and these occur in winter and early spring months when low temperatures reduce the surface ocean $pCO_2$ and deep convective mixing carries ingassed $CO_2$ away from the atmosphere. However, that pattern is reversed in the Pacific north of 45°N and in the most southerly latitudes of all three basins, where the most intense uptake is in the local summer months. This is due to strong biological activity taking

DIC out of the water and lowering the $pCO_2$ despite the warmer summer temperatures acting to raise it. The model has only weak primary production in the North Atlantic so that effect is reduced there, whereas the winter subduction is particularly strong, and so winter uptake dominates in that region in this model. Figure 14 shows the seasonal cycle of the anthropogenic perturbation flux in a similar way. Similar patterns are observed, but the North Atlantic is less dominant in winter.

### 4.1.6 DIC

Figure 15 compares the model's surface DIC (means over the years 2010-2019, in the upper panel, and 1990-1999, in the middle panel) with that from the GLODAP gridded field (lower panel; http://cdiac.ornl.gov/oceans/glodap/). The data from the GLODAP project have been re-gridded to the HadGEM2-ES ocean grid, and converted from Mol C $kg^{-1}$ to mMol C $m^{-3}$ using a mean surface water density of 1025 kg $m^{-3}$. The global mean surface values are 2068 mMol C $m^{-3}$ for the model in the years 2010-2019 (and 2054 mMol C $m^{-3}$ averaged over the years 1990-1999), while the data (referenced to the year 2000) have a global average of 2066 mMol C $m^{-3}$. Both these quantities, of course, include anthropogenic $CO_2$ present in the surface waters. Because the GLODAP field only extends to 70°N the model mean does not include values poleward of that latitude either. The geographical pattern can be seen to be very similar, with the only area showing significant disagreement being the Atlantic Ocean basin, and in particular the northern-hemisphere sub-tropical and sub-polar gyres therein, where the surface concentration in the model is significantly higher. There has been a substantial increase in the model's surface concentration in that basin between the 1990s and the 2010s, and the agreement between model and data is noticeably better for the earlier date (which is closer to the data's reference date). Figure 16 shows the amplitude and the phase (time of year of the maximum) of the seasonal cycle of surface DIC. This is determined by a number of factors: vertical mixing, vertical transport, air-sea $CO_2$ flux and biological uptake and release. All of these factors vary seasonally and their relative contributions are different from place to place, and so the phase of the cycle (and how well a sine-curve represents it) varies more with location than many other cycles. In the sub-polar North Atlantic, for example, relatively high DIC water is mixed (by convective and by wind-induced mixing) from depth to the surface during the winter, and the low surface temperature keeps the ocean $pCO_2$ lower than the atmosphere, so there is ingassing of $CO_2$. As the season passes to spring the increased solar irradiance warms the surface water, vertical mixing is suppressed, and there is net uptake of DIC by the phytoplankton for growth. Those factors tend to cause a reduction in surface DIC concentration and so reduce the $pCO_2$, but at the same time the increased temperature will increase it (for a given DIC concentration); which is the dominant effect, and so whether the air-sea $CO_2$ flux moves towards greater ingassing or greater outgassing, depends on the local conditions. The phase varies by up to 6 months across the North Atlantic at a latitude of 50°, while at a similar latitude across the Pacific the phase is almost constant.

### 4.1.7 Nutrients: nitrate, silicate, iron

Figure 17 compares the model surface nitrate field (mean over the years 2010 to 2019) with the corresponding field from the World Ocean Atlas 2005 (hereafter WOA05; Conkwright et al. 2005). Strictly the model nitrate field represents the sum of all dissolved inorganic nitrogen compounds (nitrate, nitrite and ammonium) but in many circumstances the first of those is dominant. Nitrogen is the "currency" of the model ecosystem and the main limiting nutrient. The geographical distributions

compare well, with high concentrations in the Southern Ocean, the Eastern Equatorial Pacific, and the northern sub-polar regions of the Pacific and Atlantic Oceans. The gridded data from WOA05 is slightly higher than the model in the Eastern Equatorial Pacific and in the sub-polar North Atlantic; in the former region this is due to higher production in the model than is observed in the real ocean taking up more nitrate for phytoplankton growth, while in the latter the lower-than-observed

5    production is due to low nitrate concentrations at the start of the growing season, in turn due to a tendency of the model to lose nutrient from that region through the deep circulation. It can also be seen that in the model the nitrate concentration has slipped to be slightly negative in some sub-tropical regions, particularly the centres of the gyres; in such circumstances the ecosystem model (but not the advection or mixing processes of the physical model) treats the value as zero. Figure 18 compares the amplitude and phase of the seasonal cycle in the model and WOA05 nitrate fields. These have been determined

10   by finding the best-fitting sine-curve to the monthly means at each point; the phase refers to the time (fraction of year) when the concentration is highest. The seasonal cycle will be determined by a number of factors, including vertical advection and mixing and the uptake and remineralisation of nitrate by the ecosystem, all of which can vary through the year. The model amplitude field is similar in pattern and scale to the mean concentration as presented in Figure 17, but the WOA05 field shows some interesting differences from its concentration field: the scale of the seasonal cycle is much lower in the Southern Ocean

15   (0.5 to 5 mMol N m$^{-3}$ amplitude compared to greater than 20 mMol N m$^{-3}$ mean, while the model has an amplitude of 5 to 15 mMol N m$^{-3}$ with a similar mean). This suggests that the model is not fully limiting the phytoplankton growth in that region: this limitation will not be from low nitrate levels as they are always higher than needed for growth, but could be from other nutrients (probably dissolved iron; see Martin et al. 1992) or from light limitation. In terms of the phase of the cycle, the model shows much greater consistency than WOA05: almost all the areas poleward of 30° in the model show the highest

20   concentration at the end of local winter, but the data product shows much more variability in the Southern Hemisphere (both models show variability in the tropics). The high variability in the Southern Ocean in WOA05 may be related to the lower amplitude of the cycle making it hard to determine a best-fitting sine-curve unambiguously.

Figure 19 compares the model silicate field (i.e. dissolved silicic acid; meaned over the years 2010-2019) with the corresponding gridded field from WOA05. Unfortunately a problem in the implementation of the model in the CMIP5 simulations

25   has meant that the model silicate field has deviated substantially from the observations, with high surface values everywhere. This has the effect that, while it would normally be expected that silicate values will be low enough to limit the growth of diatoms (which require it to form their shells) in some areas all the time and in others at certain times of the seasonal cycle (after a bloom, for instance), in these model simulations silicate is never a limiting nutrient for diatoms, which are therefore only limited by nitrate, iron and light-availability. Despite that, Figure 20, which compares the amplitude and phase of the

30   seasonal cycle of surface silicate in the model and WOA05, shows that those non-silicate limitations are still able to produce a seasonal cycle of uptake in the model that looks reasonable, suggesting that the diatom production is well-represented (though not for all the right reasons).

Figure 21 presents the surface dissolved iron concentration in the model (upper panel) and the amplitude of the seasonal cycle (lower panel). In each case the period considered covers the years 2010 to 2019. Note that different scales are used for

35   the two plots. Given that the half-saturation concentration for iron limitation was set at 0.2 $\mu$ Mol Fe m$^{-3}$ it can be seen that

there are few areas of the ocean where the decadal mean concentration of dissolved iron limits the growth of either misc-Phyto or diatoms. However, there are significant areas, including the Southern Ocean, the Eastern Equatorial Pacific and the North Pacific, where iron is limiting at certain times of the seasonal cycle, though even this is different from the observed situation where, for instance, iron is limiting in the Southern Ocean at all times of the seasonal cycle. Analysis of the long-term behaviour

5 of the dissolved iron field in the piControl simulation shows a drift to higher concentrations at all depths including the surface levels, due to parameter values in the iron sub-model not being optimal and this field not being fully spun-up. There is still much uncertainty in the quantitative understanding of the processes affecting iron in the ocean, especially those relating to organic ligands, and the representation used here can surely be improved.

## 4.2 Response to climate change

10 This section presents key results of the response of the model to climate change in the RCP8.5 scenario simulation, in particular between the decade 2010-2019 ("the 2010s") and the decade 2090-2099 ("the 2090s"), and also through the historical simulation from which the future run is initialised.

Figure 22 shows the global zonal mean surface nitrate concentration through the historical and RCP8.5 scenario period (years 1860 to 2099), allowing trends to be identified. The corresponding period of the piControl simulation (not shown) has

15 no trend or drift, so the changes with time seen in this plot are all due to climate change. It can be seen that at almost all latitudes the concentration decreases through the 21st century, and that the rate of decrease becomes more marked towards the end of the simulation. This trend can be understood in terms of the vertical supply of nitrate being reduced as the surface ocean is warmed and becomes more stratified. Although phytoplankton growth (and nitrate uptake) is also reduced because of the reduced nutrient availability the net effect is a decrease in the surface nitrate concentration, and this drives many of the changes

20 seen in the model and presented in this section.

Figure 23 presents Hov-Muller plots of the total chlorophyll anomaly (a measure of the abundance of both types of phytoplankton) from 1860 to 2099 for the Atlantic basin (upper panel) and the Pacific basin (lower panel). The anomaly has been calculated by subtracting the chlorophyll in the piControl simulation (the mean from 1860 to 2099) from the annual mean chlorophyll in the historical+RCP8.5 simulation. The piControl chlorophyll showed no significant trend or drift. In addition

25 to inter-annual and inter-decadal variability in both basins it can be seen that trends become apparent in the climate change scenario, mainly after the year 2000. In both basins the chlorophyll close to the Antarctic continent increases substantially, as does that in the Atlantic Basin around 45°S. In contrast there is a clear reduction in chlorophyll at the Equator, present in both basins but particularly marked in the Pacific. Between 30 and 60°N there is a smaller reduction in chlorophyll in each basin, while in the Pacific just north of that band there is a marked increase. These trends can be understood as increased stratifica-

30 tion both reducing the vertical nutrient supply and reducing the depth of the mixed layer during the growing season (and so improving the available light for phytoplankton in the surface layer): in the tropics the former dominates so production (and chlorophyll) is reduced, but at high latitudes the latter is more important and leads to higher production. In addition, around Antarctica warming seas mean that ice-cover is reduced, allowing more primary production. Similar results have been reported previously in future scenario simulations (e.g. Bopp et al. 2003).

Figure 24 shows how the seasonal cycle of total chlorophyll changes from the 2010s to the 2090s in the Atlantic basin (upper panel) and the Pacific (lower panel). In both basins the reduction in chlorophyll at Equatorial latitudes is seen to be present throughout the year, though it is most intense in the Atlantic between July and November and in the Pacific during March and April. In the Southern Ocean sectors of each basin the change is an increase between October and February in
5   the most southerly latitudes, and no change in other months; however slightly further north, around 45°S, there is an increase during those austral summer months in the Atlantic but a decrease in the Pacific. In the northern hemisphere, poleward of 40°N, the Atlantic sees a reduction between April and September but the Pacific sees a strong increase in the Spring (March to May) followed by an equally-strong reduction in the summer (June to August). This "dipole" change in the North Pacific is a signature of the seasonal cycle shifting forward by several months, in response to changing physical conditions.

10   Figure 25 shows the difference, between the 2090s and the 2010s, in the mean total primary production (upper panel) and in the mean seasonal cycle of that quantity (lower panel). The mean field displays strong reductions in the Equatorial Pacific and Atlantic Oceans, because of reduced nitrate availability, and also in the sub-polar North Atlantic and the eastern sub-polar North Pacific. In contrast the Southern Ocean close to the Antarctic continent shows strong increases in production, for the reasons outlined above: shallower surface mixed layers allowing the phytoplankton to remain for longer in well-lit depths near
15   the surface, and reduced seasonal ice-cover allowing more time for growth. The seasonal cycle shows a pattern of changes that is very similar to the change in the mean, except in the Eastern Equatorial Pacific where the amplitude of the cycle is little changed but the mean has been substantially reduced; note that in the 2010s the seasonal cycle was also relatively small, while the mean was high in that area. Figure 26 shows the change through time of the diatom production and the misc-Phyto production (upper and lower panels respectively), and also separated into the Atlantic and Pacific basins (left- and right-hand
20   panels respectively). It is clear that similar trends are found for both phytoplankton types, though there are some differences between basins (e.g. the production by both types increases poleward of 60°N in the Pacific during the later 21st century, while similar latitudes in the Atlantic show a decrease). The global annual mean total primary production in the 2090s is 30.494 Pg C yr$^{-1}$ (compared to 35.175 Pg C yr$^{-1}$ in the 2010s, so a 13.3% reduction), which is apportioned 17.227 Pg C yr$^{-1}$ (c.f. 19.791; -13.0%) to the diatoms and 13.267 Pg C yr$^{-1}$ (c.f. 15.384; -13.7%) to the misc-Phyto; therefore there is only a very small shift
25   towards increased dominance by the diatoms.

Figure 27 shows how the surface ocean $pCO_2$ varies through the historical and RCP8.5 scenario. The top panel shows the change with time of the global zonal mean $pCO_2$ anomaly (i.e. the difference between the scenario and the piControl). As expected, the surface $pCO_2$ increases smoothly with time, increasing its rate in keeping with the prescribed atmospheric concentration. Most of the rise therefore occurs during the 21st century. It is notable that all latitudes increase at a substantially
30   similar rate. The middle panel shows the geographical distribution of the anomaly averaged over the period 2090-2099. Here the colour-scale has been set to show up what differences there are: the rise is greatest in the arctic and in the sub-tropical gyres, and in the northern sub-polar Atlantic. The bottom panel shows that the distribution of the anomaly of the seasonal cycle amplitude is very similar to that of the mean concentration, except around the Antarctic continent. The phase of the seasonal cycle in the 2090s (not shown) has changed little from that in the 2010s.

Finally, the air-to-sea flux of $CO_2$ is considered. Figure 28 shows the global total flux through the historical+RCP8.5 simulation from 1860 to 2099 (the piControl over that period showed no trend). It is clear that the flux increases with time; this is to be expected, since the atmospheric $pCO_2$ was increasing monotonically through the simulation. By the 2090s the net flux is 4.8 Pg C yr$^{-1}$.

5 Figure 29 shows the evolution of the zonal mean flux globally (top panel) and in the Atlantic and Pacific basins separately (middle and bottom panels respectively). It can be seen that, while the global total flux continued to increase throughout the period, there were certain latitudes in some basins where the flux peaked and then began to decline - despite the atmospheric $CO_2$ concentration continuing to increase. This effect is particularly noticeable in the Atlantic between 50 and 60 °N, with the peak uptake occurring between 1980 and 2030 before an accelerating decrease. Such a "peak and decline" feature is seen in

10 many CMIP5 model simulations as well as in other future simulations, and the causes are examined in Halloran et al. (2015). In the Southern Ocean, meanwhile, the uptake shows a monotonic and significant increase, particularly in the second half of the 21st century.

Figure 30 shows the seasonal cycle of the zonally-meaned total flux during the 2090s globally and in each ocean basin separately. It can be compared to Figure 13, which shows the same cycles during the 2010s. It is clear that there has been a

15 substantial shift towards net uptake, particularly where there was substantial uptake already in the 2010s; but there are some areas which were sources at the earlier time that became sinks for atmospheric $CO_2$ at the later time. There are also regions (e.g. the Atlantic around 45°N) which were weak sources in the summer months during the 2010s but which have become strong sources by the 2090s; and this is despite those latitudes being stronger sinks in the winter and spring months at the later time. Overall, therefore, the cycling of $CO_2$ between the ocean and atmosphere seems to have generally intensified.

20 ## 5    Conclusions

The Diat-HadOCC model is a development of the earlier HadOCC model, including separate diatom and misc-Phytoplankton components and representations of the dissolved silicate and iron cycles in the ocean and through the marine ecosystem. The model forms the ocean biogeochemistry component of the Met Office's coupled Earth System model HadGEM2-ES, and has been used to run a wide-ranging suite of simulations for the CMIP5 experiment. This paper has described the model in

25 detail and presented a selection of results from those simulations. The results shown (and many more) are freely available from the Earth System Grid website (https://pcmdi.llnl.gov/projects/esgf-llnl/). The model has been shown to be capable of reproducing many of the important features of the marine carbon cycle, including annual mean surface concentrations of dissolved inorganic carbon and total alkalinity and the seasonal cycle of ocean surface $pCO_2$. The climate change response of the model is also shown to be in accordance with similar modelling studies. In terms of the ecosystem, dissolved nutrient

30 concentrations (and their seasonal cycles) match available datasets well. Model chlorophyll tends to be more extreme than that inferred from satellite-derived ocean colour data: lower in the ocean's oligotrophic gyres but considerably higher in areas of high phytoplankton productivity and especially in the Equatorial Pacific. In contrast, the model's total primary productivity is around the lower bound of observational estimates. Diatoms make up 55% of the total phytoplankton biomass.

*Code availability.* Due to intellectual property right restrictions, the author cannot provide either the source code or documentation papers for the Unified Model (UM). The Met Office Unified Model is available for use under licence. A number of research organizations and national meteorological services use the UM in collaboration with the Met Office to undertake basic atmospheric process research, produce forecasts, develop the UM code and build and evaluate Earth system models. For further information on how to apply for a licence, see

5    http://www.metoffice.gov.uk/research/modelling-systems/unified-model.

Geoscientific
Model Development
Discussions

# References

Acton, F.S.: Numerical Methods that Work, Harper and Row, New York, 52, 1970

Anderson, T.R.: A spectrally averaged model of light penetration and photosynthesis, Limnol. Oceanogr., 38, 1403–1419, 1993

Antonov, J.I., Seidov, D., Boyer, T.P., Locarnini, R.A., Mishonov, A.V., Garcia, H.E., Baranova, O.K., Zweng, M.M., and Johnson, D.R.:

5     World Ocean Atlas 2009, Volume 2: Salinity. In Levitus, S. (Ed.) NOAA Atlas NESDIS 68, U.S. Gov. Printing Office, Wash., D.C., 2010

Bacastow, R.B.: Numerical evaluation of the evasion factor, in: Bolin, B. (ed.) Scope 16: Carbon cycle Modelling. John Wiley, New York, pp 95-101, 1981

Benson, B.B., and Krause, D. Jr: The concentration and isotopic fractionation of oxygen dissolved in freshwater and seawater in equilibrium with the atmosphere, Limnol. Oceanogr., 29, 620-632, 1984

10    Best, M.J., Pryor, M., Clark, D.B., Rooney, G.G., Essery, R.L.H., Menard, C.B., Edwards, J.M., Hendry, M.A., Porson, A., Gedney, N., Mercado, L.M., Sitch, S., Blyth, E., Boucher, O., Cox, P.M., Grimmond, C.S.B., and Harding, R.J.: The Joint UK Land Environment Simulator (JULES), model description - Part 1: Energy and water fluxes, Geosci. Model Dev., 4, 677–699, doi:10.5194/gmd-4-677-2011, 2011

Bryan, K.: A numerical method for the study of the circulation of the world ocean, J. Comput. Phys., 4, 347–376, 1969

15    Clark, D.B., Mercado, L.M., Sitch, S., Jones, C.D., Gedney, N., Best, M.J., Pryor, M., Rooney, G.G., Essery, R.L.H., Blyth, E., Boucher, O., Harding, R.J., Huntingford, C., and Cox, P.M.: The Joint UK Land Environment Simulator (JULES), model description - Part 2: Carbon fluxes and vegetation dynamics, Geosci. Model Dev., 4, 701–722, doi:10.5194/gmd-4-701-2011, 2011

Coleman, K., and Jenkinson, D.S.: RothC-26.3: a model for the turnover of carbon in soil, In: Powlson, D.S., Smith, P., Smith, J.U. (Eds.), Evaluation of soil organic matter models using existing, long-term datasets, NATO ASI Series I, Vol. 38. Springer-Verlag, Heidelberg, pp.

20    237–246, 1996

Coleman, K., and Jenkinson, D.S.: RothC-26.3, A model for the turnover of carbon in soil: Model description and User's guide, Lawes Agricultural Trust, Harpenden, UK, http://www.rothamsted.ac.uk/sustainable-soils-and-grassland-systems/rothamsted-carbon-model-rothc, 1999

Collins, W.J., Bellouin, N., Doutrieaux-Boucher, M., Gedney, N., Halloran, P., Hinton, T., Hughes, J., Jones, C.D., Joshi, M., Liddicoat, S.,

25    Martin, G., O'Connor, F., Rae, J., Senior, C., Sitch, S., Totterdell, I., Wiltshire, A., and Woodward, S.: Development and evaluation of an Earth-System model - HadGEM2, Geosci. Model Dev., 4, 1051–1075, doi:10.5194/gmd-4-1051-2011, 2011

Cox, M.D.: A primitive equation, three dimensional model of the ocean, Ocean Group Tech. Rep. 1, GFDL, Princeton, NJ, USA, 143 pp, 1984

Cox, P.M.: Description of the TRIFFID Dynamic Global Vegetation Model, Hadley Centre Technical Note HCTN 24,

30    Met Office, FitzRoy Road, Exeter EX1 3PB, UK, www.metoffice.gov.uk/media/pdf/9/h/HCTN_24.pdf, 2001 [Available from https://digital.nmla.metoffice.gov.uk/]

Cox, P.M., Betts, R.A., Jones, C.D., Spall, S.A., and Totterdell, I.J.: Acceleration of global warming due to carbon-cycle feedbacks in a coupled climate model, Nature, 408, 184–188, 2000

Dickson, A.G.: Thermodynamics of the dissociation of boric acid in synthetic seawater from 273.15 to 298.15 K, Deep-Sea Res., 37, 755-766,

35    1990

Dukowicz, J.K., and Smith, R.D.: Implicit free surface method for the Bryan-Cox-Semtner ocean model, J. Geophys. Res., 99, 7991–8014, 1994

Geoscientific
Model Development
Discussions

Eppley, R.W.: Temperature and phytoplankton growth in the sea, Fishery Bull., 70, 1063–1085, 1972

Essery, R.L.H., Best, M.J., Betts, R.A., Cox, P.M., and Taylor, C.M.: Explicit representation of sub-grid heterogeneity in a GCM land-surface scheme, J. Hydrometeorol., 4, 530–543, 2003

Fanton d'Andon, O.H., Antoine, D., Mangin, A., Maritorena, S., Durand, D., Pradhan, Y., Lavender, S., Morel, A., Demaria, J., and Barrot,
5    G.: Ocean colour sensors characterisation and expected error estimates of ocean colour merged products from GlobColour, Ocean Optics XIX, Barga, Italy, 6-10 October 2008, pp. 51, 2008

Fasham, M.J.R., Ducklow, H.W., and McKelvie, S.M.: A nitrogen-based model of plankton dynamics in the oceanic mixed layer, J. Mar. Res., 48, 591–639, 1990

Ford, D.A., Edwards, K.P., Lea, D., Barciela, R.M., Martin, M.J., and Demaria, J.: Assimilating GlobColour ocean colour data into a pre-
10    operational physical-biogeochemical model, Ocean Science, 8(5), 751-771, 2012

Garcia, H.E., and Gordon, L.I.: Oxygen solubility in seawater: Better fitting equations, Limnol. Oceanogr., 37, 1307-1312, 1992

Garcia, H.E., Locarnini, R.A., Boyer, T.P., Antonov, J.I., Baranova, O.K., Zweng, M.M., and Johnson, D.R.: World Ocean Atlas 2009. Volume 3: Dissolved Oxygen, Apparent Oxygen Utilization, and Oxygen Saturation. In Levitus, S. (Ed.) NOAA Atlas NESDIS 69, U.S. Gov. Printing Office, Washington, D.C., 2010a

15    Garcia, H.E., Locarnini, R.A., Boyer, T.P., Antonov, J.I., Baranova, O.K., Zweng, M.M., and Johnson, D.R.: World Ocean Atlas 2009. Volume 3: Dissolved Oxygen, Apparent Oxygen Utilization, and Oxygen Saturation. In Levitus, S. (Ed.) NOAA Atlas NESDIS 69, U.S. Gov. Printing Office, Washington, D.C., 2010b

Geider, R.J., MacIntyre, H.L., and Kana, T.M.: Dynamic model of phytoplankton growth and acclimation: responses of the balanced growth rate and the chlorophyll a:carbon ratio to light, nutrient limitation and temperature, Mar. Ecol. Prog. Ser., 148, 187–200, 1997

20    Gent, P.R., and McWilliams, J.C.: Isopycnal mixing in ocean circulation models, J. Phys. Oceanogr., 20, 150–155, 1990

Gordon, C., Cooper, C., Senior, C.A., Banks, H., Gregory, J.M., Johns, T.C., Mitchell, J.F.B., and Wood, R.A.: The simulation of SST, sea ice extents and ocean heat transports in a version of the Hadley Centre coupled model without flux adjustments. Clim. Dyn., 16, 147-168, 2000

Griffies, S.M.: The Gent-McWilliams skew flux, J. Phys. Oceanogr., 28, 831–841, 1998

25    The HadGEM2 Development Team: Martin, G.M., Bellouin, N., Collins, W.J., Culverwell, I.D., Halloran, P.R., Hardiman, S.C., Hinton, T.J., Jones, C.D., McDonald, R.E., McLaren, A.J., O'Connor, F.M., Roberts, M.J., Rodriguez, J.M., Woodward, S., Best, M.J., Brooks, M.E., Brown, A.R., Butchart, N., Dearden, C., Derbyshire, S.H., Dharssi, I., Doutriaux-Boucher, M., Edwards, J.M., Falloon, P.D., Gedney, N., Gray, L.J., Hewitt, H.T., Hobson, M., Huddleston, M.R., Hughes, J., Ineson, S., Ingram, W.J., James, P.M., Johns, T.C., Johnson, C.E., Jones, A., Jones, C.P., Joshi, M.M., Keen, A.B., Liddicoat, S., Lock, A.P., Maidens, A.V., Manners, J.C., Milton, S.F., Rae, J.G.L., Ridley,
30    J.K., Sellar, A., Senior, C.A., Totterdell, I.J., Verhoef, A., Vidale, P.L., and Wiltshire, A.: The HadGEM2 family of Met Office Unified Model climate configurations, Geosci. Model Dev., 4, 723–757, doi:10.5194/gmd-4-723-2011, 2011

Halloran, P.R., Booth, B.B.B., Jones, C.D., Lambert, F.H., McNeall, D.J., Totterdell, I.J., and Völker, C.: The mechanisms of North Atlantic $CO_2$ uptake in a large Earth System Model ensemble. Biogeosci., 12, 4497-4508, 2015

Hunke, E.C., and Dukowicz, J.K.: An elastic-viscous-plastic model for sea ice dynamics, J. Phys. Oceanogr., 27, 1849–1867, 1997

35    Hunke, E.C., and Lipscomb, W.H.: CICE: The Los Alamos Sea Ice Model, documentation and software, Version 3.1, LA-CC-98-16, Los Alamos National Laboratory, Los Alamos, NM, 56pp, 2004

IPCC: Climate Change 2013: The Physical Science Basis. Contribution of Working Group I to the Fifth Assessment Report of the Intergovern-
    mental Panel on Climate Change [Stocker, T.F., Qin, D., Plattner, G.-K., Tignor, M., Allen, S.K., Boschung, J., Nauels, A., Xia, Y., Bex
    V., and Midgley, P.M. (eds.)]. Cambridge University Press, Cambridge, United Kingdom and New York, NY, USA, 1535 pp, 2013

Johns, T.C., Durman, C.F., Banks, H.T., Roberts, M.J., McLaren, A.J., Ridley, J.K., Senior, C.A., Williams, K.D., Jones, A., Rickard, G.J.,
5   Cusack, S., Ingram, W.J., Crucifix, M., Sexton, D.M.H., Joshi, M.M., Dong, B.-W., Spencer, H., Hill, R.S.R., Gregory, J.M., Keen, A.B.,
    Pardaens, A.K., Lowe, J.A., Bodas-Salcedo, A., Stark, S., and Searl, Y.: The new Hadley Centre climate model HadGEM1: Evaluation of
    coupled simulations, J. Climate, 19(7), 1327–1353, 2006

Jones, C.D., Hughes, J.K., Bellouin, N., Hardiman, S.C., Jones, G.S., Knight, J., Liddicoat, S., O'Connor, F.M., Andres, R.J., Bell, C., Boo,
    K.-O., Bozzo, A., Butchart, N., Cadule, P., Corbin, K.D., Doutriaux-Boucher, M., Friedlingstein, P., Gornall, J., Gray, L., Halloran, P.R.,
10   Hurtt, G., Ingram, W.J., Lamarque, J.-F., Law, R.M., Meinshausen, M., Osprey, S., Palin, E.J., Parsons Chini, L., Raddatz, T., Sanderson,
    M.G., Sellar, A.A., Schurer, A., Valdes, P., Wood, N., Woodward, S., Yoshioka, M., and Zerroukat, M.: The HadGEM2-ES implementation
    of CMIP5 centennial simulations, Geosci. Model Dev., 4, 543–570, doi:10.5194/gmd-4-543-2011, 2011

Keeling, R.F., Stephens, B.B., Najjar, R.G., Doney, S.C., Archer D., and Heimann, M.: Seasonal variations in the atmospheric O2/N2 ratio
    in relation to the kinetics of air-sea gas exchange, Global Biogeochem. Cycles, 12, 141-163, doi:10.1029/97GB02339, 1998

15  Key, R.M., Kozyr, A., Sabine, C.L., Lee, K., Wanninkhof, R., Bullister, J., Feely, R.A., Millero, F., Mordy, C., and Peng, T.-H.: A global
    ocean carbon climatology: Results from GLODAP. Global Biogeochemical Cycles, Vol. 18, GB4031, 2004

Kraus, E.B., and Turner, J.S.: A one dimensional model of the seasonal thermocline II. The general theory and its consequences, Tellus, 19,
    98–105, 1967

Leonard, B.P., MacVean, M.K., and Lock, A.P.: Positivity-Preserving Numerical Schemes for Multidimensional Advection, NASA Technical
20   memorandum 106055, 64pp., 1993 [Available from http://ntrs.nasa.gov]

Locarnini, R.A., Mishonov, A.V., Antonov, J.I., Boyer, T.P., Garcia, H.E., Baranova, O.K., Zweng, M.M., and Johnson, D.R.: World Ocean
    Atlas 2009, Volume 1: Temperature. In Levitus, S. (Ed.) NOAA Atlas NESDIS 67, U.S. Gov. Printing Office, Washington, D.C., 2010

Maritorena, S., Fanton d'Andon, O.H., Mangin, A., and Siegel, D.A.: Merged satellite ocean color data products using a bio-optical model:
    Characteristics, benefits and issues, Remote Sens. Environ., 114, 1791-1804, 2010

25  Martin, J.H., Knauer, G.A., Karl, D.M., and Broenkow, W.W.: VERTEX: carbon cycling in the northeast Pacific, Deep-Sea Res., 34, 267–285,
    1987

Millero, F.J.: Thermodynamics of the carbon dioxide system in the ocean, Geochim. Cosmochim. Acta, 59, 661-677, 1995

Morel, A.: Optical modelling of the upper ocean in relation to its biogenous matter content (case 1 waters), J. Geophys. Res, 93, 10,749–
    10,768, 1988

30  Morel, A.: Light and marine photosynthesis: A spectral model with geochemical and climatological implications, Prog. Oceanogr., 26,
    263–306, 1991

Moss, R.H., Edmonds, J.A., Hibbard, K.A., Manning, M.R., Rose, S.K., van Vuuren, D.P., Carter, T.R., Emori, S., Kainuma, M., Kram, T.,
    Meehl, G.A., Mitchell, J.F.B., Nakicenovic, N., Riahi, K., Smith, S.J., Stouffer, R.J., Thomson, A.M., Weyant, J.P., and Wilbanks, T.J.:
    The next generation of scenarios for climate change research and assessment, Nature, 463, 747-756, doi:10.1038/nature08823, 2010

35  O'Connor, F.M., Johnson, C.E., Morgenstern, O., Abraham, N.L., Braesicke, P., Dalvi, M., Folberth, G.A., Sanderson, M.G., Telford, P.J.,
    Voulgarakis, A., Young, P.J., Zeng, G., Collins, W.J., and Pyle, J.A.: Evaluation of the new UKCA climate-composition model - Part 2:
    The Troposphere, Geosci. Model Dev., 7, 41–91, doi:10.5194/gmd-7-41-2014, 2014

Oki, T., and Sud, Y.C.: Design of total runoff integrating pathways (TRIP)- a global river channel network, Earth Interactions 2: 1–37, 1998

Pacanowski, R.C., and Griffies, S.M.: MOM 3.0 manual, NOAA/Geophysical Fluid Dynamics Laboratory, Princeton, NJ, 692pp., 1998 [Available from NOAA/Geophysical Fluid Dynamics Laboratory, Princeton, NJ 08542.]

Palmer, J.R., and Totterdell, I.J.: Production and export in a global ocean ecosystem model, Deep-Sea Res. I, 48, 1169–1198, 2001

Parekh, P., Follows, M.J., and Boyle, E.: Modeling the global ocean iron cycle, Global Biogeochem. Cycles, 18, GB1002, doi:10.1029/2003GB002061, 2004

Platt, T., Sathyendranath, S., and Ravindran, P.: Primary production by phytoplankton: Analytic solutions for daily rates per unit area of water surface, Proc. R. Soc. London, Ser. B, 241, 101–111, 1990

Roy, R.N., Roy, L.N., Vogel, K.M., Moore, C.P., Pearson, T., Good, C.E., Millero, F.J., and Cambell, D.J.: Determination of the ionization constants of carbonic acid in seawater in salinities 5 to 45 and temperatures 0 to 45 °C, Mar. Chem., 44, 249-267, 1993

Sabine, C. L., Key, R.M., Kozyr, A., Feely, R.A., Wanninkhof, R., Millero, F.J., Peng, T.-H., Bullister, J.L., and Lee, K.: Global Ocean Data Analysis Project: Results and Data. ORNL/CDIAC-145, NDP-083. Carbon Dioxide Information Analysis Center, Oak Ridge National Laboratory, U.S. Department of Energy, Oak Ridge, Tennessee, 110 pp., 2005

Taylor, K.E., Stouffer, R.J., and Meehl, G.A.: An overview of CMIP5 and the experiment design, Bull. Amer. Meteor. Soc., 93, 485–498, doi:10.1175/BAMS-D-11-00094.1, 2012

Visbeck, M., Marshall, J., Haine T., and M. Spall, M.: Specification of eddy transfer coefficients in coarse-resolution ocean circulation models, J. Phys. Oceanogr., 27, 381–402, 1997

Wanninkhof, R.: Relationship between wind speed and gas exchange over the ocean, J. Geophys. Res., 97C, 7373-7382, 1992

Weiss, R.F.: Carbon dioxide in water and seawater: the solubility of a non-ideal gas, Mar. Chem., 2, 203-215

Woodward, S.: Modelling the atmospheric life cycle and radiative impact of mineral dust in the Hadley Centre climate model, J. Geophys. Res., 106, D16, 18155–18166, 2001

Woodward, S.: Mineral dust in HadGEM2, Hadley Centre Technical Note HCTN 87, Met Office, FitzRoy Road, Exeter EX1 3PB, UK, 2011 [Available from https://digital.nmla.metoffice.gov.uk/]
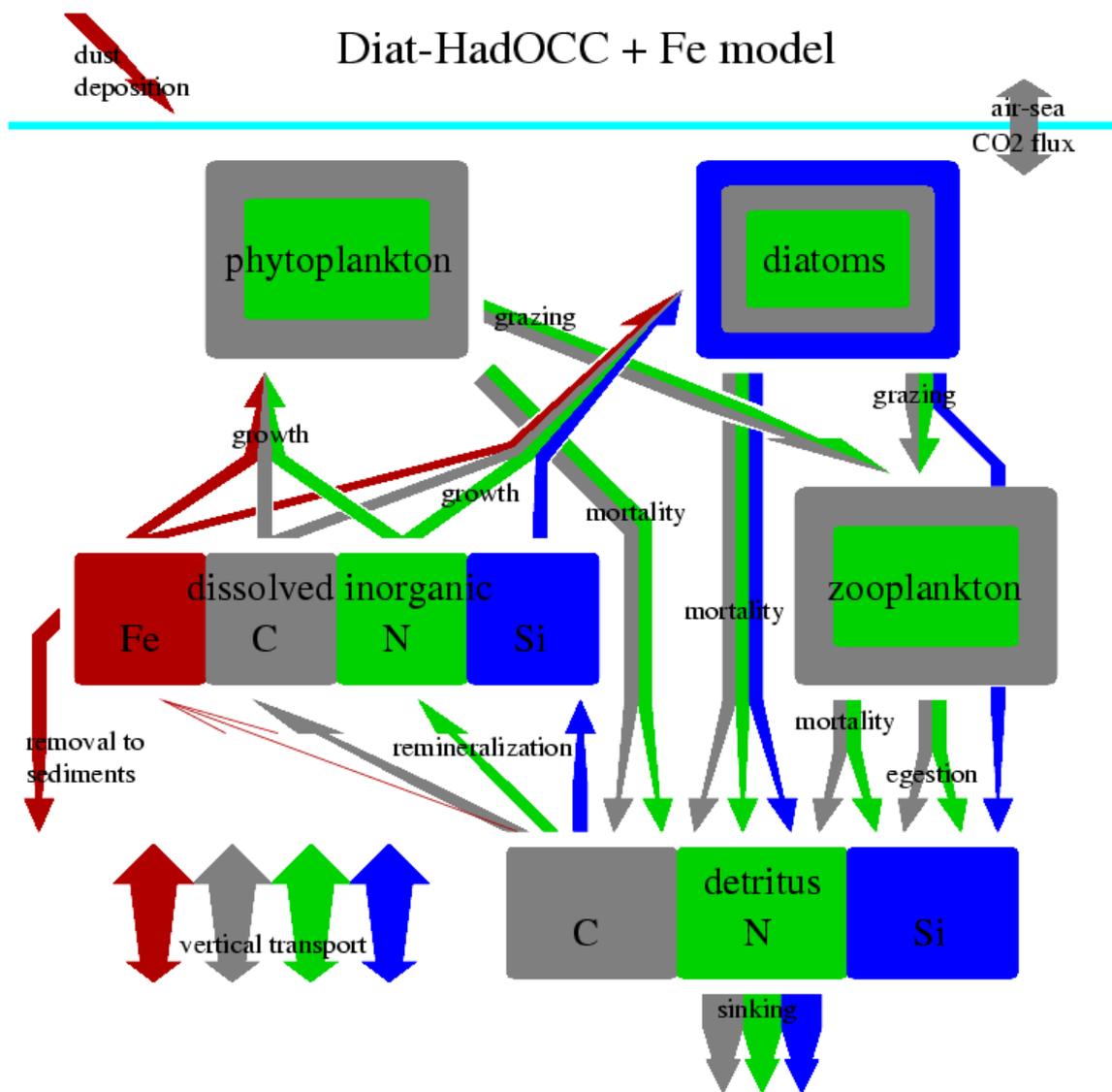
**Figure 1.** Diagram of the Diat-HadOCC model components and flows of nitrogen, carbon, silicon and iron
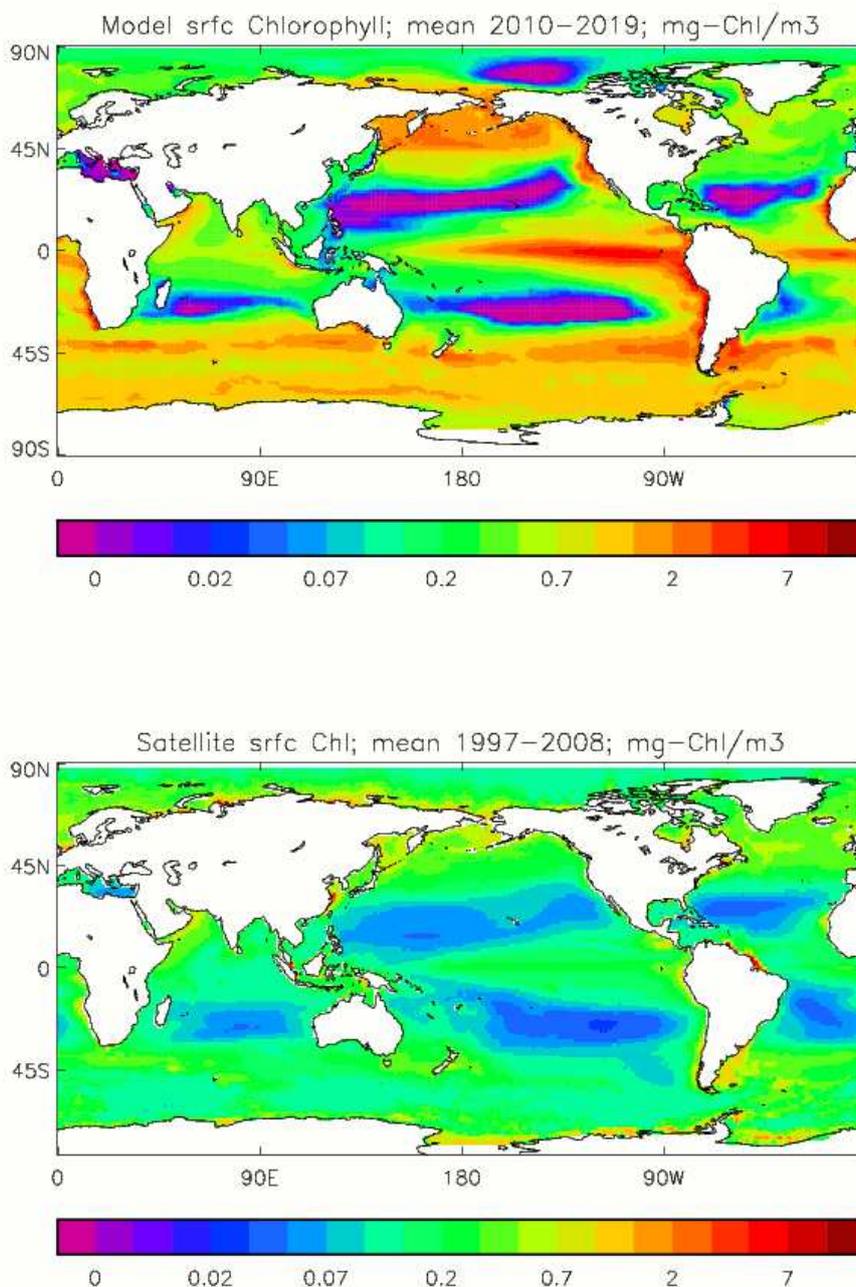
**Figure 2.** Comparison of surface chlorophyll: upper panel, mean over the years 2010-9 inclusive from the model, Historical+ RCP8.5 scenario; lower panel, mean over 1998-2007 from GlobColor, with further processing as described in (Ford et al., 2012). Units are mg Chl $m^{-3}$

Geoscientific
Model Development
Discussions
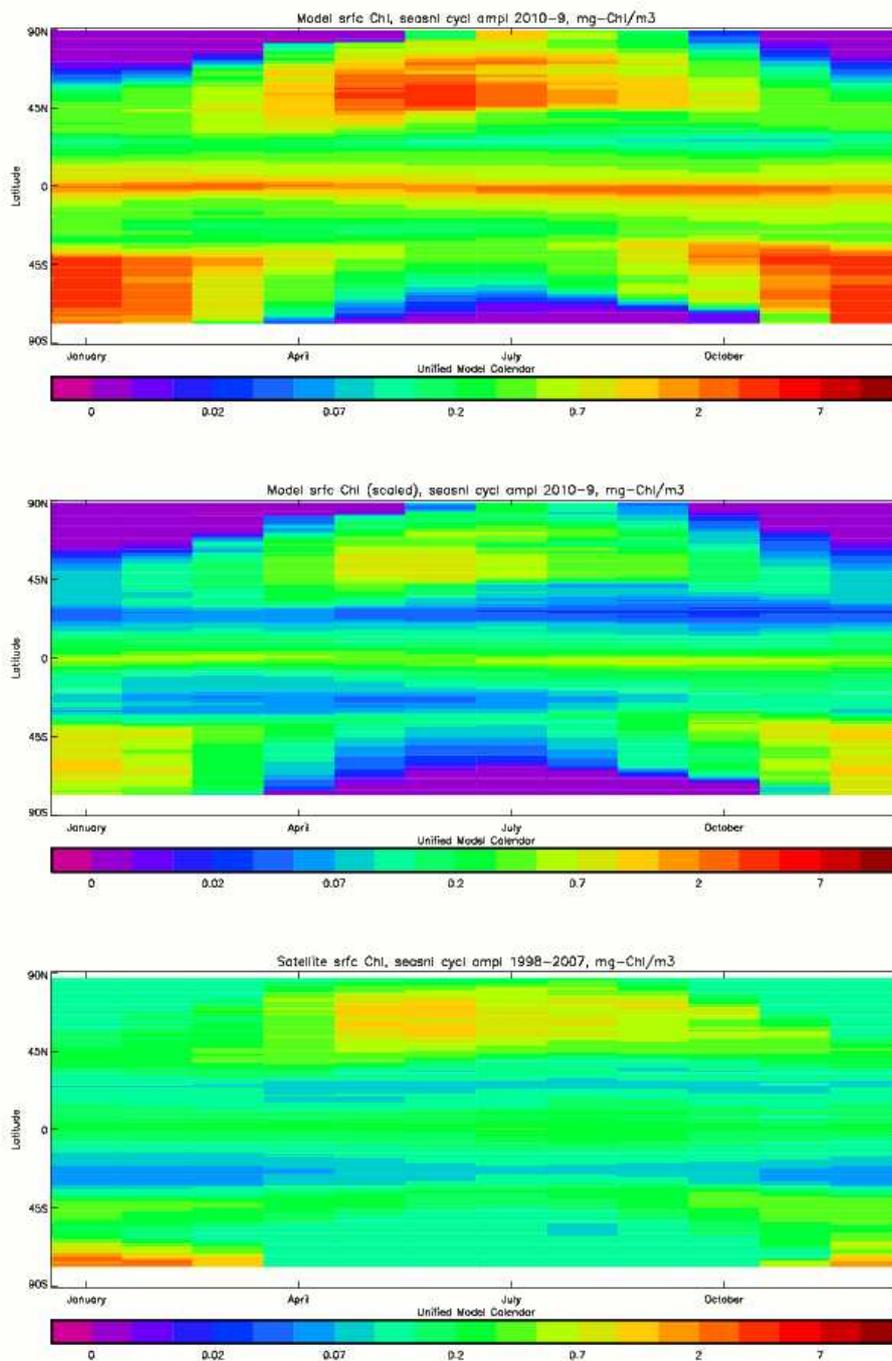


**Figure 3.** Seasonal cycle of global zonal mean surface chlorophyll, in mg Chl m$^{-3}$: top panel, average over the years 2010-9 inclusive from the model, Historical+RCP8.5 scenario; middle, the same but scaled by factor 0.213/0.812 (=0.262) so that the model mean matches the observations; bottom, satellite-derived data from GlobColor, averaged over 1998-2007 inclusive.
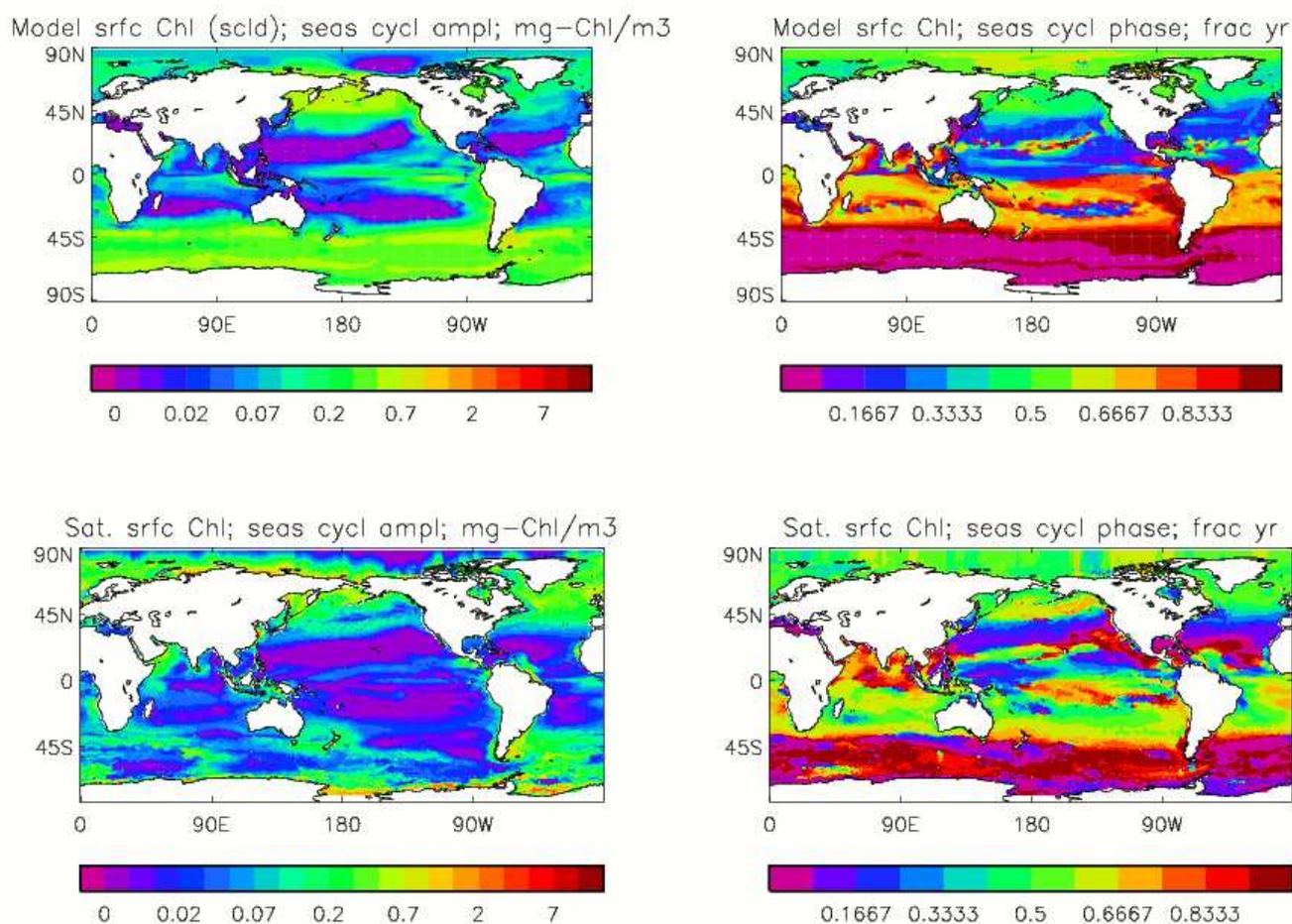
**Figure 4.** The amplitude (left-hand panels; units are mg Chl m$^{-3}$) and phase (right-hand panels; units are 'fraction of year') of the seasonal cycle of surface chlorophyll in the model (upper panels; average over years 2010-9, Historical+RCP8.5 scenario, amplitude scaled by factor of 0.213/0.812) and in the GlobColor data (lower panels; average over years 1998-2007). The amplitude has been determined by finding the best-fitting sine-curve through the monthly-mean values of the average cycle at each point, and the phase refers to the fraction of the year when the fitted curve is at its maximum.
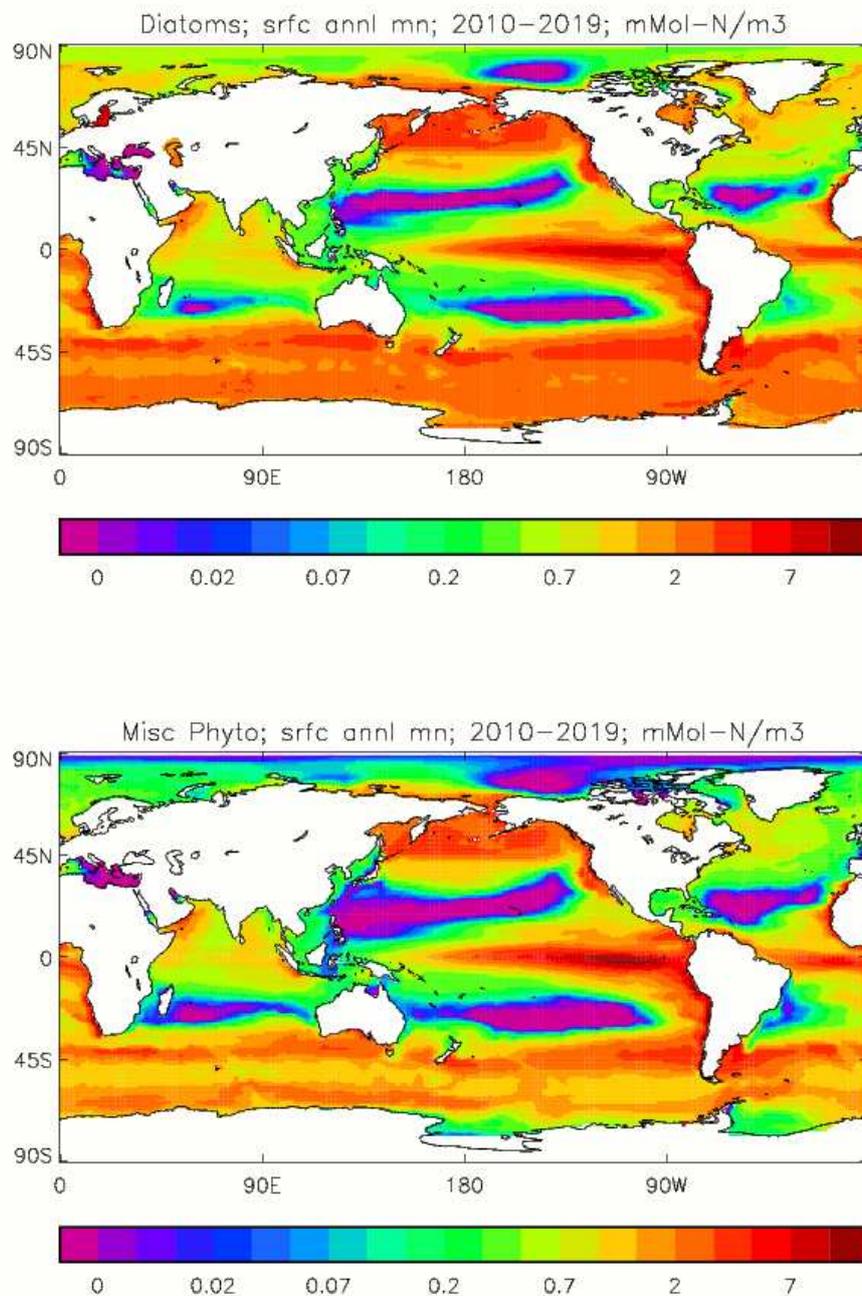
**Figure 5.** Phytoplankton surface biomass (in mMol N m$^{-3}$), averaged over the model years 2010-2019 inclusive, for (upper panel) Diatoms, and (lower panel) misc-Phytoplankton.

Geoscientific
Model Development
Discussions
Open Access
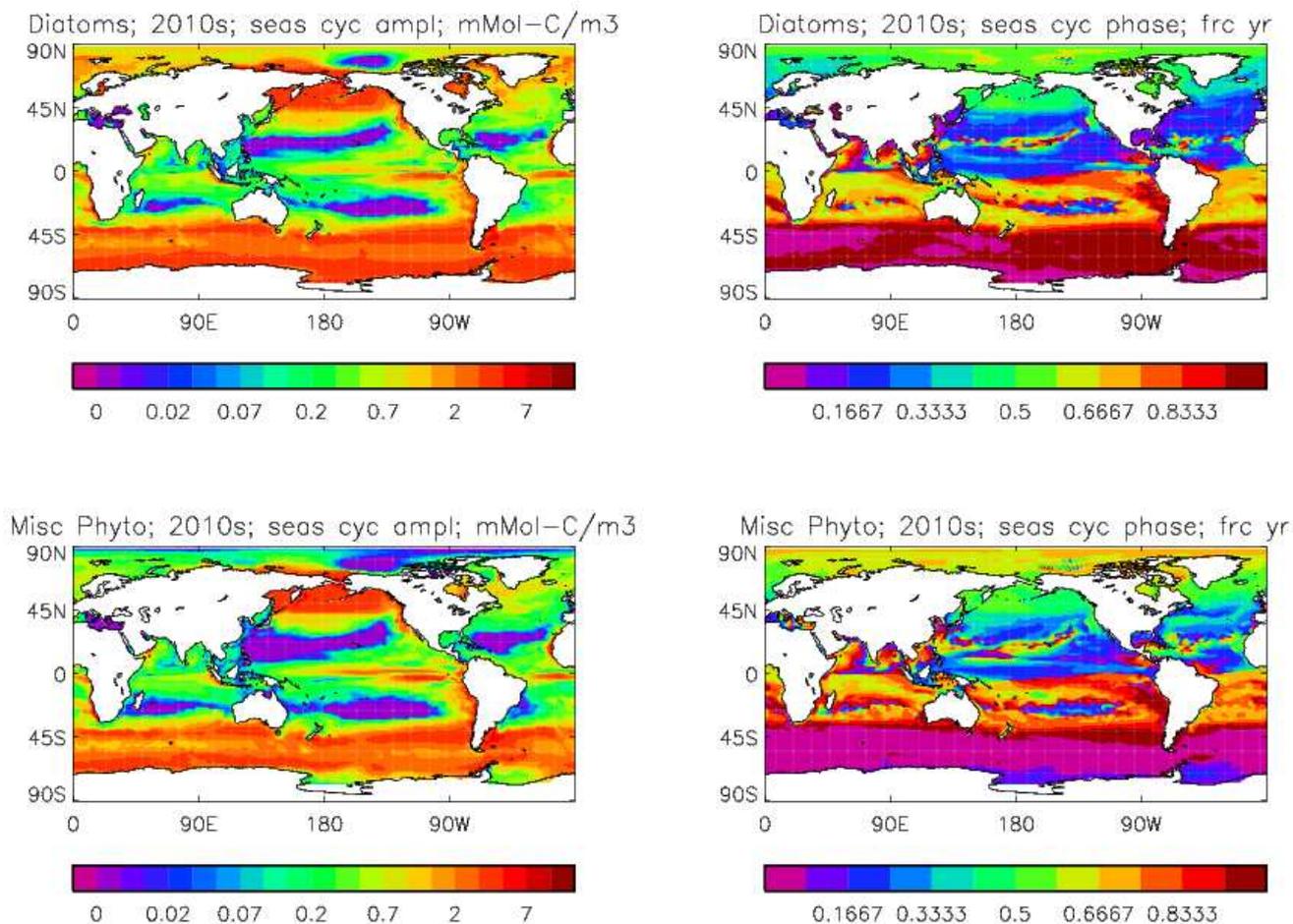


**Figure 6.** Phytoplankton surface biomass mean seasonal cycle, averaged over model years 2010 to 2019 inclusive, for (upper panels) Diatoms and (lower panels) misc-Phytoplankton. Left-hand panels show the amplitude (in mMol N m$^{-3}$) and the right-hand panels the phase (in fraction of calendar year).
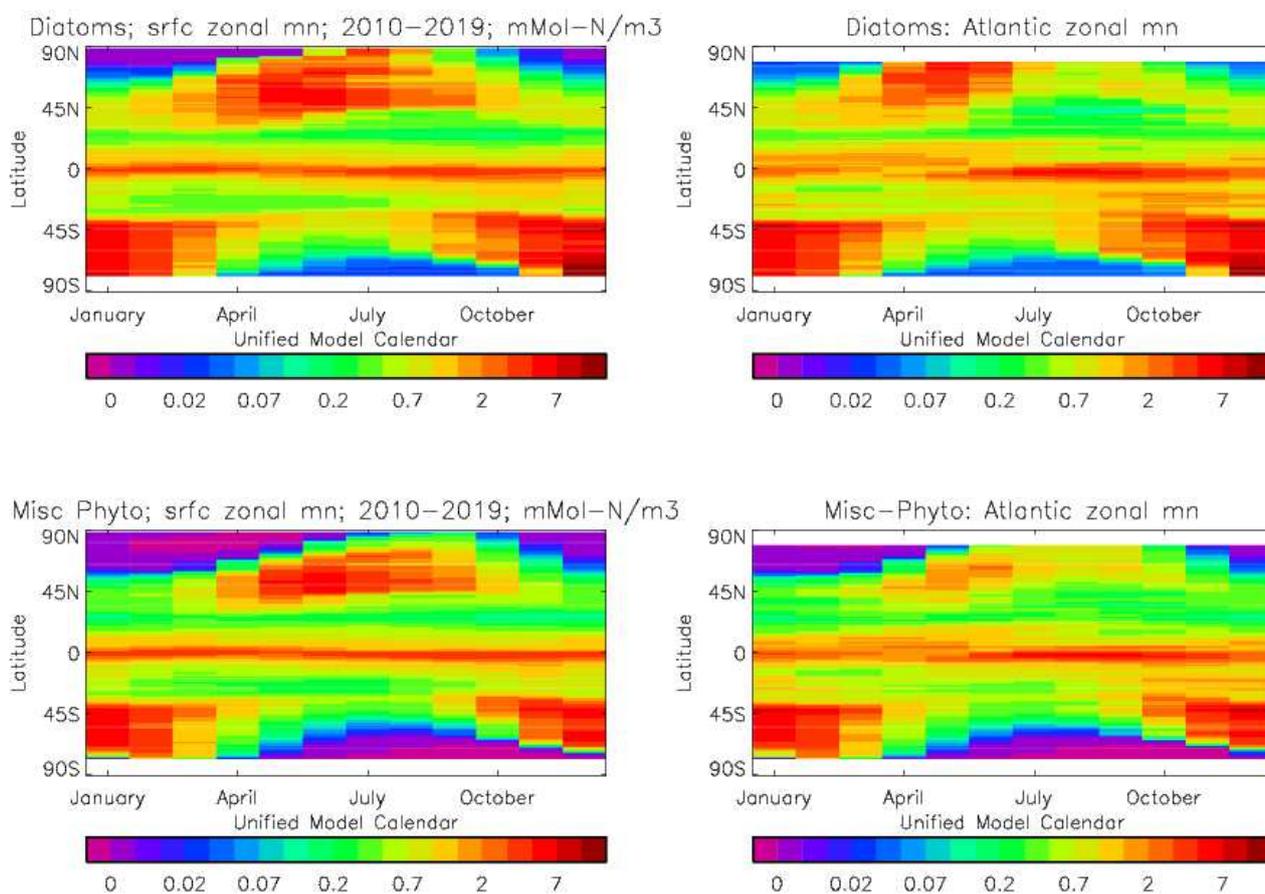
**Figure 7.** Phytoplankton surface biomass (in mMol N m$^{-3}$), zonal mean (taken globally for left-hand panels, across Atlantic basin only for right-hand panels), averaged for each month over the model years 2010-2019 inclusive: upper panels, Diatoms; lower panels, misc-Phytoplankton
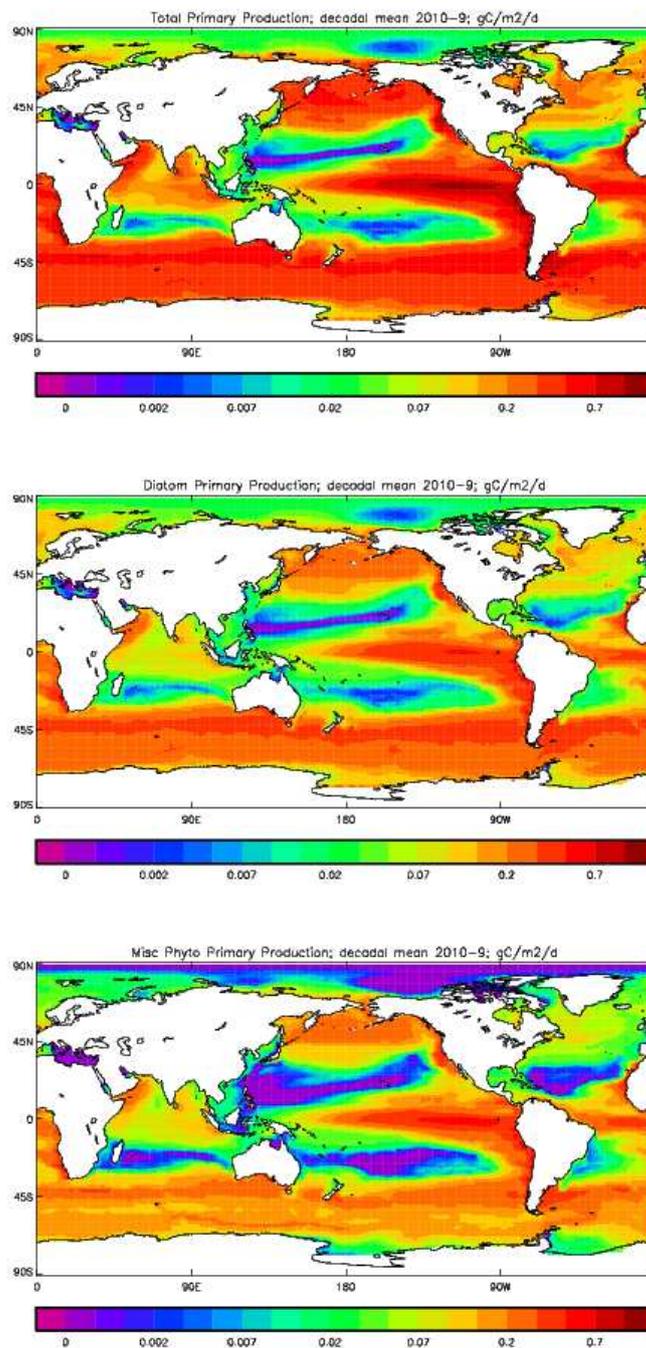
**Figure 8.** Primary Production (g C m$^{-2}$ d$^{-1}$), depth-integrated, averaged over the model years 2010-2019 inclusive: bottom panel, PP by misc-Phytoplankton; middle panel, that by Diatoms; top panel, total by both phytoplankton types
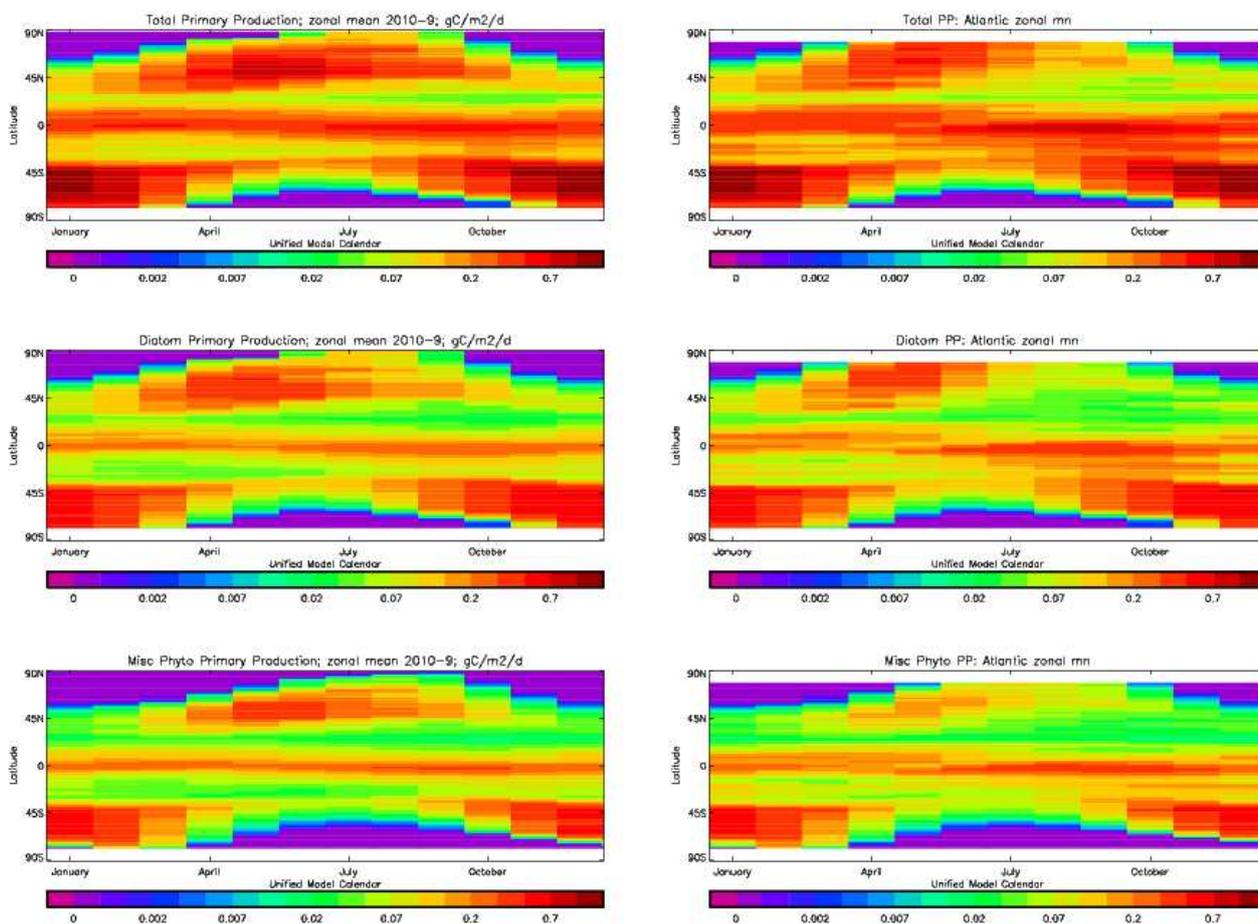
**Figure 9.** Primary Production (g C m$^{-2}$ d$^{-1}$), depth-integrated, zonally-meaned, averaged for each month over the model years 2010-2019 inclusive: bottom panels, PP by misc-Phytoplankton; middle, that by Diatoms; top, total by both phytoplankton types. The left-hand panels show global zonal means, while the right-hand panels show zonal means across the Atlantic basin only.
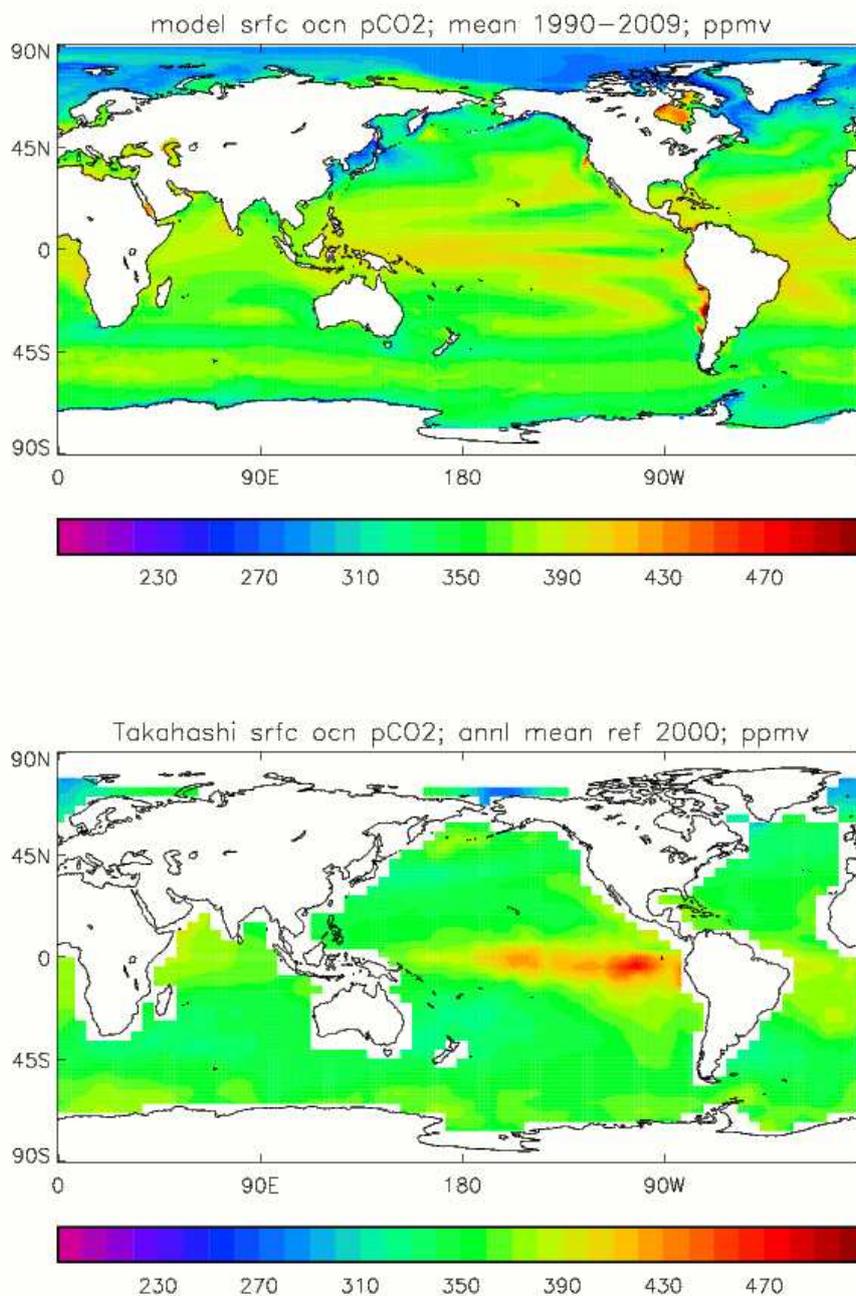
**Figure 10.** Surface ocean pCO2 (in ppmv): upper panel, model field averaged over the model years 1990-2009 inclusive; lower panel, Takahashi gridded field from data, annual mean, referenced to the year 2000
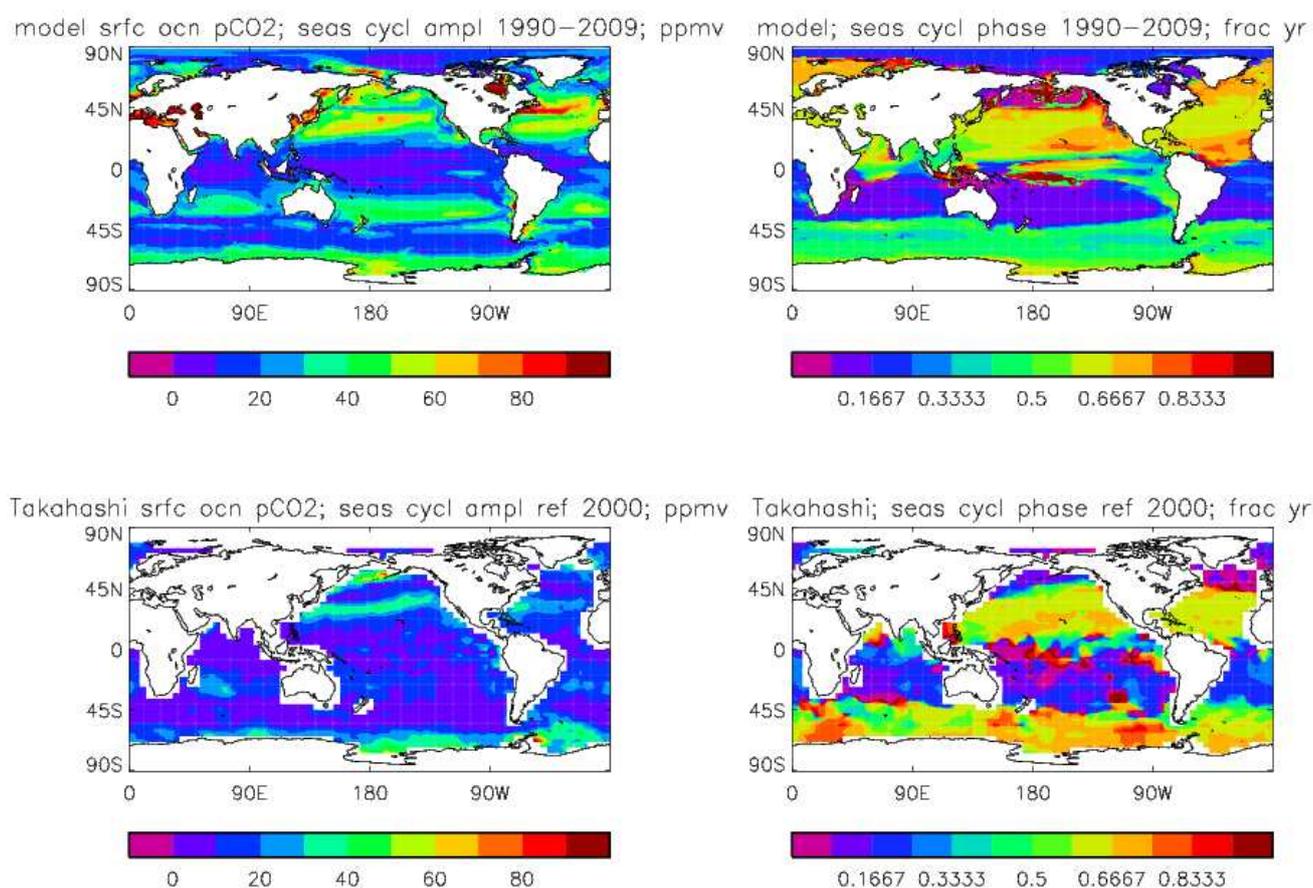
**Figure 11.** Surface ocean pCO2, seasonal cycle: upper panels, model, averaged over model years 1990-2009 inclusive; lower panels, Takahashi gridded data, referenced to the year 2000; left-hand panels, amplitude of the cycle (ppmv); right-hand panels, phase of the cycle (in fraction of year)
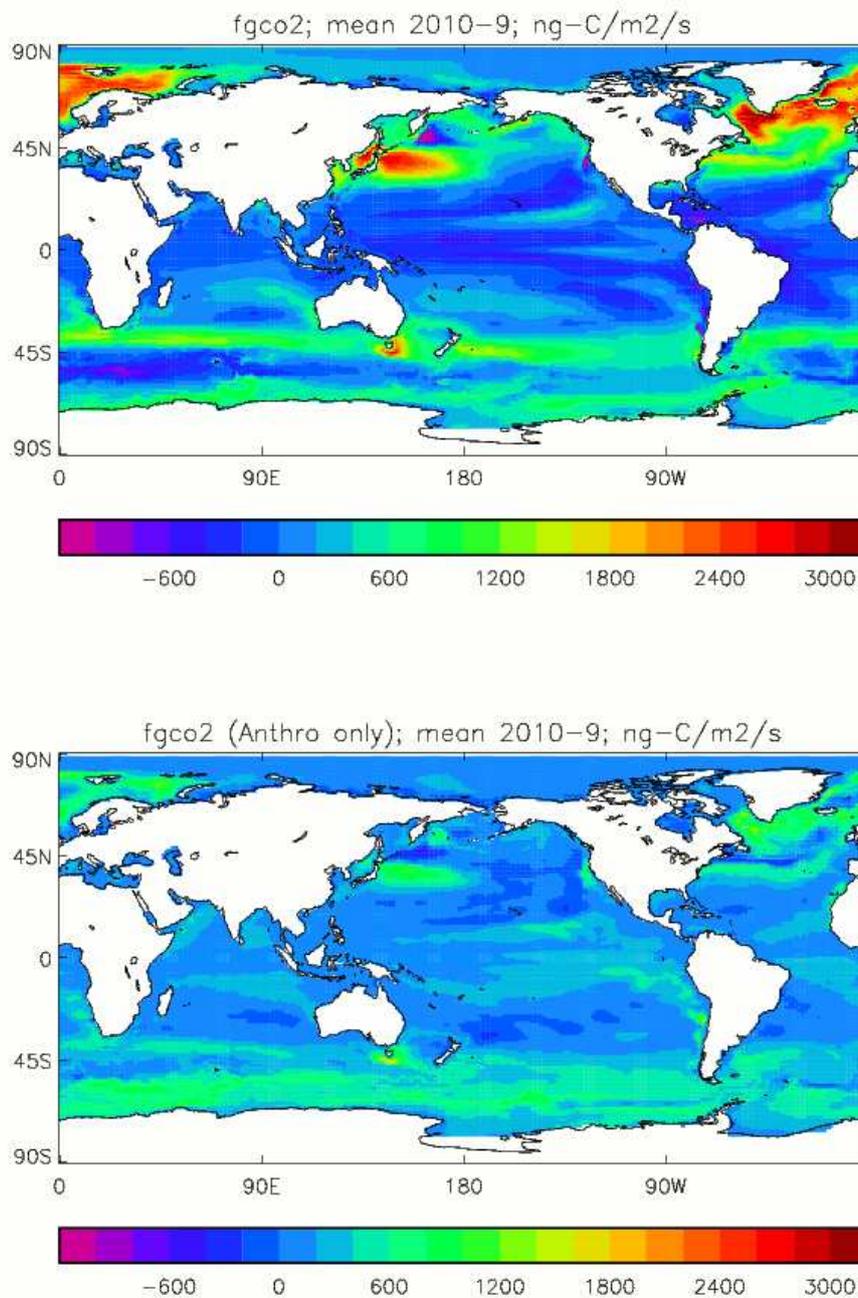
**Figure 12.** Total air-to-sea flux of $CO_2$ (ng C m$^{-2}$ s$^{-1}$; positive values into the ocean), mean over model years 2010-2019 inclusive: upper panel, total flux (natural cycle and anthropogenic perturbation); lower panel, anthropogenic perturbation
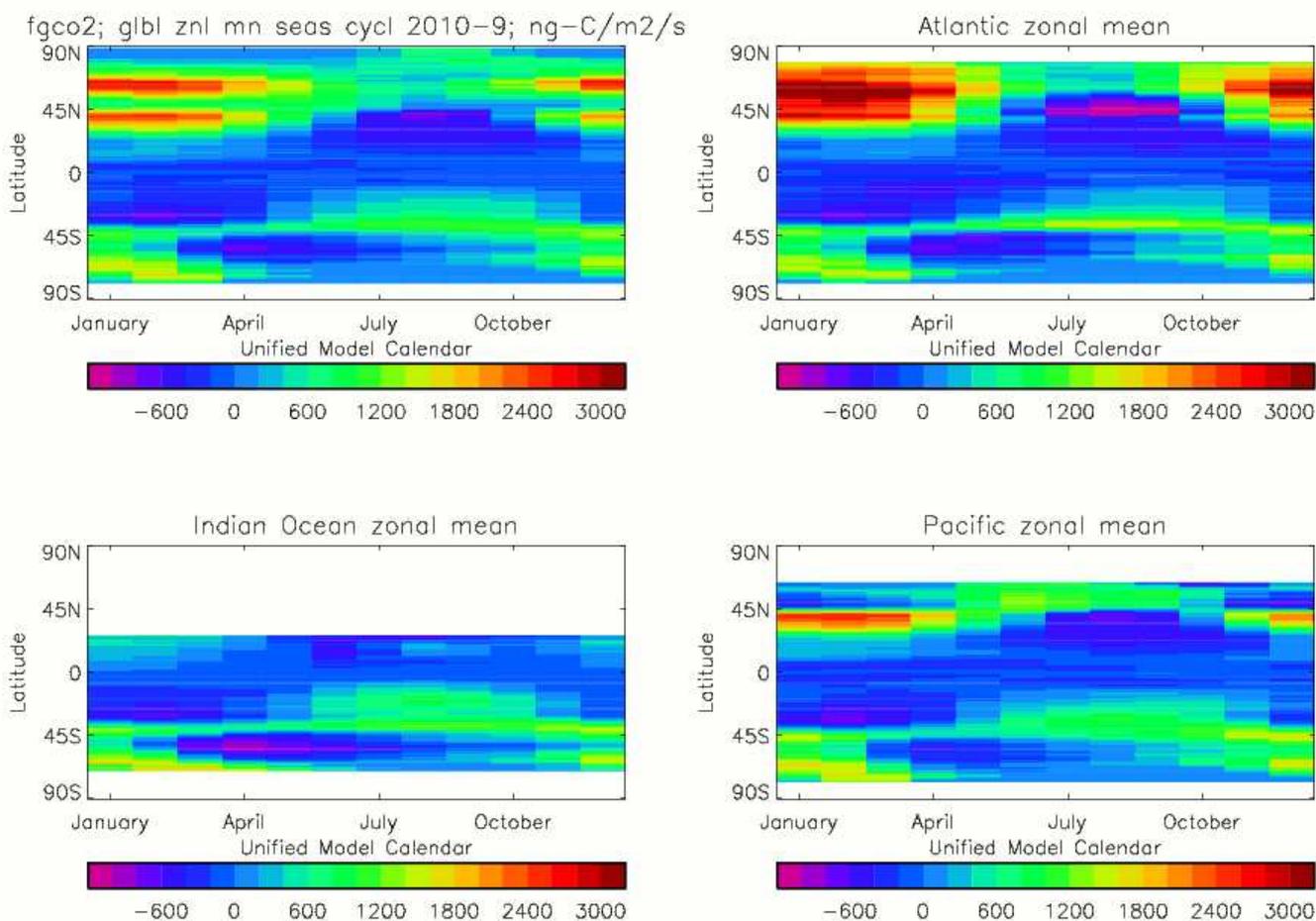
**Figure 13.** Total air-to-sea flux of $CO_2$ (ng C m$^{-2}$ s$^{-1}$), seasonal cycle averaged for each month over the model years 2010-2019 inclusive, zonally-meaned: upper left panel, global zonal mean; upper right, zonal mean of the Atlantic Ocean basin; lower left, zonal mean of the Indian Ocean basin; lower right, zonal mean of the Pacific Ocean basin
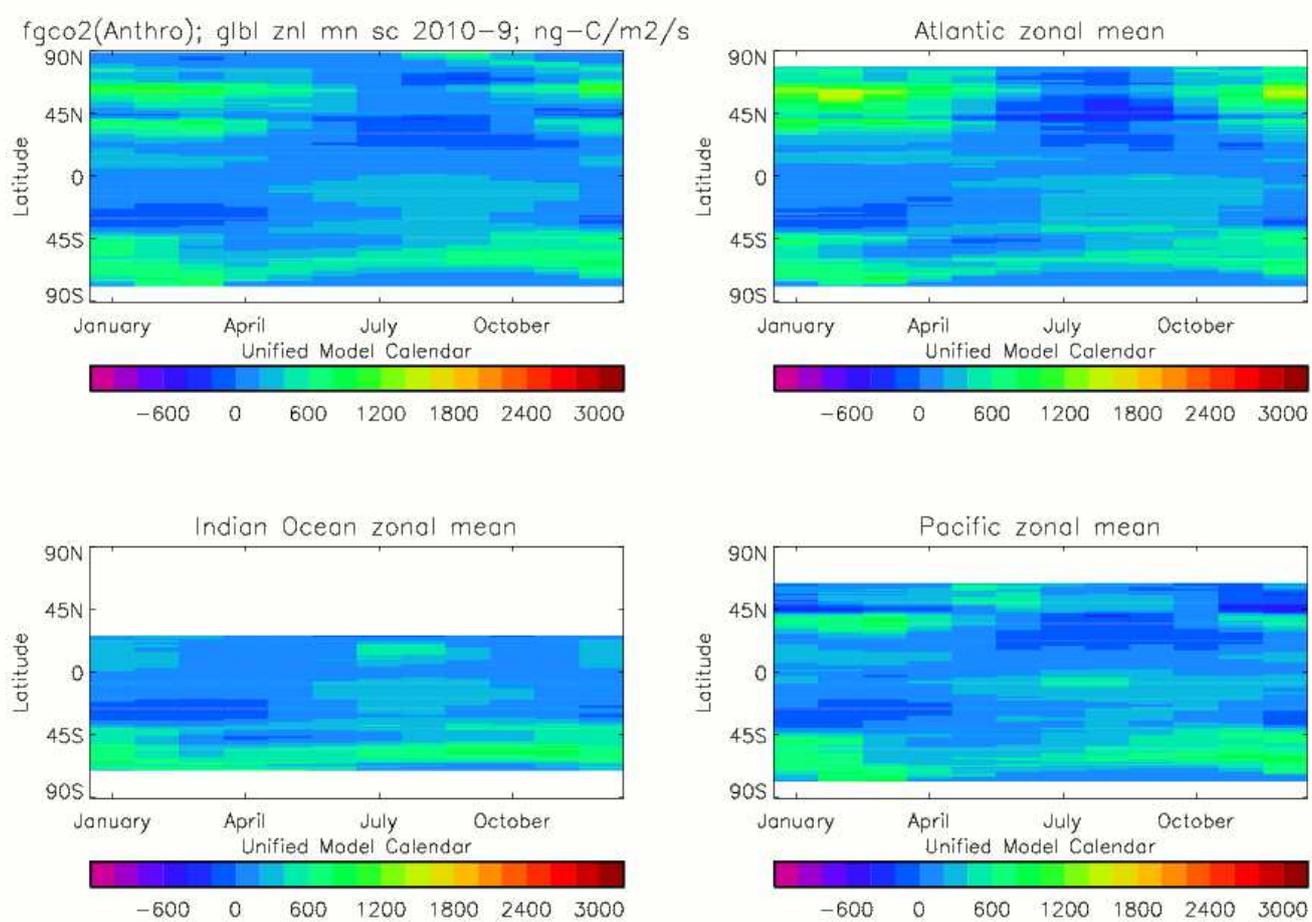
**Figure 14.** As Figure 13, but for the air-to-sea flux of anthropogenic $CO_2$ only (ng C m$^{-2}$ s$^{-1}$)
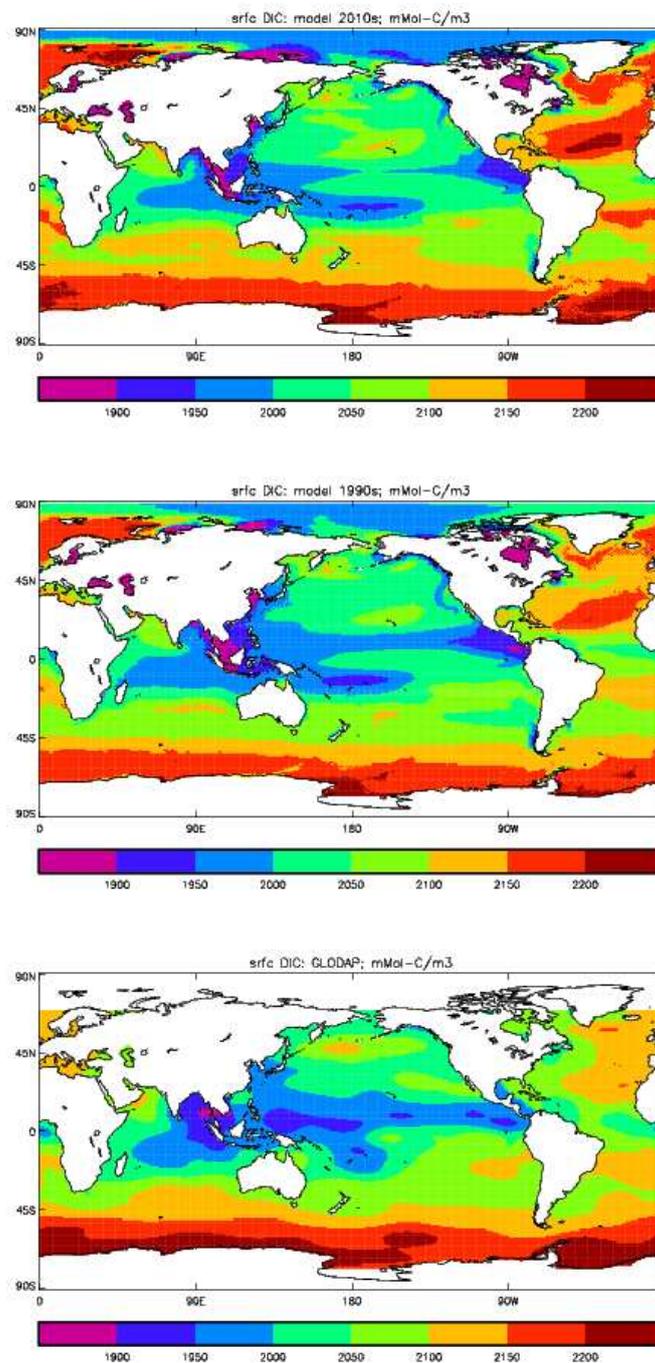
**Figure 15.** Surface concentration of Dissolved Inorganic Carbon (mMol C m$^{-3}$): top panel, model field averaged over model years 2010-2019 inclusive; middle, model field averaged over model years 1990-1999 inclusive; bottom, the gridded field from the GLODAP database
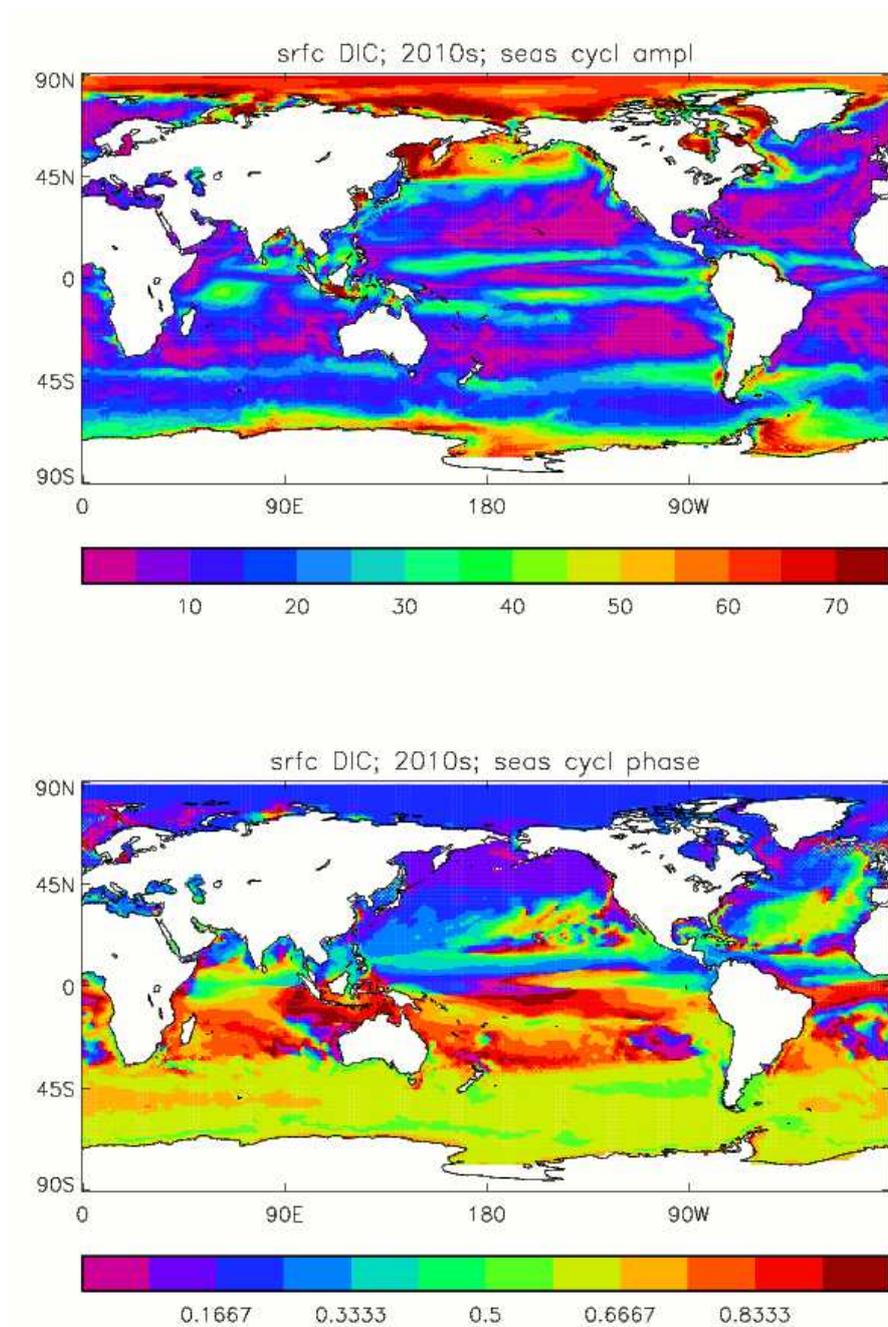
**Figure 16.** Surface DIC, model seasonal cycle, averaged over model years 2010-2019 inclusive: upper panel, amplitude of cycle (mMol C m$^{-3}$); lower panel, phase of cycle (fraction of year)
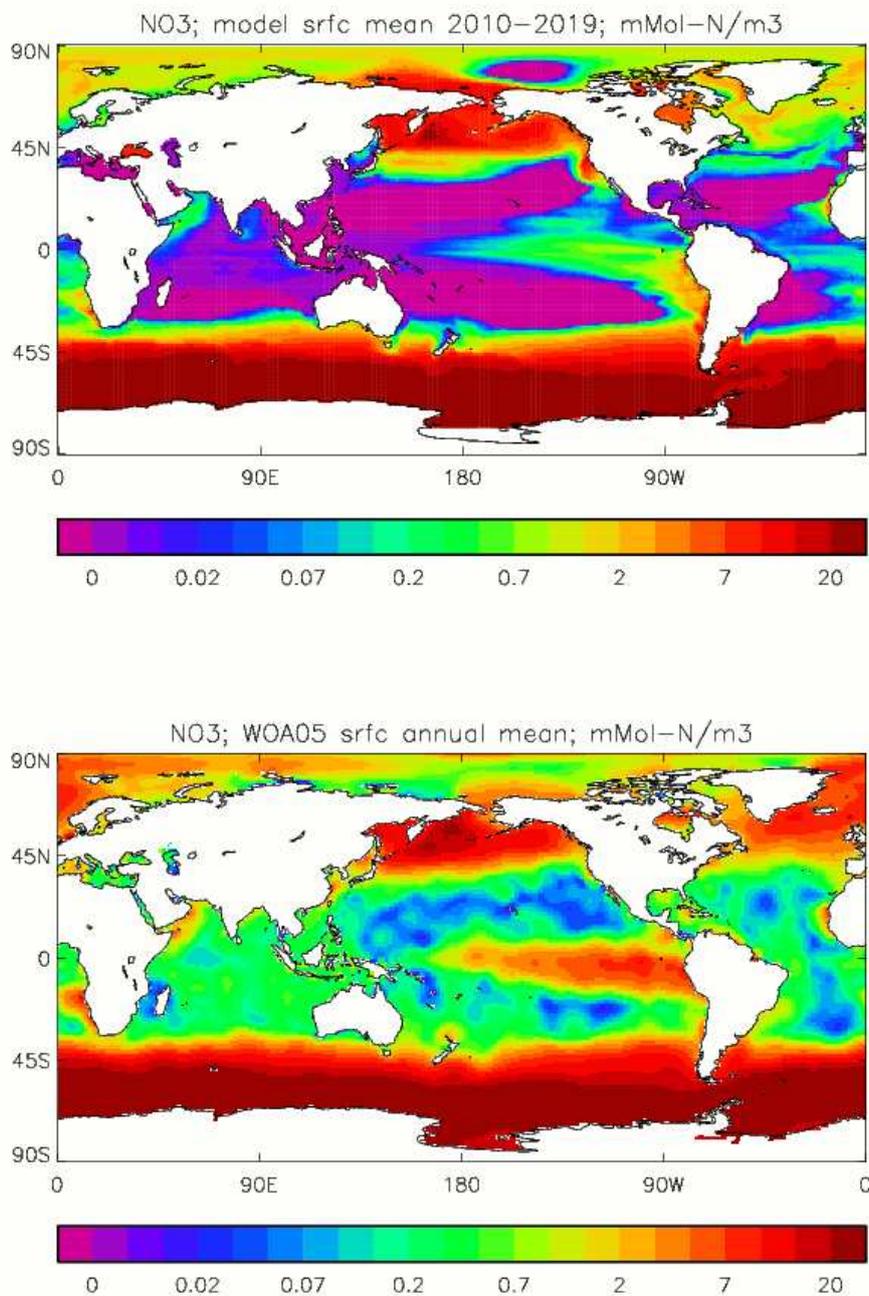
**Figure 17.** Surface dissolved nitrate (mMol N m$^{-3}$): upper panel, model field averaged over model years 2010-2019 inclusive; lower panel, the gridded field from the 2005 World Ocean Atlas
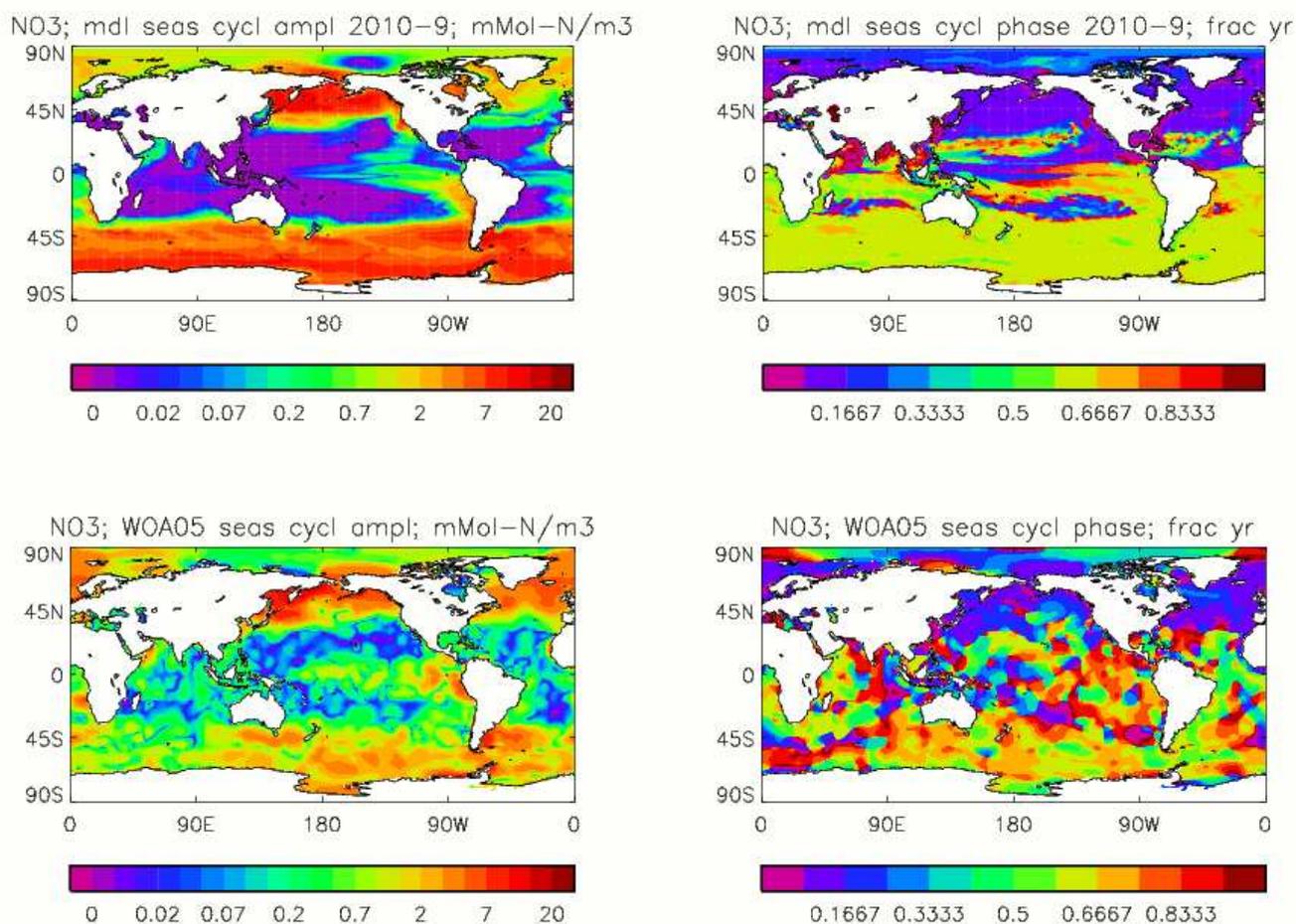
**Figure 18.** Surface dissolved nitrate, seasonal cycle: upper panels, model cycle, averaged over model years 2010-2019 inclusive; lower panels, the cycle from the monthly gridded fields from the 2005 World Ocean Atlas; left-hand panels, the amplitude of the cycle (mMol N m$^{-3}$); right-hand panels, the phase of the cycle (fraction of year)
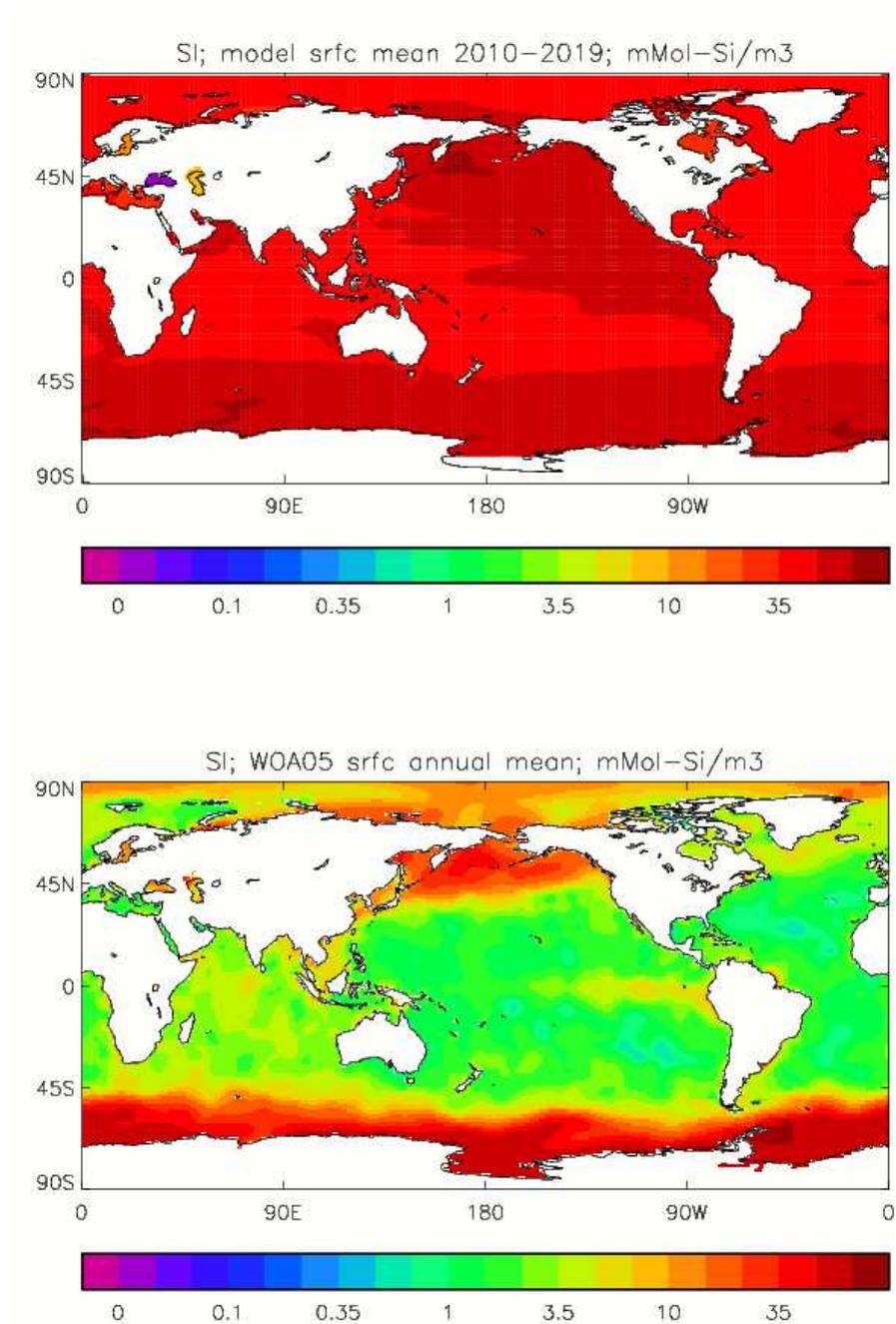
**Figure 19.** Surface dissolved silicate (mMol Si m$^{-3}$): upper panel, model field averaged over model years 2010-2019 inclusive; lower panel, the gridded field from the 2005 World Ocean Atlas
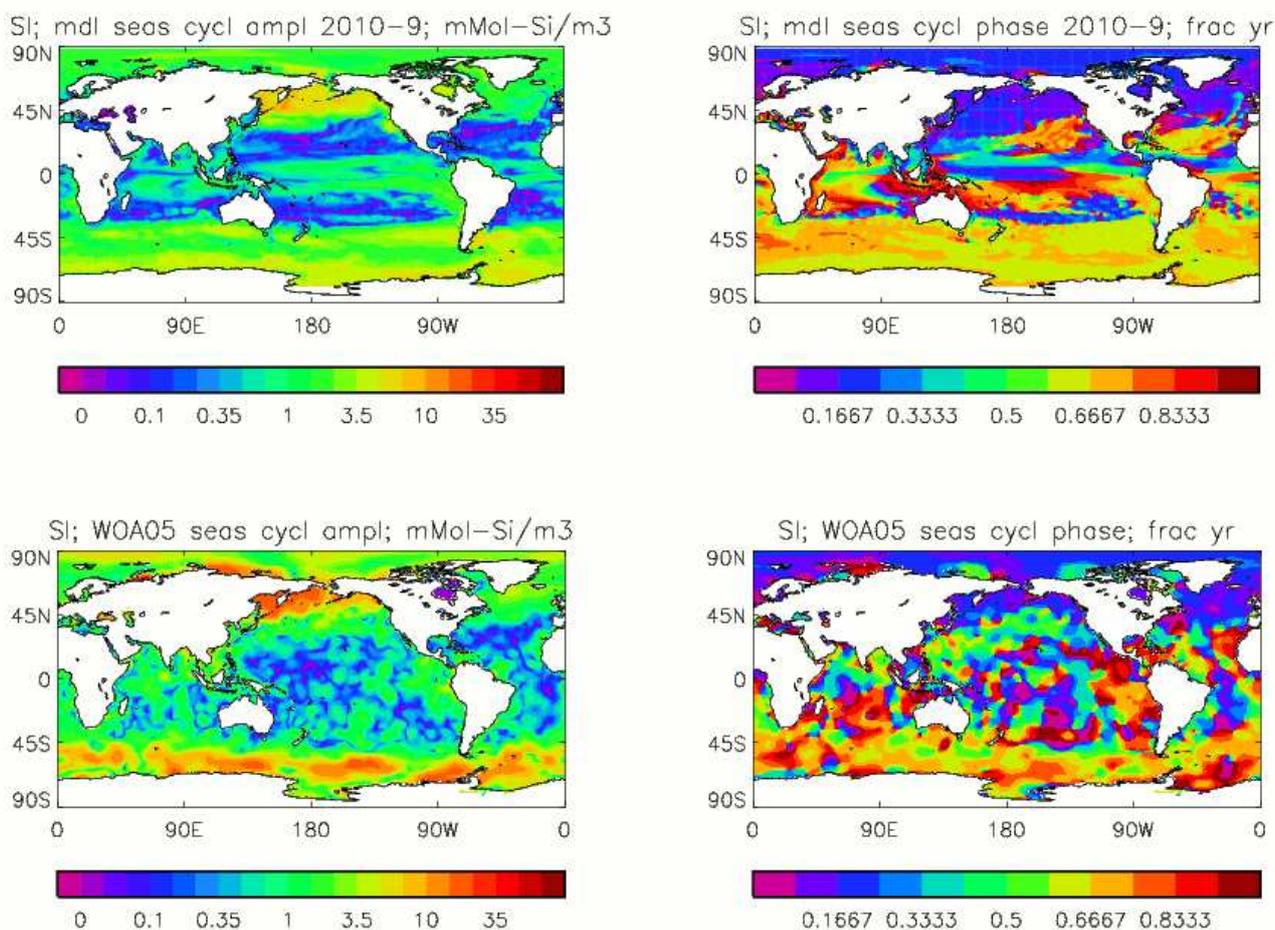
**Figure 20.** Surface dissolved silicate, seasonal cycle: upper panels, model cycle, averaged over model years 2010-2019 inclusive; lower panels, the cycle from the monthly gridded fields from the 2005 World Ocean Atlas; left-hand panels, the amplitude of the cycle (mMol Si m$^{-3}$); right-hand panels, the phase of the cycle (fraction of year)
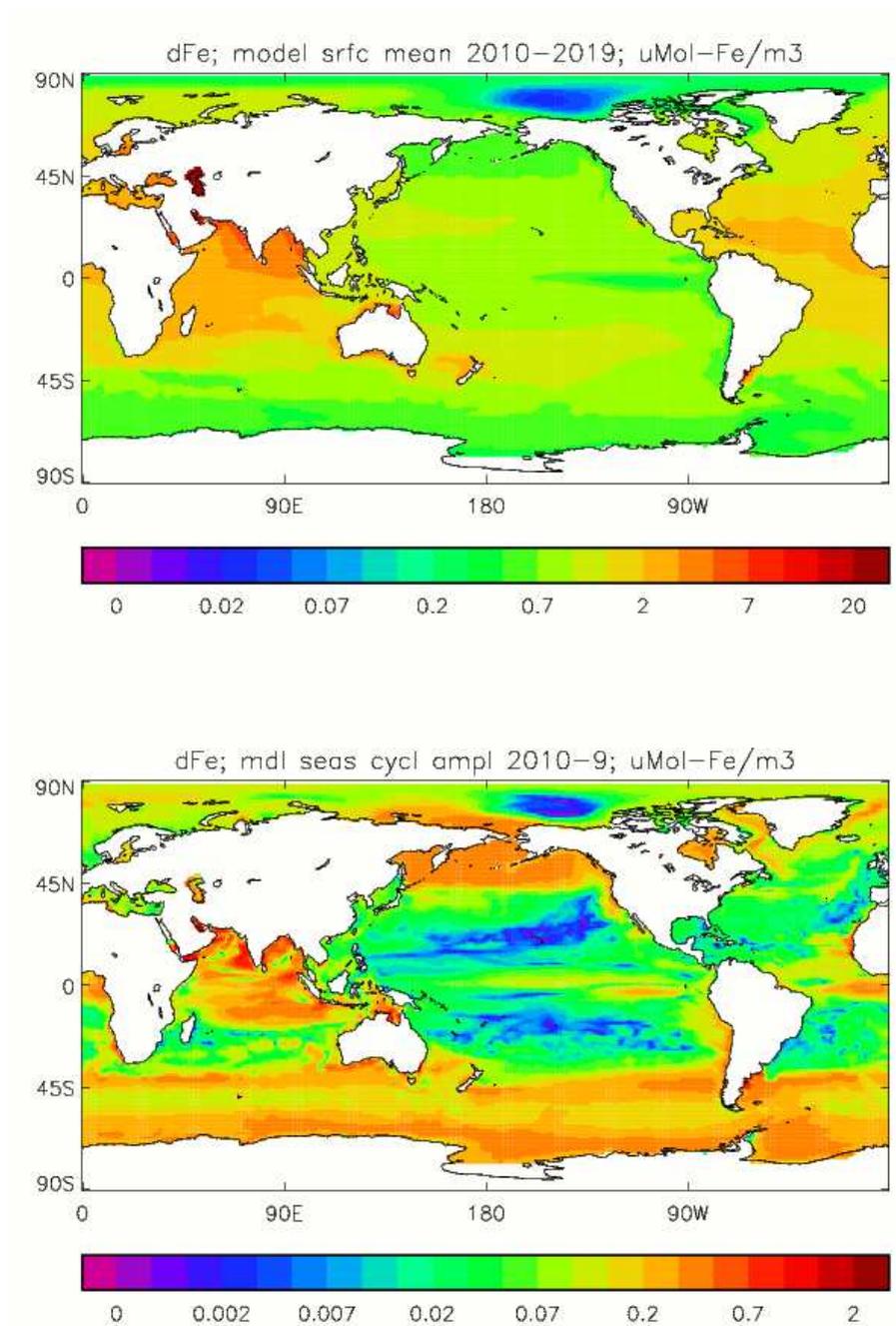
**Figure 21.** Surface dissolved iron (uMol Fe m$^{-3}$): upper panel, model field averaged over model years 2010-2019 inclusive; lower panel, amplitude of the model seasonal cycle averaged over the same period
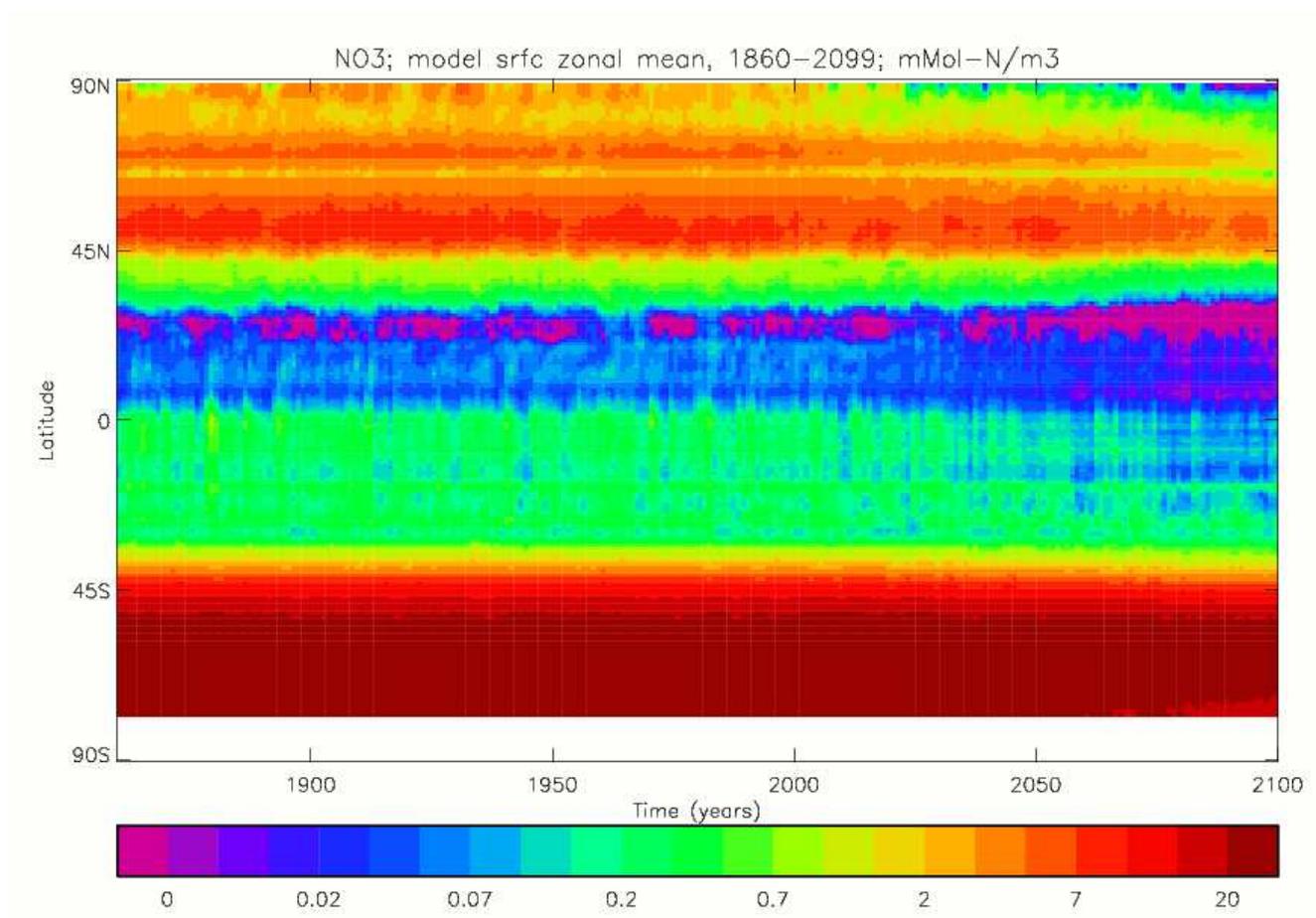
**Figure 22.** Surface dissolved nitrate concentration (mMol N m$^{-3}$), global zonal and annual means for model years 1860 to 2099, from the CMIP5 Historical and RCP8.5 simulations, showing the response to changing climatic forcing

Geoscientific
Model Development
Discussions
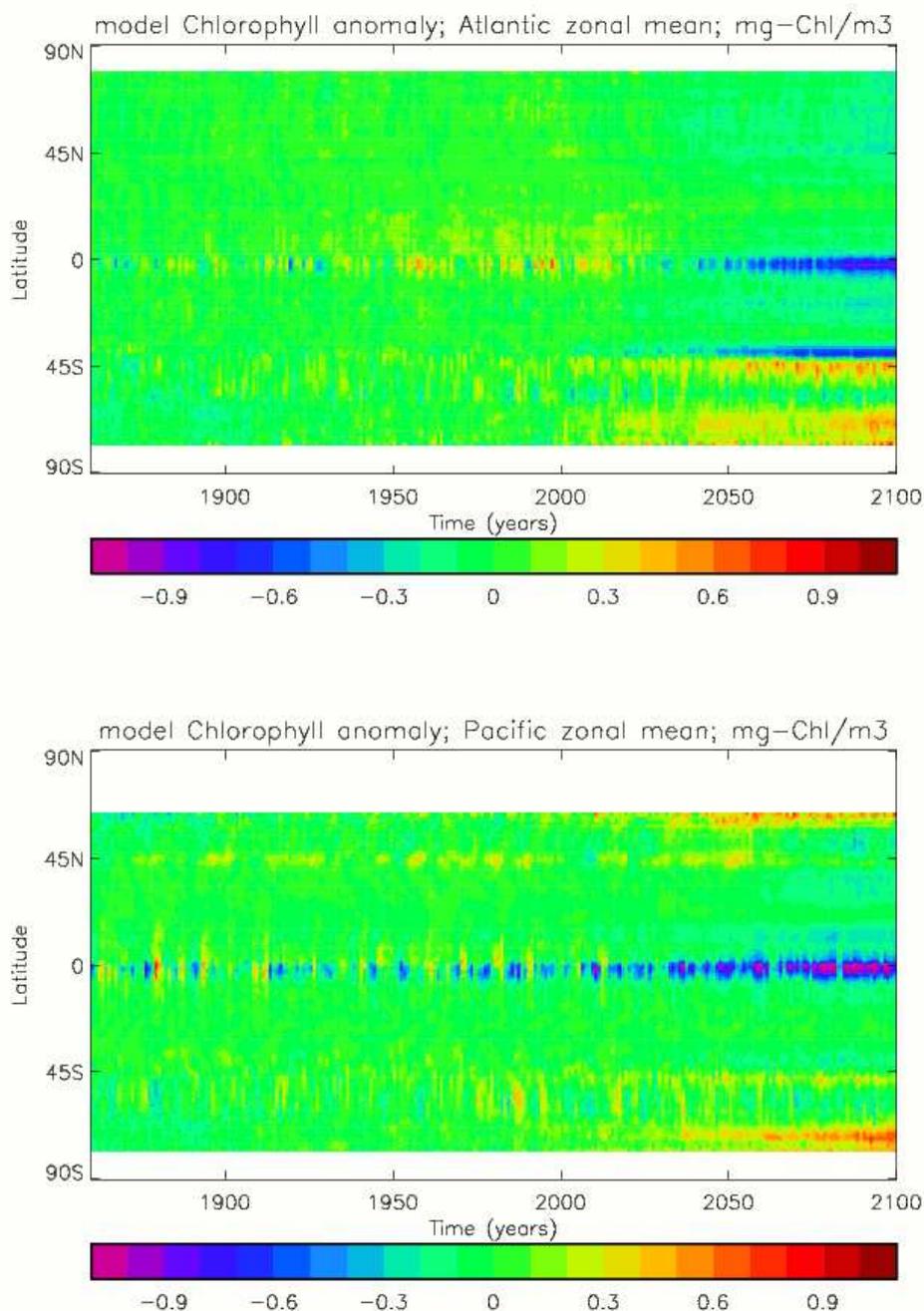


**Figure 23.** Surface total chlorophyll concentration anomaly (mg Chl m$^{-3}$), zonal and annual means for model years 1860 to 2099, from the CMIP5 Historical and RCP8.5 simulations: upper panel, zonal mean of the Atlantic Ocean basin; lower panel, zonal mean of the Pacific Ocean basin. The anomaly has been calculated by subtracting the surface chlorophyll concentration field, meaned over the years 1860 to 2099 inclusive, as produced by the piControl simulation from the annual means of the Historical and RCP8.5 simulations
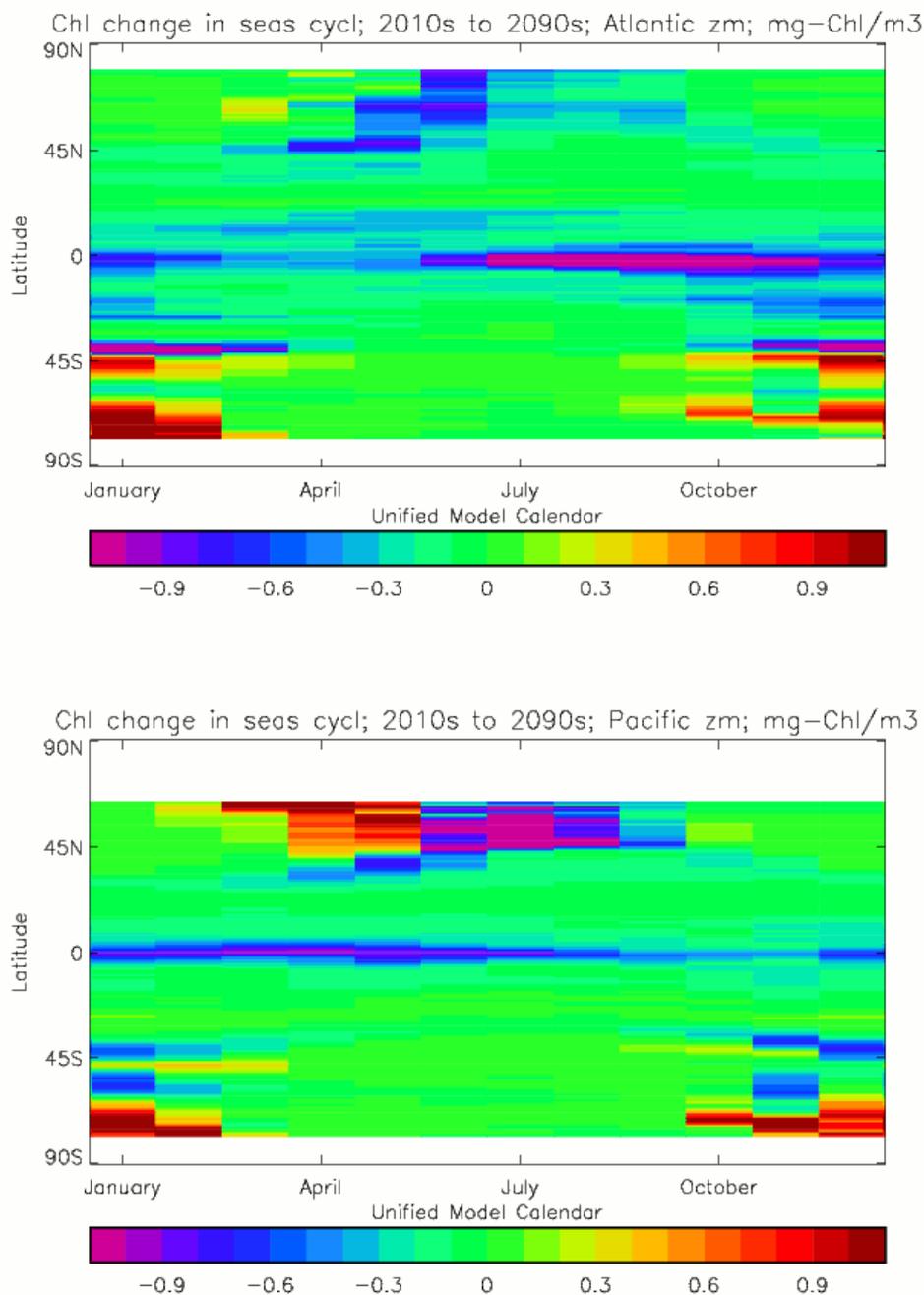
**Figure 24.** Change in the seasonal cycle of surface chlorophyll concentration in the CMIP5 RCP8.5 simulation: change is calculated between the mean seasonal cycles of the model years 2090-2099 and 2010-2019. Zonal means of the (upper panel) Atlantic Ocean basin and (lower panel) Pacific Ocean basin
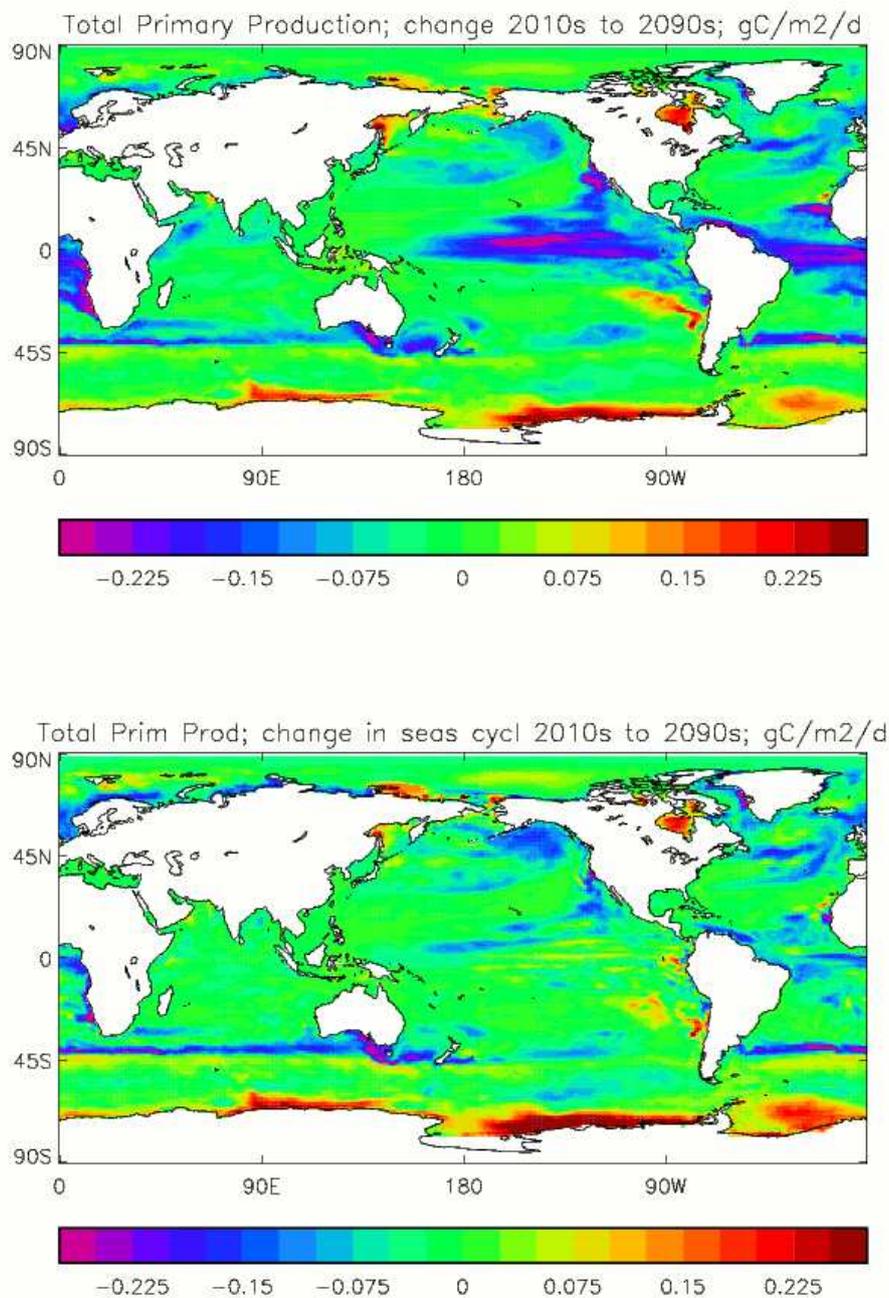
**Figure 25.** Change in the depth-integrated total Primary Production (mg C m$^{-2}$ d$^{-1}$) in the RCP8.5 simulation: difference between the model years 2090-2099 and 2010-2019. Upper panel: difference in decadal means; lower panel: difference in amplitude of mean seasonal cycle
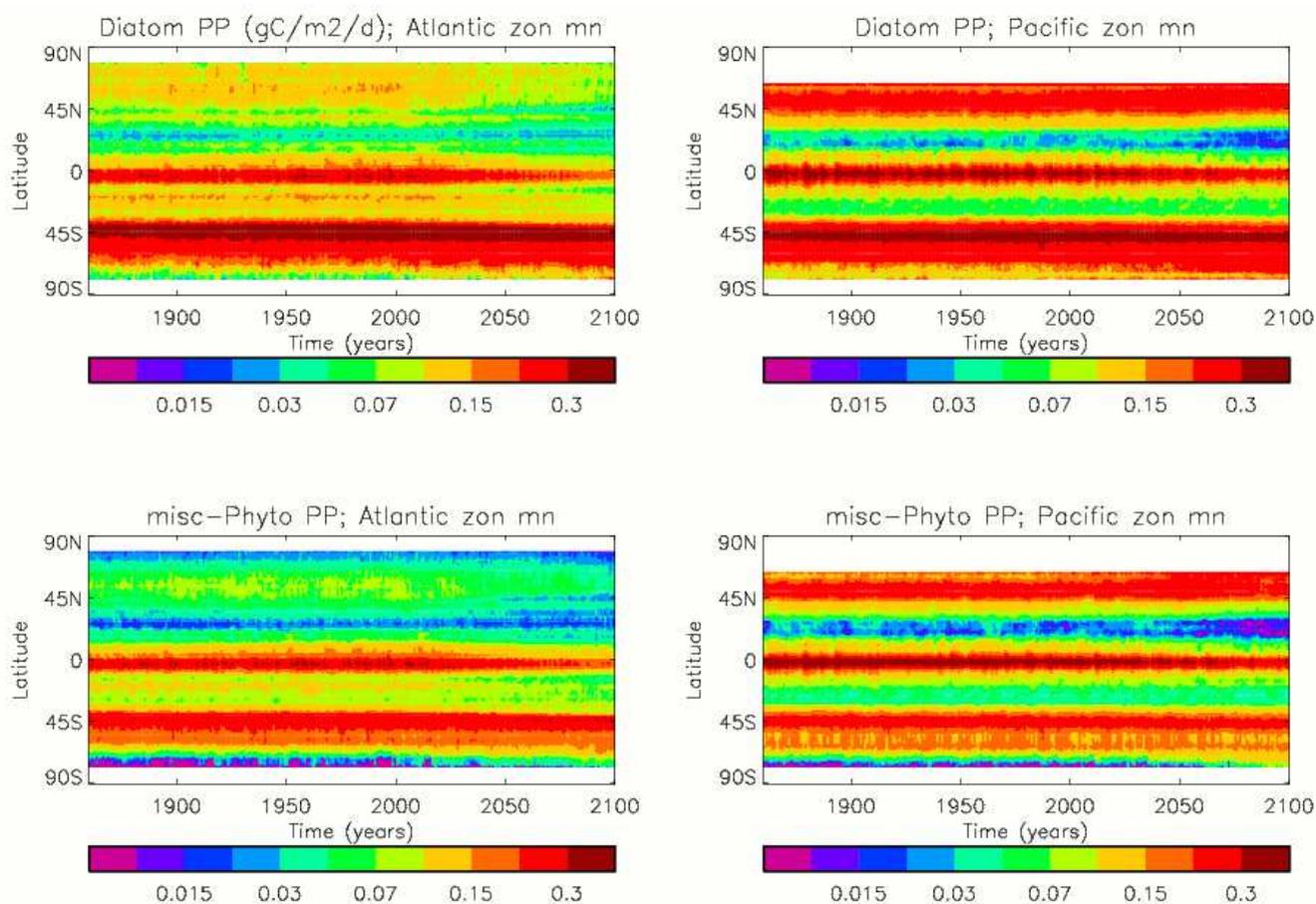
**Figure 26.** Change in annual mean depth-integrated Primary Production (mg C m$^{-2}$ d$^{-1}$) during the model years 1860 to 2099 in the CMIP5 Historical and RCP8.5 simulations. Upper panels, PP by Diatoms; lower panels, PP by misc-Phytoplankton; left-hand panels, Atlantic Ocean basin zonal mean; right-hand panels, Pacific Ocean basin zonal mean
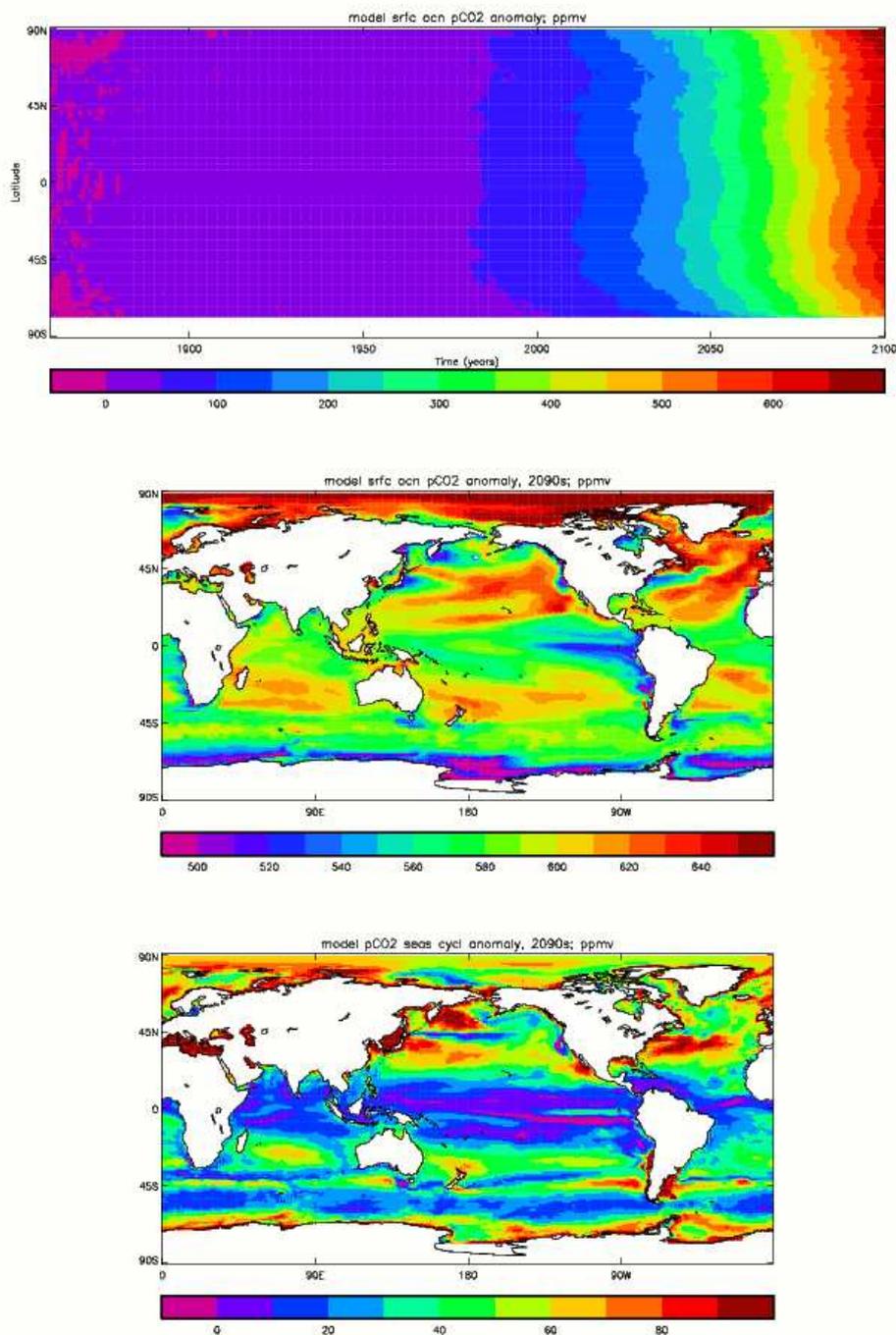
**Figure 27.** Change in surface pCO$_2$ (ppmv) during the model years 1860 to 2099 in the CMIP5 Historical and RCP8.5 simulations. Top panel: the anomaly over the period of the simulations, calculated by subtracting the annual means of the piControl simulation from those of the Historical and RCP8.5 simulations. Middle panel: the decadal mean anomaly during the model years 2090-2099, calculated by subtracting the relevant years of the piControl from those of the RCP8.5 simulation. Bottom panel: the seasonal cycle amplitude anomaly averaged over the model years 2090-2099, calculated as for the middle panel
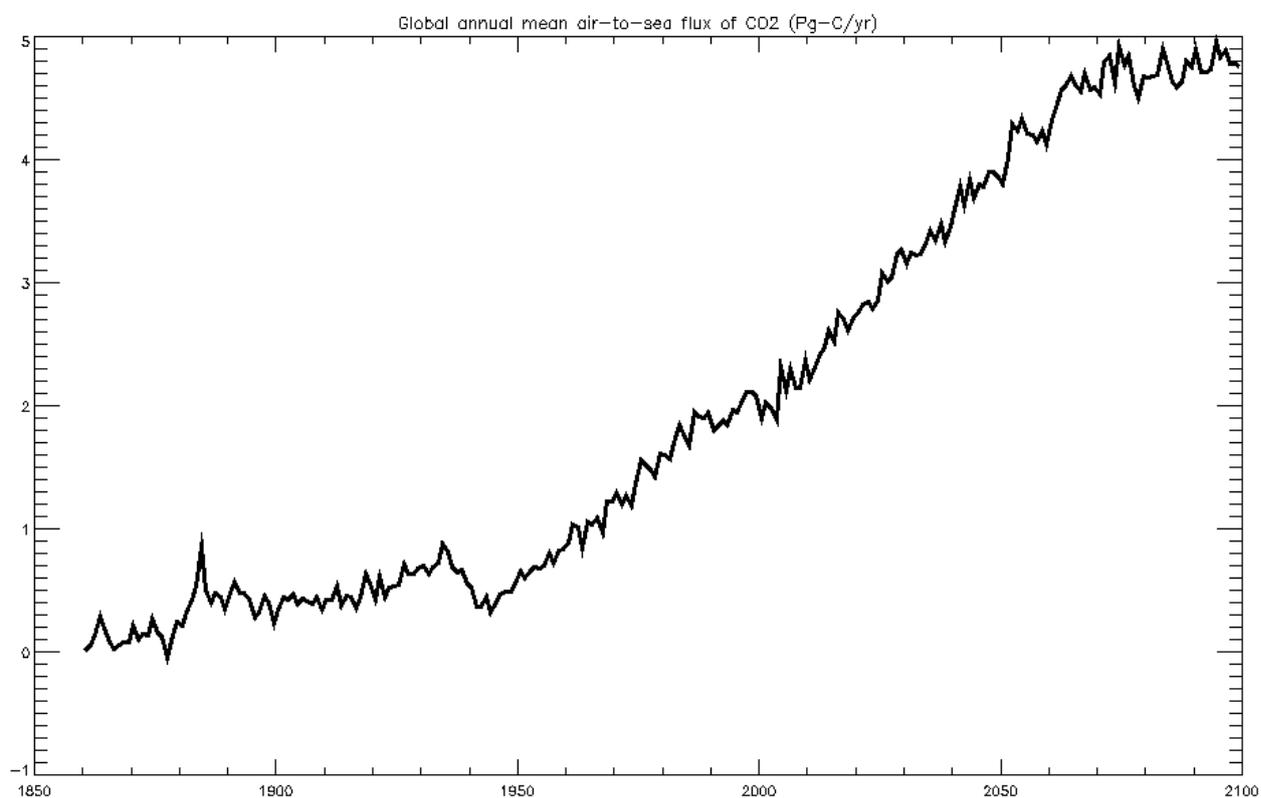
**Figure 28.** Time-evolution of the annual mean global total air-to-sea $CO_2$ flux (Pg C yr$^{-1}$) between model years 1860 and 2099 in the CMIP5 Historical and RCP8.5 simulations

Geoscientific
Model Development
Discussions
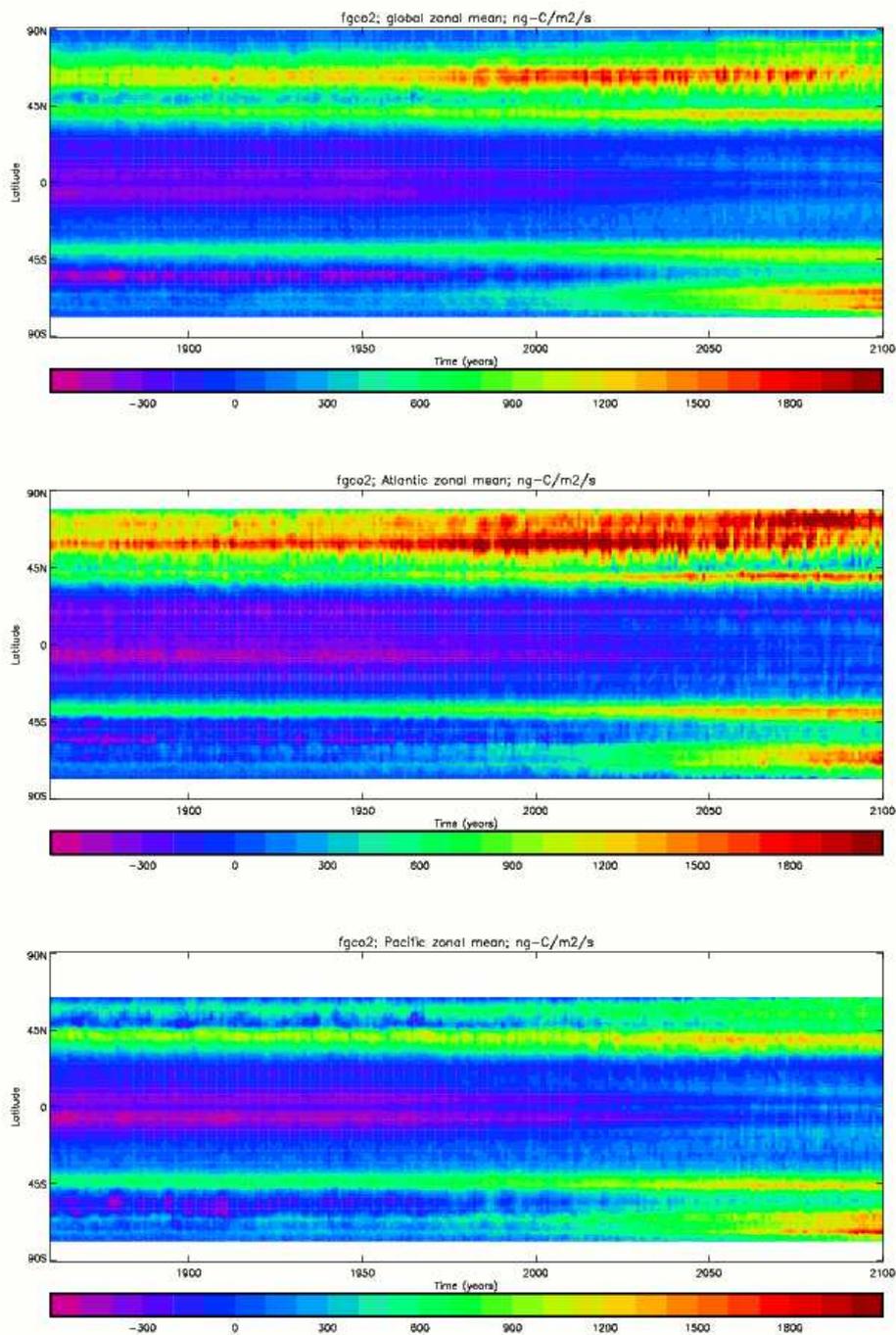


**Figure 29.** Change in the annual mean total air-to-sea $CO_2$ flux (ng C m$^{-2}$ s$^{-1}$) during model years 1860 to 2099 in the Historical and RCP8.5 simulations. Top panel: global zonal mean; middle panel: Atlantic Ocean basin zonal mean; bottom panel: Pacific Ocean basin zonal mean
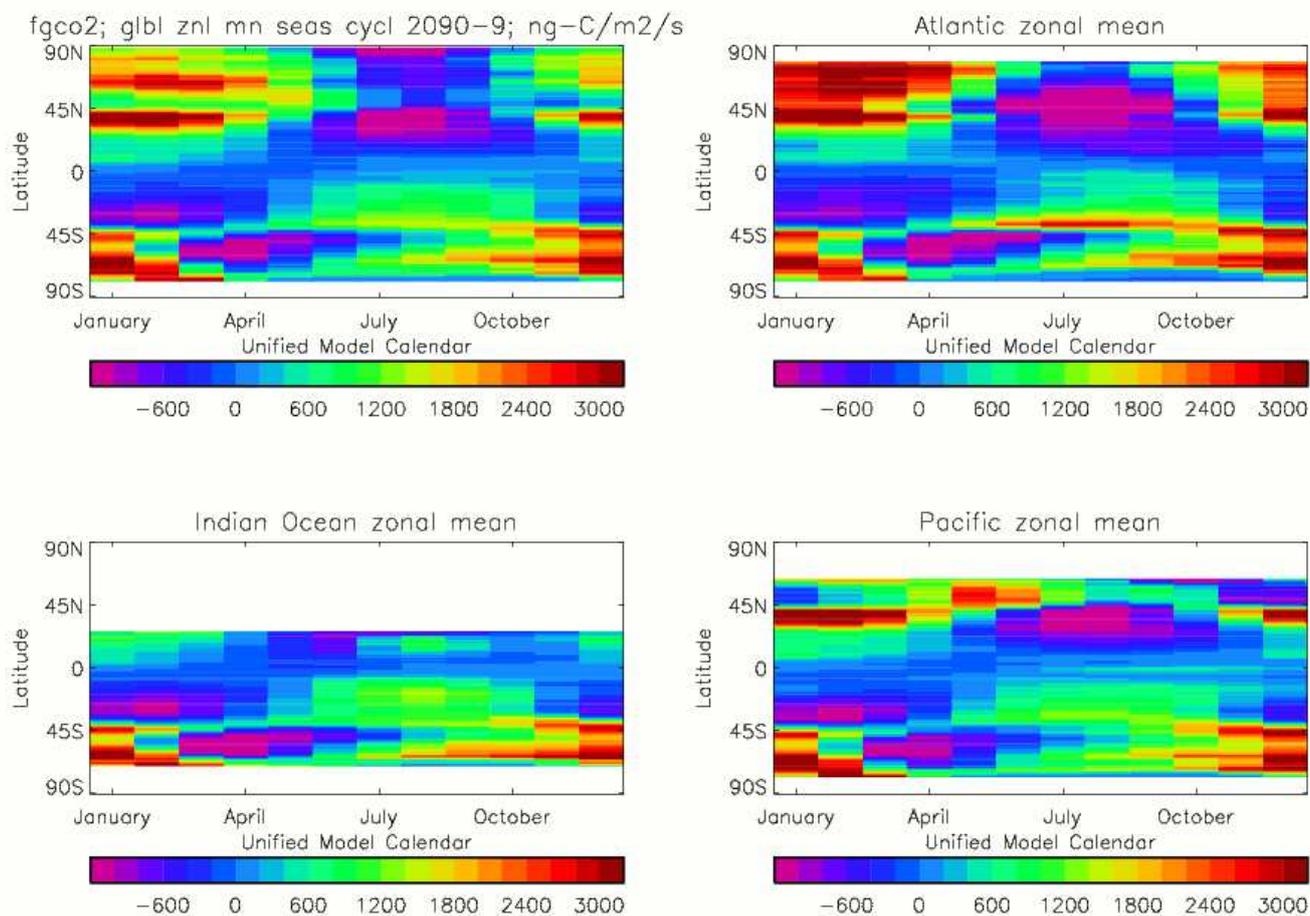
**Figure 30.** The seasonal cycle (monthly means) of the total air-to-sea $CO_2$ flux (ng C m$^{-2}$ s$^{-1}$) averaged over the model years 2090-2099 inclusive. Zonal mean of: upper left panel, global ocean; upper right, Atlantic Ocean basin; lower left, Indian Ocean basin; lower right, Pacific Ocean basin

**Table 1.** Diat-HadOCC model state variables

| Symbol | Description | Units |
| --- | --- | --- |
| $DIN$ | dissolved inorganic nitrogen | mmol-N / m$^3$ |
| $Si$ | silicic acid | mmol-Si / m$^3$ |
| $FeT$ | total dissolved iron | umol-Fe / m$^3$ |
| $Ph$ | miscellaneous (misc-) phytoplankton | mmol-N / m$^3$ |
| $Dm$ | diatom phytoplankton | mmol-N / m$^3$ |
| $DmSi$ | diatom silicate | mmol-Si / m$^3$ |
| $Zp$ | zooplankton | mmol-N / m$^3$ |
| $DtN$ | detrital nitrogen | mmol-N / m$^3$ |
| $DtSi$ | detrital silicate | mmol-Si / m$^3$ |
| $DtC$ | detrital carbon | mmol-C / m$^3$ |
| $DIC$ | dissolved inorganic carbon | mmol-C / m$^3$ |
| $TAlk$ | total alkalinity | meq / m$^3$ |
| $Oxy$ | dissolved oxygen | mmol-O2 / m$^3$ |

**Table 2.** Polynomial coeffs relating $k$ to square root of pigment in depth-range $L$

| $L$ | $b_{0,L}$ | $b_{1,L}$ | $b_{2,L}$ | $b_{3,L}$ | $b_{4,L}$ | $b_{5,L}$ |
|---|---|---|---|---|---|---|
| 1 | 0.095934 | 0.039307 | 0.051891 | -0.020760 | 0.0043139 | -0.00035055 |
| 2 | 0.026590 | 0.016301 | 0.073944 | -0.038958 | 0.0075507 | -0.00054532 |
| 3 | 0.015464 | 0.14886 | -0.15711 | 0.15065 | -0.055830 | 0.0075811 |

**Table 3.** Polynomial coeffs for $\frac{da\#}{dz}$ as a function of pigment and depth

| | |
|---|---|
| $gcof_1 = g_1 = 0.048014$ | $gcof_6 = g_4 = 0.0031095$ |
| $gcof_2 = g_2 = 0.00023779$ | $gcof_7 = g_9 = 0.0012398$ |
| $gcof_3 = g_5 = -0.0090545$ | $gcof_8 = g_6 = 0.0027974$ |
| $gcof_4 = g_7 = 0.00085217$ | $gcof_9 = g_{10} = -0.00061991$ |
| $gcof_5 = g_3 = -0.023074$ | $gcof_{10} = g_8 = -0.0000039804$ |

Geoscientific
Model Development
Discussions
Open Access

**Table 4.** Polynomial coeffs and rational function coeffs for psynth calculation

| Coeff | i=1 | 2 | 3 | 4 | 5 |
|-------|-----|---|---|---|---|
| $\Omega_i$ | 1.9004 | -0.28333 | 0.028050 | -0.0014729 | 0.000030841 |
| $\gamma_i$ | 1.62461 | 0.0045412 | 0.13140 | | |

**Table 5.** Parameter values used in CMIP5 simulations

| Param | Value | Units | Description |
|---|---|---|---|
| $P_{m,r}^{Ph}$ | 1.5 | d$^{-1}$ | Max rate of psynth; misc-Phyto, Fe-replete |
| $P_{m,l}^{Ph}$ | 1.5 | d$^{-1}$ | Max rate of psynth; misc-Phyto, Fe-limited |
| $P_{m,r}^{Dm}$ | 1.85 | d$^{-1}$ | Max rate of photosynthesis; diatom, Fe-replete |
| $P_{m,l}^{Dm}$ | 1.11 | d$^{-1}$ | Max rate of photosynthesis; diatom, Fe-limited |
| $\alpha^{Ph}$ | 0.02 | mg C (mg Chl)$^{-1}$ h$^{-1}$ ($\mu$Einst m$^{-2}$ s$^{-1}$)$^{-1}$ | Initial slope of the psynth-light curve; misc-Phyto |
| $\alpha^{Dm}$ | 0.02 | mg C (mg Chl)$^{-1}$ h$^{-1}$ ($\mu$Einst m$^{-2}$ s$^{-1}$)$^{-1}$ | Initial slope of the psynth-light curve; diatom |
| $k_{DIN}^{Ph}$ | 0.1 | mMol N m$^{-3}$ | Half-saturation const, N uptake; misc-Phyto |
| $k_{DIN}^{Dm}$ | 0.2 | mMol N m$^{-3}$ | Half-saturation const, N uptake; diatom |
| $k_{Si}^{Dm}$ | 1.0 | mMol Si m$^{-3}$ | Half-saturation const, Si uptake; diatom |
| $R_{c2n}^{Ph}$ | 6.625 | mMol C (mMol N)$^{-1}$ | Molar C:N ratio, misc-Phyto |
| $R_{c2n}^{Dm}$ | 6.625 | mMol C (mMol N)$^{-1}$ | Molar C:N ratio, diatom |
| $R_{c2n}^{Zp}$ | 5.625 | mMol C (mMol N)$^{-1}$ | Molar C:N ratio, zoopl |
| $R_{si2n,r}^{Dm}$ | 0.606 | mMol Si (mMol N)$^{-1}$ | Molar Si:N ratio, diatom, Fe-replete |
| $R_{si2n,l}^{Dm}$ | 0.606 | mMol Si (mMol N)$^{-1}$ | Molar Si:N ratio, diatom, Fe-limited |
| $R_{c2chl,0}^{Ph}$ | 40.0 | mg C (mg Chl)$^{-1}$ | default Carbon:Chlorophyll ratio, misc-Phyto |
| $R_{c2chl,min}^{Ph}$ | 20.0 | mg C (mg Chl)$^{-1}$ | minimum Carbon:Chlorophyll ratio, misc-Phyto |
| $R_{c2chl,max}^{Ph}$ | 200.0 | mg C (mg Chl)$^{-1}$ | maximum Carbon:Chlorophyll ratio, misc-Phyto |
| $R_{c2chl,0}^{Dm}$ | 40.0 | mg C (mg Chl)$^{-1}$ | default Carbon:Chlorophyll ratio, diatom |
| $R_{c2chl,min}^{Dm}$ | 20.0 | mg C (mg Chl)$^{-1}$ | minimum Carbon:Chlorophyll ratio, diatom |
| $R_{c2chl,max}^{Dm}$ | 200.0 | mg C (mg Chl)$^{-1}$ | maximum Carbon:Chlorophyll ratio, diatom |
| $g_{max}$ | 0.8 | d$^{-1}$ | Max specific rate of zooplankton grazing |
| $g_{sat}$ | 0.5 | nMol N m$^{-3}$ | Half-saturation const for zoopl grazing |
| $bprf_{Ph}$ | 0.45 | (none) | Zoopl base feeding preference for misc-Phyto |
| $bprf_{Dm,r}$ | 0.45 | (none) | Zoopl base feeding pref: diatom, Fe-replete |
| $bprf_{Dm,l}$ | 0.45 | (none) | Zoopl base feeding pref: diatom, Fe-limited |
| $bprf_{Dt}$ | 0.10 | (none) | Zoopl base feeding preference for detritus |
| $F_{ingst}$ | 0.77 | (none) | Fraction of food that is ingested |
| $F_{messy}$ | 0.1 | (none) | Frac of non-ingstd food to dslvd nutrient/carbon |
| $\beta^{Ph}$ | 0.9 | (none) | Assimilate-able frac of ingested misc-Phyto |
| $\beta^{Dm}$ | 0.9 | (none) | Frac of ingested diatom that can be assimilated |
| $\beta^{Dt}$ | 0.7 | (none) | Frac of ingested detritus that can be assimilated |

Geoscientific
Model Development
Discussions

**Table 5a.** Parameter values used in CMIP5 simulations (cont)

| Param | Value | Units | Description |
|---|---|---|---|
| $\Pi^{Ph}_{resp}$ | 0.05 | $d^{-1}$ | misc-Phyto respiration, specific rate |
| $\Pi^{Dm}_{resp}$ | 0.0 | $d^{-1}$ | Diatom respiration, specific rate |
| $\Pi^{Ph}_{mort}$ | 0.05 | $d^{-1}$ (mMol N m$^{-3}$)$^{-1}$ | misc-Phyto mortality, density-dep rate |
| $ph_{min}$ | 0.01 | mMol N m$^{-3}$ | misc-Phyto conc below which mortality is zero |
| $\Pi^{Dm}_{mort}$ | 0.04 | $d^{-1}$ (mMol N m$^{-3}$)$^{-1}$ | Diatom mortality, density-dep rate |
| $\Pi^{Zp}_{lin}$ | 0.05 | $d^{-1}$ | Zooplankton losses, specific rate |
| $\Pi^{Zp}_{mort}$ | 0.3 | $d^{-1}$ (mMol N m$^{-3}$)$^{-1}$ | Zoopl. mortality, density-dep |
| $F_{nmp}$ | 0.01 | (none) | Fraction of mortality to dissolved nutrient |
| $F_{zmort}$ | 0.67 | (none) | Fraction of zoopl mortality to dissolved nutrient |
| $V_{Dt}$ | 10.0 | m d$^{-1}$ | Sinking speed, detritus |
| $\Pi^{DtC}_{rmndd}$ | 8.58 | m d$^{-1}$ | Detrital remineralisation rate factor, carbon |
| $\Pi^{DtC}_{rmnmx}$ | 0.125 | $d^{-1}$ | Max detrital remineralisation rate, carbon |
| $\Pi^{DtN}_{rmndd}$ | 8.58 | m d$^{-1}$ | Detrital remineralisation rate factor, nitrogen |
| $\Pi^{DtN}_{rmnmx}$ | 0.125 | $d^{-1}$ | Max detrital remineralisation rate, nitrogen |
| $\Pi^{DtSi}_{rmn}$ | 0.05 | $d^{-1}$ | Detrital silicate (opal) remin/dissolution rate |
| $V_{Dm}$ | 1.0 | m d$^{-1}$ | Diatom sinking speed |
| $R^{eco}_{fe2c}$ | 0.025 | $\mu$Mol Fe (mMol C)$^{-1}$ | Molar Fe:C ratio for ecosystem |
| $k_{FeT}$ | 0.2 | $\mu$Mol Fe m$^{-3}$ | Half-saturation factor for Fe-limitation |
| $LgT$ | 1.0 | $\mu$Mol m$^{-3}$ | Total ligand concentration |
| $K_{FeL}$ | 200.0 | ($\mu$Mol m$^{-3}$)$^{-1}$ | Fe-ligand partition function |
| $\Pi^{FeF}_{ads}$ | $5.0\times10^{-5}$ | $d^{-1}$ | Adsorption rate of iron onto particles |
| $R^{eco}_{o2c}$ | 1.302 | mMol O$_2$ (mMol C)$^{-1}$ | Molar O$_2$:C ratio for ecosystem |
| $R^{Ph}_{cc2pp}$ | 0.0195 | mMol CaCO$_3$ (mMol C)$^{-1}$ | Misc-Phyto molar ratio, carbnt frmtn:organic prodn |
| $Z_{lys}$ | 2113.0 | m | Depth of lysocline |